



ARCS: Auroral Reconstruction CubeSwarm

A 2019 Heliophysics Medium-Class Explorer Phase A Concept Study

Section E: Science Implementation

Robert E Erlandson, JHU/APL

Kristina A Lynch, Dartmouth College

Marilia Samara, NASA/GSFC

Brian Anderson, APL

Jacob Bortnik, UCLA

Meghan Burleigh, UMich, now NRL

David Knudsen, Calgary

Kshitija Deshpande, ERAU

Don Hampton, UAF/GI

Lynn Kistler, UNH

Jim LaBelle, Dartmouth

John Lyon, Dartmouth

Elizabeth MacDonald, GSFC

Robert Michell, GSFC

Chris Mouikis, UNH

Steven Myers, SwRI, now FrontGrade Technologies

Rumi Nakamura, IWF

Romina Nikoukar, APL

Werner Magnes, IWF

David Rau, UNH

Griffith Russell, Gryphon Effect

Christine Schulz, SwRI

Roy Torbert, UNH

Jules van Irsel, Dartmouth

Sarah Vines, APL, now SwRI

Matt Zettergren, ERAU

Shasha Zou, UMich

Submitted to NASA July 2019

Published as a NASA Technical Report, 2024

Accompanying report, Section D: Science, Lynch, Erlandson, et al.



AURORAL RECONSTRUCTION CUBESWARM

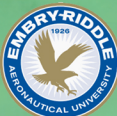
2019 Heliophysics Medium-Class Explorer
Phase A Concept Study
07 July 2021

Principal Investigator:
Professor Kristina A. Lynch, Dartmouth College

A handwritten signature in black ink, appearing to read "Kristina A. Lynch".

Authorizing Official:
Jill Mortali, Dir., Office of Sponsored Projects
Dartmouth College

A handwritten signature in black ink, appearing to read "Jill Mortali".





Proposal title page restriction removed for this public document.

Cover Page Credit: Photo, J. Ahrns/UAF

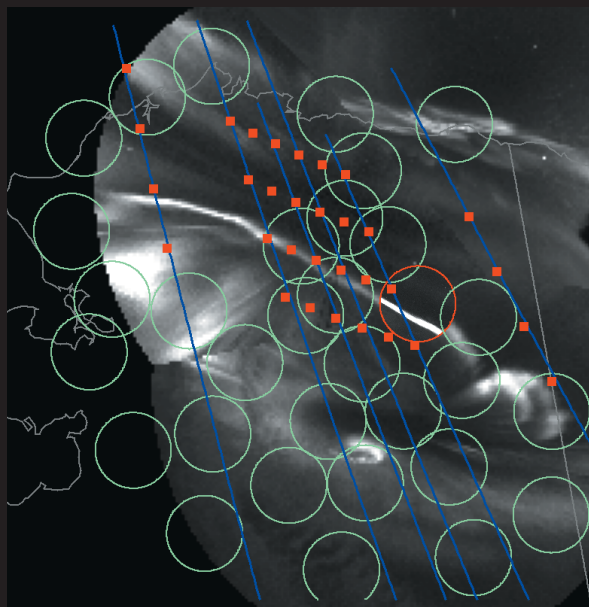


AURORAL RECONSTRUCTION CUBE SWARM

Connecting the Dots: A distributed high-fidelity map for decoding the auroral ionosphere

The **ARCS MISSION GOAL:** decode the aurora by exploring the relationship between the visible aurora and distributed currents and flow fields, to unlock critical physics of the auroral ionosphere at mesoscales.

ARCS addresses Key NASA Goals by exploring auroral processes at mesoscales. These scales have consequences, not only for the ionosphere-thermosphere (IT) system but significantly for the global dynamics of the entire magnetosphere. ARCS directly aligns with NASA Strategic Goals and Objectives and with NASA SMD's strategic objectives to explore processes in the space environment active throughout the solar system and the universe. Specifically, ARCS's focus is to fill key knowledge gaps of "how the IT system responds to, and regulates magnetospheric forcing over... regional and local scales" (AIMI-1).



ARCS Science Objectives:

- SO-1: DISCOVER** Map the 2D mesoscale structure and temporal evolution of plasma flows and currents in the auroral ionosphere.
- SO-2: LINK** Determine how these 2D maps of plasma flows and currents self-consistently evolve in conjunction with auroral ionospheric density responses
- SO-3: UNDERSTAND** Determine the roles of the physical mechanisms regulating the relationships between the flows, currents, auroral forms and precipitation in the auroral ionospheric system.

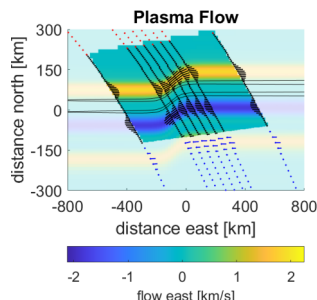
ARCS MISSION OVERVIEW:

- Truly next generation mission using a swarm of 32 cubesats (red dots above) to explore the aurora at mesoscales
- In-situ flows, currents, and 3D electron density measurements over a dedicated array of ground-based auroral imagers (green circles above) & dual frequency transmitters
- Multi-point data reconstructions feed modern 3D physics-based simulations to explore the auroral ionosphere as a system
- Observing System Simulation Experiment (OSSE) with synthetic data generated by GEMINI model shown in reconstruction examples below

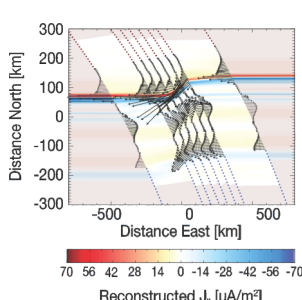


ARCS SYNTHETIC DATA RECONSTRUCTIONS

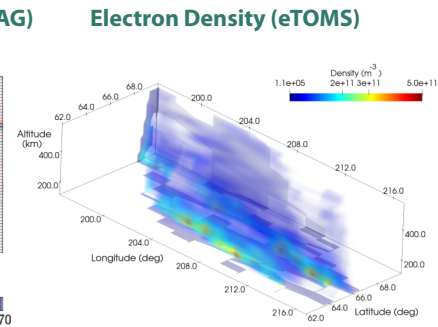
Plasma Flow (STA)



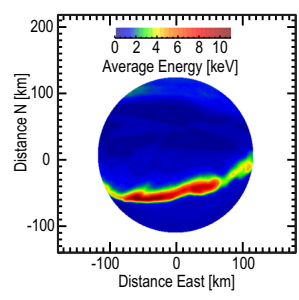
Field Aligned Currents (MAG)



Electron Density (eTOMS)



Precipitation Energy (GBO)



The ARCS swarm produces low-resource observations for system science enabling progress toward the **"Diversified and Distributed Sensor Deployment Strategy"** envisioned in the NAS Decadal Appendix C [NRC, 2013] as a requirement for creating "system-wide understanding" based on data "integrated into distributed yet coordinated approaches that create the best system-wide understanding."

E. Science Implementation

E.1 Level 1 Science Requirements and Level 2 Project Requirements

The ARCS team have developed draft mission success criteria and Level 1 (L1) and Level 2 (L2) science requirements. These requirements flow from the Science Traceability Matrix (STM). The L1 science requirements are shown in Table E-1 along with their flow-down from the ARCS Science Objectives (SO1, -2 and -3). Each Science Objective builds upon the previous objective. For example, SO1 requires plasma flow maps and field-aligned current maps (L1-SR-1, -2); SO2 builds upon SO1 by requiring electron density 3d maps (L1-SR-3); SO3 builds on SO2 requiring auroral image mosaics, electron average energy and energy flux maps (L1-SR-4, -5). All involve the ARCS modeling related L1 requirement (L1-SR-6).

The flow-down to L2 measurement and instrument requirements are also shown in Table E-1. These requirements are met by establishing a 32-satellite formation that we call the “CubeSwarm” and a network of 32 Ground Based Observatories (GBO) (FO1-C, F). The ARCS in-situ instruments (FO1-F) include the STA (plasma flow maps), MAG (field aligned current maps) and eTOMS (electron density maps). These instruments are used to address L1-SR-1, -2 and -3. The GBOs house the multispectral auroral cameras that address L1-SR-4 and -5, and the dual frequency ground transmitters whose signals are received by eTOMS.

Key ARCS L2 mission requirements are provided in App L.22. The L2 requirements include mission, mission design, spacecraft (S/C) design, ground system, launch system, space segment instrument measurement and ground segment instrument measurement requirements.

L1 Science Requirements – Threshold Mission. The Baseline and Threshold mission were defined in §D.3. The Baseline mission launches 32 satellites, requiring at least 24 satellites to simultaneously collect science data. The Threshold science mission launches 24 satellites, requiring that at least 16 satellites to simultaneously collect science data. There are no changes in the instrumentation between the Baseline and

ARCS leverages exciting new advances in small satellites, coupled with high heritage instruments, to explore the auroral ionosphere at mesoscales.

- ARCS 32-satellite CubeSwarm with high-heritage identical instruments providing multi-point observations of the auroral ionosphere.
- Ground Based Observatory (GBO) at 32 sites in Alaska provide mesoscale imaging of the aurora.
- Novel approach using dual-frequency ground transmitters and eTOMS RF receivers enables 3D tomographic reconstruction of the e- density
- Identical satellite configuration, high-heritage instruments, low complexity science operations (on/off) enables low risk CubeSwarm approach

Threshold missions. The result of fewer satellites in the CubeSwarm results in lower time resolution of the Level-1 requirements (STA and MAG) and a larger uncertainty for eTOMS. See Table E-1, representing the L1 Science Requirements for the Threshold mission. The Threshold mission will include the same 8 planes of satellites as the Baseline mission. The difference is that there will be at least 2 operating satellites per plane versus at least 3 operating satellites per plane in the Baseline mission. There are no changes to the GBO between the Baseline and the Threshold mission.

The reduction in satellites from the Baseline to Threshold mission results in less frequent map updates due to a larger gap between the leading and trailing satellites. For eTOMS (L1-SR-3), the reduction in satellites results in an increase in error of the electron density from $1 \times 10^{11} \text{ e-}/\text{m}^3$ to $2 \times 10^{11} \text{ e-}/\text{m}^3$, an increase due to the decrease in the number of ray paths used in the inversion (§E.3.3 for a discussion of error).

E.1.2 Mission Success Criteria

The draft mission success criteria are based on the Threshold science requirements. The Mission Success Criteria, shown below, result in closure of all ARCS SOs (Table D-1 and §D.2.3).

Table E-1: Flowdown from STM Science Objectives to L1 and L2 Requirements.

Science Objectives	Level 1 Science Requirements for Baseline Mission (Threshold Mission)	Level 2 Measurement Requirements	L2 Instrument Requirements
SO1 Map the 2D mesoscale structure and temporal evolution of plasma flows and currents in the auroral ionosphere	L1.SR-1 Plasma Flow Maps: ARCS shall produce maps of the plasma flow at a rate of at least one map every 18s (36s) with an uncertainty lower than 300 m/s, a latitude resolution of at least 2 km, and an average longitude resolution of 150 km in the pre-magnetic midnight sector auroral zone, as a moving mosaic along the S/C orbit to resolve along-track gradients with a scale size of at least 500m.	L2-MSR-1 ARCS shall measure the plasma flow with an uncertainty lower than 300 m/s every 50 ms. (at each of the 32 satellite locations)	L2-I1 The STA instrument shall measure the ion distribution function at energies from 1-20 eV (better than 12% energy resolution) and over a 100 x 100° field of view centered on the ram direction.
	L1.SR-2 Field Aligned Current Maps: ARCS shall produce maps of the field aligned current density at a rate of at least one map every 18s (36s) with a resolution of at least 1 μA/m ² , a latitude resolution of at least 2 km, and an average longitude resolution of 150 km in the pre-magnetic midnight sector auroral zone, as a moving mosaic along the S/C orbit to resolve along-track gradients with a scale size of at least 500m.	L2.MSR-2 ARCS shall measure the magnetic field with an accuracy of at least 30 nT every 50 ms. (at each off the 32 satellite locations)	L2-I2 The three-axis fluxgate magnetometer (MAG) instrument shall measure the vector magnetic field with a resolutoin of at least 2 nT over the range from -50000 to +50000 nT.
SO2 Determine how these 2D maps of plasma flows and currents self-consistently evolve in conjunction with auroral ionospheric density responses	L1.SR-1, L1.SR-2 and		
	L1.SR-3 Electron Density Maps: ARCS shall produce volumetric (3D) maps of electron densities every 60s from 90-540 km with a spatial resolution between 10-40 km in altitude, 1° in latitude and 2° in longitude in the pre-magnetic midnight sector auroral zone over the GBO array, as a moving mosaic along the S/C overpass. The E-region density uncertainty, associated with auroral precipitation, shall be less than $1 \times 10^{11} \text{ e-} / \text{m}^3$ ($2 \times 10^{11} \text{ e-} / \text{m}^3$).	L2-MSR-3: Electron Density: ARCS shall measure relative TEC to an accuracy of 0.02 TECU or better at a rate of at least 1 Hz	L2-I3: Electron Density: The eTOMS instrument shall simultaneously measure the amplitude and phase of UHF (400-500 MHz) and S-Band (2025-2120 MHz) signals up to 9 different ARCS GBO ground transmitters at a rate of at least 50 Hz.
SO3 Determine the roles of the physical mechanisms regulating the relationships between the flows, currents, precipitation and auroral forms in the auroral ionospheric system	L1.SR-1, L1.SR-2, L1.SR-3 and		
	L1.SR-4 Auroral Image Mosaics: ARCS shall acquire auroral imagery during S/C overpasses at wavelengths of 427.8 nm, 557.7 nm, 630.0 nm and 844.6 nm at an image cadence of at least 8 Hz for 427.8 nm, 557.7 nm and 844.6 nm, and at least 0.5 Hz for 630 nm in the pre-magnetic midnight sector auroral zone, with at least 75% coverage from 62-72° magnetic latitude across Alaskan longitudes.	L2-MSR-5 Auroral Image Mosaics, Average Energy and Energy Flux Maps: The ARCS Project shall acquire auroral imagery in 3 bands (427.8, 557.7 and 844.6 nm) at 8 Hz and one band (630.0 nm) at 0.5 Hz across the 32 GBO sites distributed across Alaska covering 62 to 72° magnetic latitude (75% coverage).	L2-I5 Auroral Image Mosaics: The GBO auroral imagers shall acquire auroral imagery in 3 bands (427.8, 557.7 and 844.6 nm) with a sensitivity of 250 Rayleigh and one band (630.0 nm) with a sensitivity of 50 Rayleigh.
SO1 to SO3	L1.SR-6 Data Assimilation, Modelling and Data Reconstruction: ARCS shall ingest Level 1 science products (L1-SR-1 to -5) into the ARCS modeling framework (FrAMBOISE) and produce model outputs, producing a system view of the auroral ionosphere using the physics based models to address the ARCS science objectives.	L2-MSR-1 to -5	L2-I1 to I5

Draft Mission Success Criteria. ARCS is the first CubeSwarm multi-point investigation of the aurora at multi-scales, launching 24 or more satellites, resulting in at least 16 satellites that acquire simultaneous multi-point observations to decode the relationship between the visible aurora and distributed currents and flow fields, to unlock critical physics of the auroral ionosphere at mesoscales, those scales associated with discrete auroral arcs. Mesoscales will be investigated by producing the products below over an area of 500 km in latitude and 900 km in longitude in the pre-magnetic midnight sector. To achieve this ARCS shall:

- Produce time-dependent moving-mosaic maps of the plasma flow at mesoscale resolutions.
- Produce time-dependent moving-mosaic maps of field aligned current density at mesoscale resolutions.
- Produce time-dependent moving-mosaic 3-dimensional electron density profiles at mesoscale resolutions.
- Acquire time-dependent multi-spectral auroral imagery.
- Produce time-dependent maps of electron average energy and energy flux.

Acquire simultaneous observations of at least 1000 science passes in the pre-magnetic midnight sector auroral zone. The distribution of science crossings shall include 30% of crossings with eTOMS data (SO2) and 15% of crossings with GBO auroral imaging data (SO3). These science crossings will provide the data necessary to provide science closure (§D.6) by addressing key science investigations associated with each SO (Table D-2).

E.2 Science Mission Profile

The ARCS science mission profile is focused on the pre-magnetic midnight sector auroral zone with simultaneous multi-point in-situ satellite observations and the Alaskan dense network of ARCS-specific GBOs. The specific ARCS SOs allows us focus on the science data collection on 3 daily 12-minute long science passes (Fig. E-1).

E.2.1 Orbit Design and GBO Site Locations

Orbit. The ARCS L1 science requirements (Table E-1: L1-SR-3, -4 and -5) flow down to

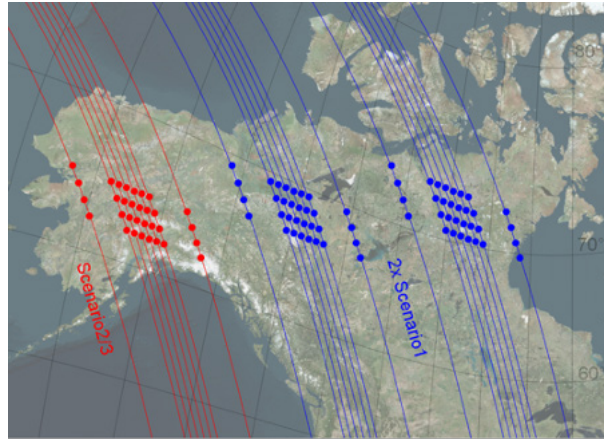


Figure E-1. ARCS 3-daily science observations.

the L2 requirement (App. L.22) to center the magnetic field line projection of CubeSwarm on the center of the multi-site GBO array in Alaska. This allows simultaneous observations of the in-situ sensors with ground based auroral imagery from the GBO array. This relationship between the CubeSwarm and the GBO array leads to the selection of a repeating ground track orbit, designed to “fly-over” nightside Alaska once per day at 1000 UT which corresponds to 2230 Magnetic Local Time (MLT) over Alaska.

The ARCS orbit is a ground track repeat orbit that centers the CubeSwarm array over Alaska and the GBO array at 1000 UT +/- 2 minutes every day. The ascending node on the dark side of the earth is chosen for thermal stability of the satellites, which will go into eclipse in the southern hemisphere rather than just before the northern hemisphere science passes. The orbit that achieves this daily ground repeat is a circular sun sync orbit (FO1-F). The orbit repeat accuracy ensures that the CubeSwarm is over the center of GBO array once per day FO1-C.

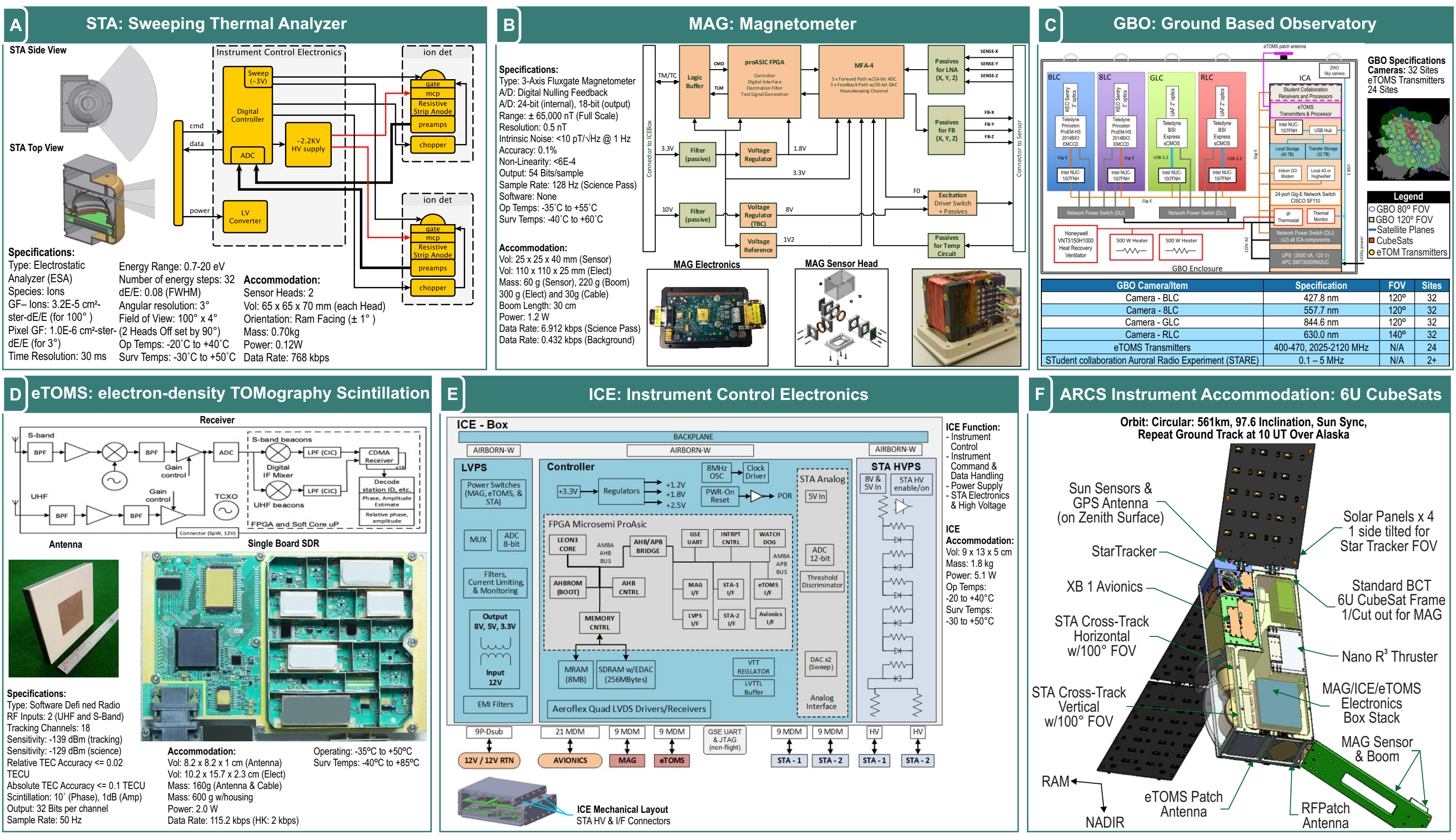
Ground Sites. An integral part of the ARCS mission is the use of GBO auroral imagers to remotely sense the visible aurora and house dual-band RF transmitters whose signals are acquired by the eTOMS instrument for the tomographic reconstruction of the ionosphere. ARCS will fabricate, deploy and operate 32 of these GBO sites at locations spread across Alaska, as shown in FO1-C and described in §E.3.4. The GBO auroral camera observations require darkness at the site. Figure E-2 shows the days of the year as a function of GBO site latitude when auroral viewing is possible.



AURORAL RECONSTRUCTION CUBESWARM

Science Implementation

F01



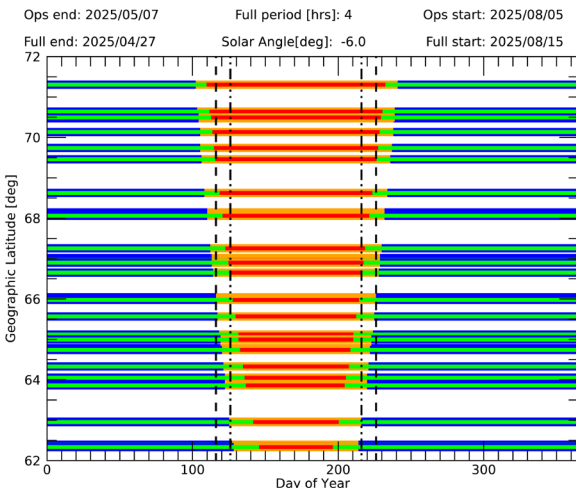


Figure E-2. Seasonal sunlight plot for Alaska at 1000 UTC (vertical markers corresponding to Bettles GBO site). Green/blue represent days where lighting is favorable for GBO operations

E.2.2 CubeSwarm Configuration and Accuracy

The driver of the ARCS CubeSwarm configuration is based on the objective to focus on mesoscale auroral features. Flow down from the ARCS SOs and the rationale for the CubeSwarm is addressed in §D. The resulting requirement (App. L.22) is for 8 planes of satellites with 4 satellites per plane (Fig. E-1). The outer two planes (1 and 8) are separated from the neighboring planes by 300 km in longitude (all distances are at values at the latitude of central Alaska). The inner planes (2 to 7) are separated by 47 km in longitude in order to resolve mesoscale auroral features. The outer planes are at a larger separation to provide context and capture auroral features that span up to 900 km in longitude (§D.2.1). Each “row” of satellites trails the leading satellite by 18s and spans 900 km in longitude over Alaska.

The navigation accuracy of the entire CubeSwarm is governed by the requirement for the satellites’ position mapped along the magnetic field line to an altitude of 110 km to pass over the most dense portion of the Alaskan GBO array at the same time every day. The resulting accuracy requirements of the CubeSwarm are presented in App. L.22.7.1 and Figure L.22.3. The engineering implementation of this control box is discussed in §F.2.6.1.

E.2.3 ARCS Operation Modes

The ARCS mission has four major operation-

al modes, excluding commissioning and safe-modes. These four modes are Science Mode (SM), Data Downlink Mode (DDM), Formation Maintenance Mode (FMM) and Background Mode (BM). Engineering implementation of these modes is discussed in §F.

E.2.3.1 Science Modes

ARCS SM occurs 3 times per day, with each science mode observation lasting for 12 minutes. All 32 satellites will participate in a science mode and have identical configurations. All satellites transition to SM at the same time. The STA and MAG instruments are turned on during all Science Passes. The eTOMS instrument is turned on during all passes over Alaska. The GBOs operate during all passes over Alaska when there is favorable lighting regardless of cloud cover (Fig E-2). The exact dates of favorable lighting conditions is a function of latitude (Fig. E-2).

The ARCS instrument settings in SM are very straightforward (§E.3.1.3, §E.3.2.3, §E.3.3.3 and §E.3.4.3). In SM, MAG will be commanded to a high sampling rate (128 Hz) mode and will remain in a low-data-rate (8 Hz) collection mode in all other modes (BM, DDM, FMM). The MAG requires magnetic cleanliness and therefore the torquer rods are turned off during SM and are off 1s of every 10 in BM. (§F.2.2).

The duration of each science pass is 12 mins (1/8 of an orbit), starting at 45°N and ending at 82.4°N (the highest latitude of our 97.6° inclination orbit.). The SM is the only mode where science-based attitude requirements are placed on the satellite. In SM, science requires the S/C attitude control system to align the STA in ram to $\pm 1^\circ$ and eTOMS in nadir to $\pm 3^\circ$.

E.2.3.2 Data Downlink Mode

ARCS science data are transmitted to the ground in DDM. The objective of DDM is to send science data from 3 science passes to the ground every day. The telemetry system, ground receivers, link margins and downlink plans are described in §F.2.6.1.

E.2.3.3 CubeSwarm Formation Maintenance Mode

ARCS FMM is the mode used to maintain the position of each satellite in its required control box. The ion propulsion system will be off dur-

ing SM. FMM will also be used for conjunction mitigation maneuvers (§F.2.2).

E.2.3.4 Background Mode

ARCS BM is the mode outside of the SM, DDM and FMM windows. Science data is not collected in this mode, except for the magnetometer, which collects data continuously throughout the mission needed to support background magnetic field removal from the data collected during Science Mode. The torquer rods operate during BM to maintain attitude. However, they are turned off one out of every 10 s to provide clean data at 10 s intervals throughout the orbit.

E.2.3.5 Science Mission Timelines

The ARCS science data collection occurs during 12-minute-long science passes three times per day that provide coverage of the pre-midnight sector auroral ionosphere from approximately 45–90°N latitude. The GBO eTOMS transmitters are operated once per day, year-round and the GBO auroral cameras operate once per day from mid-September to mid-April, when there is darkness at the GBO sites (Fig. E-2).

GBO eTOMS transmitter science operations are identical at each of the 24 GBO stations that have eTOMS transmitters. The eTOMS transmitters are turned on 15 minutes before the ARCS science pass and turned off 5 minutes after the pass ends.

GBO auroral camera science operations are identical at each of the 32 GBO stations. Cameras operate from dusk to dawn in a survey mode (1 frame/s) and operate in Burst mode (15 frames/s) for 15 mins centered on the ARCS science pass, then return to Survey mode at the end of the 15 mins.

The ARCS science instrument operations are required to be simultaneous and identical across the 32 satellites greatly simplifying the ground processing and cross comparison of data. The full sequence of science instrument events and GBO events are shown for each of the 3 Observing Scenarios (Table E-2). In general, the instruments are turned on prior to the science crossing to warm up and in some cases to enter into a high-data-rate mode (MAG and GBO ground based cameras). MAG data are saved at high rate in SM and averaged by the ICE to 8 samples/s in all other modes.

System-State	Science Pass		
	Scen1	Scen2	Scen3
	Not Alaska	Over Alaska	Over Alaska
All Seasons		Apr to Sept*	Sept to April*
GBO Survey Mode	N/A	N/A	Dusk Local
GBO Burst Mode	N/A	N/A	0945 UT
eTOMS Tx On	N/A	0945 UT	0945 UT
eTOMS Rx On Warm up	N/A	0945 UT	0945 UT
STA Power & HV On	T-10 Min	0950 UT	0950 UT
Torquers Disabled	T-8 Min	0952 UT	0952 UT
Science Pass begins	T-6 Min	0954 UT	0954 UT
Center of Science Pass	T-0 Min	1000 UT	1000 UT
Science Pass ends	T+6 Min	1006 UT	1006 UT
Torquers Enabled	T+8 Min	1008 UT	1008 UT
STA HV & Power Off	T+9 Min	1009 UT	1009 UT
eTOMS RX Off	N/A	1010 UT	1010 UT
GBO Survey Mode	N/A	N/A	1011 UT
eTOMS Tx Off	N/A	1016 UT	1016 UT
GBO Off	N/A	N/A	Dawn Local

* See Figure E-2 for dates and lighting conditions at GBO Sites

E.2.4 Science Operations Planning

The ARCS science planning is very straightforward. One science pass occurs over Alaska at the same time every day (Scen2 or -3 observations). The other two science passes occur outside of the Alaskan sector. The primary science operations planning task is to determine the time of the two non-Alaskan science passes (defined as Scen1, (§D.2.2)). The Baseline is that these two Scen1 observations will occur over western and eastern Canada (Fig E-1). However, other longitudes, such as in Scandinavia, will be considered (§D.2.2).

The ARCS CubeSwarm STA and MAG instruments only have one mode. The eTOMS is able to upload commands that specify which ground transmitters a given satellite receiver will acquire. eTOMS simultaneously acquires 9 dual frequency transmitters (§E.3.3). The GBO eTOMS transmitter sites are selected via upload commands and modified as needed to optimize science return.(§E.3.3.6).

The Science Operations Center (SOC) conducts science operations planning and performs initial science data ingest and processing (§F.2.7.9). This science planning function is

relatively simple compared to a typical mission, since the operations are identical for every SM pass. The data processing however is somewhat more involved to support inter-calibration and higher level product generation. Hence the SOC functions relating to sensor calibration and data processing will be more complex than in single satellite missions. Detailed SOC data plans are discussed in §E.5. and the draft data management plan is provided in App. L.5.

E.3 Instrumentation

E.3.1 Sweeping Thermal Analyzer (STA)

Because the plasma flow perpendicular to the magnetic field is given by $\mathbf{E} \times \mathbf{B}/B^2$ convection in the upper F-region, the flow measurement combined with the magnetic field is used to determine the convection electric field [Knudsen et al., 2017; Lomidze et al., 2019]. The STA (FO1-A) measures the flow velocity of the thermal plasma to map the two-dimensional mesoscale structure and temporal evolution of plasma flows in the auroral ionosphere contributing to all three SOs and L1 requirement L1.SR-1.

E.3.1.1 STA Requirements

STA performance requirements flow down from L2 requirements SR-4. The STA measures the flow velocity of the thermal plasma for velocities up to 3 km/s in 3D with resolution better than 300 m/s. At 561 km altitude, the ram velocity of the S/C is ~8 km/s, which is larger than the plasma flow. Thus the flow in the S/C frame is dominated by the ram velocity, so a FOV in the ram direction is required to measure the full distribution. To accommodate the expected velocities of the plasma, the field of view must extend 50° from the ram direction in both the horizontal cross-track and vertical directions. The ionospheric ions at this altitude are predominantly O+, so the main peaks used to determine the velocity are from O+. The instrument must be able to determine the velocity for densities from $\sim 10^9$ to 10^{11} /m³, ion temperatures from 0.1 to 0.4 eV. At a velocity of 8 km/s, this corresponds to an energy flux range of 1×10^9 to 5×10^{12} ev/cm²-s-sr-ev. To determine the velocities under these conditions requires measuring the ion distributions from 1-20 eV with better than 12% energy resolution. To determine the cross-track velocity, the peak direction must be determined to <0.5°. This requires

angular binning of < 5°. The peak is determined from fitting the angular distribution to a gaussian. The full-width at half-max of the angular distribution ranges from 13° at T=0.1 eV to 25° at T=0.4 eV. To fit the gaussian requires at least three data points spanning the distribution and sufficient counts in those data points to reduce the statistical error. Our analysis finds that 5°bins meet these constraints even in low density and temperature cases. To measure spatial structuring across auroral arc boundaries, the measurements along each S/C trajectory must be made at ~30 samples per second, corresponding to a spatial resolution of ~0.3 km. The requirements and performance characteristics are summarized in Table E-3. The performance characteristics are demonstrated in §E.3.1.2.5.

E.3.1.2 STA Instrument Design

STA Sensor. The STA on each S/C consists of two top-cap electrostatic analyzer (ESA) sensors packaged with their front-end electronics. The sensors are mounted with their entrance apertures rotated by 90°; one instrument measures the horizontal cross-track and along-track flow relative to the ram while the other measures the vertical and along-track flow. Each analyzer is a standard top-hat analyzer [Carlson et al., 1982] using a toroidal geometry [Young et al, 1988]. Figure E-3 shows sample particle trajectories through one sensor to illustrate the concept. As shown in Figure E-3a when a voltage is placed between the inner and outer hemispheres, the analyzer selects ions that fall within a narrow energy per charge and angular range. Figures E-3b and 3c show how parallel trajectories in the plane of the entrance aperture are focused at the exit of the analyzer so the position measured at the microchannel plate (MCP) detector

Table E-3: STA Performance Characteristics

Parameter	Requirement	Performance
Plasma Flow Range	+/- 2000 m/s	+/- 3000 m/s
Plasma Flow Resolution	300 m/s	13-300 m/s (Condition dependent)
Measurement Cadence	50 ms	33 ms
Energy Range	1-20 eV	0.7-20 eV
Energy Resolution	12%	10%
FOV (one sensor)	100° by <6°	100° by 4.5°
Angular binning	< 5°	3°
Flux range (ev/cm ² -s-sr-eV)	1×10^9 - 5×10^{12}	5×10^8 - 5×10^{12} (using gate)

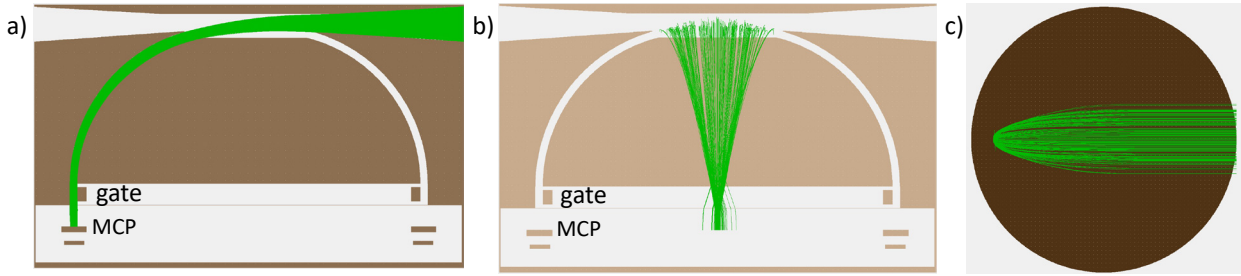


Figure E-3. Example particle trajectories in STA.

indicates the incoming direction. By stepping through a range of voltages across the analyzer, both the energy and the direction of the ions in one plane are determined. The second analyzer will measure energy and the direction in the orthogonal plane. While the basic geometry would allow a full 360° field of view, the entrance is restricted to 100° , centered on the RAM direction. The maximum expected deviation of the peak from the ram direction is 20° , but the full distribution can extend out to $\sim 50^\circ$ for higher temperatures. For cases in which there is both a strong horizontal and vertical flow, the velocity peak can fall outside the FOV. However, enough of the distribution still falls within the FOV to determine the velocity.

At the exit to the analyzer is a deflector (labeled “gate” in Fig. E-3) used to reduce the rate and increase the dynamic range of the instrument, as described below. Below the gate are a pair of MCP detectors in a chevron configuration, followed by a resistive anode, used for making position measurements.

A cross-section of the instrument from the CAD model is shown in FO1-A. The external grounded surfaces are curved, as in SWARM-TII [Knudsen et al., 2017] to minimize potential variations near the aperture. The entrance apertures are covered with grounded grids to limit stray fields as well as to optimize the geometric factor.

STA Electronics & Data Processing. A block diagram indicating each subsystem and the electrical interfaces is shown on FO1-A. The sensor electronics consist of preamps at each end of the resistive anode and a chopper circuit for the gate. When activated, the gate voltage is modulated by the chopper circuit at 500 kHz.

The preamp outputs from the two ends of the resistive anode are sent to the FPGA-based controller board located in the Instrument Control Electronics (ICE) (§E.3.1.5). The ICE also con-

tains the STA HV power supply for the MCP (0-2.2 kV) and the low voltage converter.

The Controller Board generates the analyzer voltage steps and detector biases, calculates the particle position from the pre-amp signals, and accumulates the counts in 32 positions for each energy step. It also monitors the total count rate to activate the gate. The analyzer steps through 32 energies 30 times per second, so each step is accumulated for 1.04 ms. The stepping sequence is synched to the GPS 1 Pulse Per Second (PPS) so all the instruments on all S/C step together. The total data from each sensor (two per S/C) consists of the 32×32 12-bit energy-angle arrays and a 16-bit array of total count-rate for each energy. This data is generated 30 times per second, for a total bit rate of 768 kbit/s per S/C. Data other than housekeeping is only generated in science mode.

STA Heritage and TRL. UNH has significant experience in designing and building instruments that use an ESA entrance system for energy selection followed by MCPs for detectors. Heritage derives from the ion and electron top-cap ESA instruments developed for rocket missions as well as the ion composition instruments for Cluster, STEREO, and Solar-orbiter, and the Electron Drift Instrument for Cluster and MMS. The STA sensor design is based on the HEEPS-thermal instrument. This instrument was designed at UNH for the SERSIO mission, and versions of the instrument, built at either UNH or Dartmouth, have flown on SERSIO, Scifer-2 and MICA [Fernandes et al., 2016, Fisher et al., 2016], RENU and RENU2 [Harrington, 2017, Lessard, 2019] sounding rockets.

The STA is at TRL 6, except for the gate. While the gating design is straightforward, it is a new addition to a standard instrument design. The gate design has been simulated and a prototype circuit has been built and tested during Phase A. The development to bring the design

to TRL 6 is described in §F.4.

STA Environmental Effects. The MCPs are susceptible to hydrocarbon deposition, particulates and humidity. Therefore, the instrument will have red-tag removed before flight covers and once on orbit, will be given a chance to out-gas before it is turned on. In flight, the thrusters are directed away from the instrument. The thrusters will not be fired when the instrument is operated during science mode.

STA is not highly sensitive to S/C magnetic fields or to EMI. All exterior apertures of STA, and the CubeSat are covered by grounded grids or surfaces for stray field suppression and payload potential control.

The STA electronics is designed for the expected radiation dose of 9.1 kRads. Energetic radiation belt particles will penetrate the instrument and cause background counts on the MCP. Because penetrating radiation causes an isotropic and energy independent background, and our signal is highly peaked in both energy and angle, STA can tolerate a significant background rate. A uniform background rate a factor of 100 below the peak rate would still allow the peak shape to be determined. Large background rates in the region of interest will be uncommon. The auroral arcs are at higher latitudes than the radiation belts most of the time. Contamination in the lower latitude portion of the Science region can be tolerated. Occasional Solar Energetic Particle (SEP) events will also cause penetrating particle background, and reduce the S/N for the duration of the event. UV can also be a source of background for MCP's. The UV is mitigated by coating the ESA plates with Epner Laser Black.

Low energy ion distribution measurements, such as those measured by the STA, are affected by the S/C potential by changing the energy of the incoming ions. In LEO, S/C charging can reach tens of Volts if care is not taken to avoid exposed voltages on the S/C. For objects without exposed voltages, even in sunlight at LEO, the payload charging is expected to be of order five times the ambient electron temperature (Kelley, 1989). For ARCS, STA places a strict requirement on the S/C of no exposed voltages (Table F-1, STA related requirements in column SDR). The STA energy range and resolution (Table E-3) have been chosen to mitigate the impact of the expected S/C charging. Although

engineering considerations of S/C charging are well documented [Garrett, 2001], we have quantified the expected charging levels by modeling the ARCS charging environment using a realistic S/C, including its solar panels, with realistic plasma flows and a typical auroral zone ambient electron temperature of 3036K, using the EU-PICC [Averkin and Gatsonis, 2018] and SPIS Codes [Sarraih et al., 2015]. The results from EU-PICC are shown in Figure E-4. The modeled S/C potential is -0.7 V and the potential contours on the ram-facing (+y) side are smooth. STA performance exceeds requirements in the face of potentials as strong as -5V based on the energy range of STA and shown in the next section. Potentials beyond -5V are prevented by eliminating exposed voltages (§F.2.4.5 and §E.3.1.5).

STA Expected Performance. Simulations of the instrument response at one deflection voltage (-1.8 V) and one angle in the entrance plane, but covering the full range of elevation angles are shown in Figure E-5. Figure E-5a, the combined energy-elevation angle response, shows the expected dependence of the energy on the elevation angle. Figures E-5b and E-5c demonstrate the <12% energy resolution and the <6° FWHM elevation angular acceptance. Figure E-5d shows the ion focus at the MCP location. The ions are well focused, giving the required angular resolution of better than 3°.

The velocity of the plasma, the key data product from STA, is determined from the energy-angle distributions. Figure E-6a shows an ex-

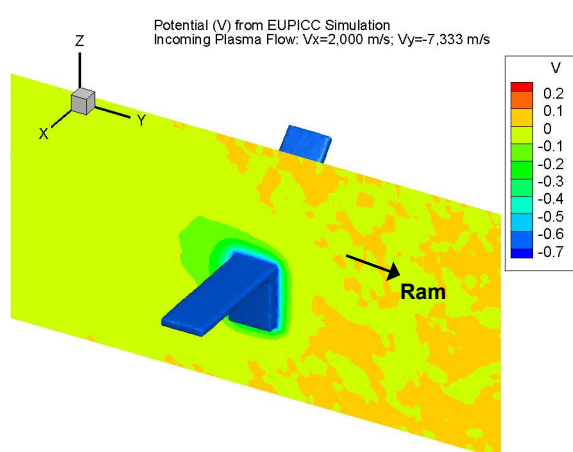


Figure E-4. Simulations of the S/C charging of the ARCS S/C in a realistic environment (no exposed voltages, no solar illumination).

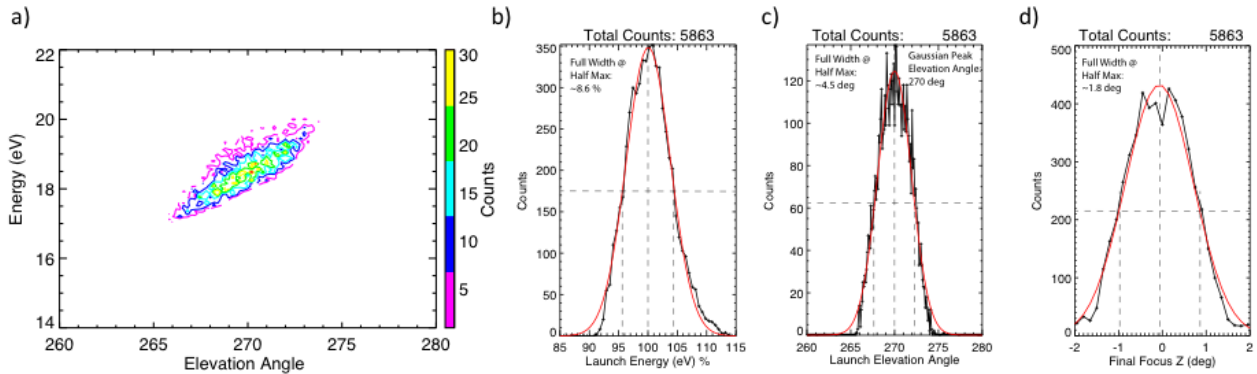


Figure E-5. Energy and elevation angle acceptance of the STA, and the focusing at the MCP.

ample angular distribution of counts in the S/C frame at one energy for a plasma with 1000 m/s flow in the x direction and 50 m/s flow in the z direction, with the S/C moving at 8000 m/s in the y (ram) direction. Because the plasma kinetic temperature thermal velocity is much less than the bulk plasma flow velocity, the distribution is a localized spot. Figure E-6b shows the two slices of this angular distribution available to the two orthogonal STA FOVs. Figures E-6c and E-6d show the energy/angle count distributions for the sensors in the horizontal and vertical orientations, respectively. This is the raw data product provided by the STA sensor that is used to determine the velocity. To first order, the velocity vector is given by the peak location in the two sensors in angle and energy. The challenges in determining the flow velocity come from the large dynamic range and the effects of the S/C potential, which shift the peak. Through a careful choice of geometric factor, optimizing the electronics, and using advanced algorithms to extract the velocity, we are able to meet the required resolution of 300 m/s, and often determine the velocity with an error much better than that.

Figure E-7 shows the expected count rates for distributions at 8 km/s (nominal S/C velocity)

with a S/C potential of -1.5V as a function of energy, covering the range of expected densities and temperatures. Covering the full dynamic range requires a span of 4 orders of magnitude. The resistive anode can measure count rates from 1kHz up to 1 MHz with full position resolution. In order to increase the dynamic range by another order of magnitude the gate can be activated when high rates are detected. When the gate is on, ions do not reach the MCP. The gate voltage is modulated at 500 kHz with a 500 ns on time when high count rates are detected. Figure E-7b compares the count rate in one 1 ms step with the gate off (red) and on (black). While, without the gate the rate would decrease due to deadtime, the gate provides a continuously increasing count rate and low statistical uncertainty up to 10 MHz with only limited distortion.

As the simulations show (Fig.E-4), the S/C potential is normally slightly negative, about -0.7V, but it varies with electron temperature and with auroral precipitation activity [Siddiqui et al, 2011]. A S/C potential on the order of -1 V increases the rammed O+ velocity by around 700 m/s. This is a significant correction to the along-track flow, and so must be taken into account. Fortunately, this information is available

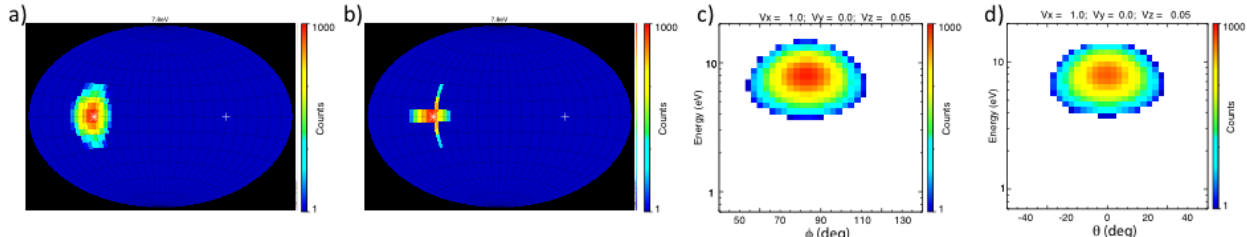


Figure E-6. Demonstration of how the energy-angle distributions measured by STA relate to the full angular distribution. See text for details.

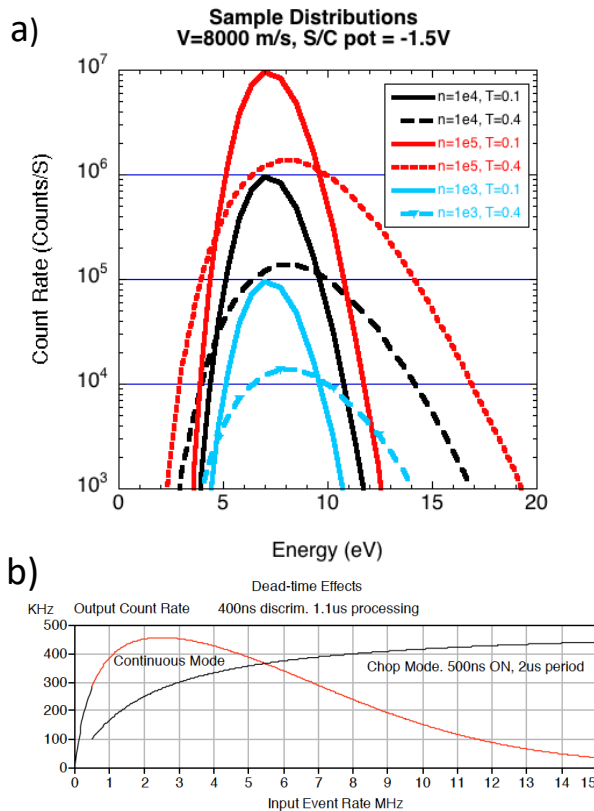


Figure E-7. a) O^+ count rates for STA for conditions spanning the range of expected parameters and b) response to high count rates using the gate.

from the shape of the thermal ion distributions themselves, and so full 2D distribution cuts are telemetered for all science data.

Various features of the distribution shape constrain possible S/C potentials. First, in addition to the dominant O^+ peak there can also be an H^+ peak. At the altitude of ARCS, the H^+ fraction of the plasma varies from 1% to 25% (higher closer to solar minimum). At the same velocities, H^+ has a factor of 16 lower energy than O^+ , and so its nominal energy is well below an eV. The S/C potential accelerates the H^+ , and it is observed at energies just above the potential. The low energy cut-off to determine the S/C po-

tential has been used for both suborbital rocket data in the auroral region [Moore et al., 1996] and on S/C data [Sarno-Smith et al., 2016]. Second, the shape of the O^+ distribution function varies strongly with the potential, so the O^+ distribution cuts alone can be used to determine the potential. Third, the distributions measured by the two sensors on STA both depend on the S/C potential, and the potential must be consistent.

Figure E-8a shows two energy/angle distributions, with an H^+ density 1% of the O^+ , with different combinations of S/C potential and along track flow, but the same centroid location. Once the S/C potential is within the energy range of the instrument ($>0.7\text{V}$) a clear inner edge of the H^+ distribution is observed. This provides information on the S/C potential to within the limit of the energy step size (0.1- 0.2 eV) and the H^+ flow energy (0.1 eV). The flattened low energy edge of the O^+ distribution also varies with the potential. This can be seen more clearly in a 1D cut through the center of the distribution. Figure E-8b shows an examples of three distributions that have the same peak resulting from a different combination of velocity and S/C potential. The blue curve has zero potential and the green curve has the highest potential. The S/C potential steepens the slope on the low energy side. By finding the parameters of a Maxwellian distribution that has the lowest chi-squared difference to the data, the potential, velocity, and temperature can be determined.

Figure E-9 show the statistical error in the velocity that results from the best fit to the distribution for some example environments. The top panels show error in the along-track velocity. On the left, the density is $10^{10}/\text{m}^3$, the nominal value, the S/C potential is -2.0V , and errors are

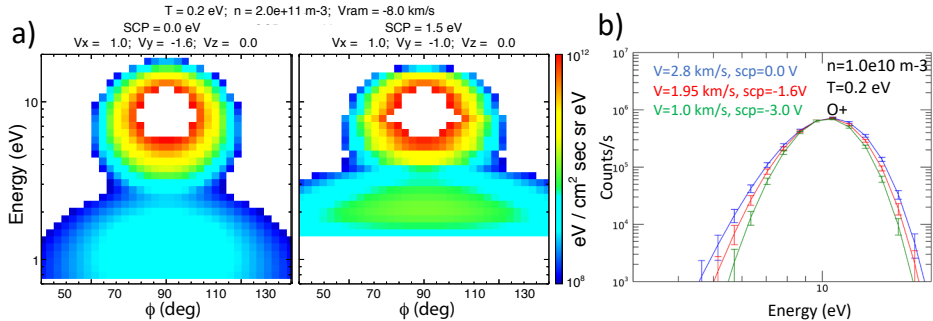


Figure E-8. a) Energy-angle distributions for a plasma with 1% H^+ and 99% O^+ at two different potential and velocity combinations. b) Statistical error in the peak velocity for a range of velocities and temperatures.

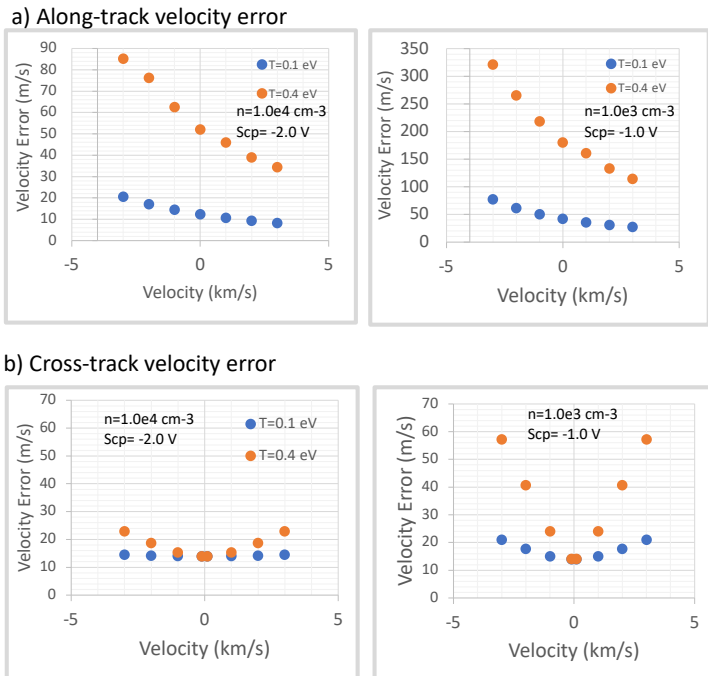


Figure E-9. Errors in a) along-track and b) cross-track velocity under nominal density and S/C charging (scp) conditions (left) and low density conditions (right).

shown for the minimum and maximum expected temperatures, 0.1 eV and 0.4 eV. The errors are significantly better than the requirement of 300 m/s in all cases. The right plot shows the errors for the lowest required density, 10³/m³, for the same two temperatures. Even in this case, the velocity meets the requirement except for the worst combination of lowest density, highest temperature, and strong along-track flow. The bottom panels show the error in the cross-track velocity. Even in the worst case, the cross-track error is well below 60 m/s, and it is below 25 m/s for nominal densities. Typical convection flow magnitudes of interest are hundreds to thousands of m/s. Using both cuts of the distribution from the two STA sensors, and requiring that the potentials and along-track velocities agree, within errors, gives an additional constraint on the allowed parameters. These techniques of fitting to a shifted and drifting Maxwellian, and forward modeling to find the best fit using the two cuts of the distribution strongly constrain the thermal ion population parameters [Fernandes et al., 2016, Fernandes and Lynch, 2016, Roberts et al., 2017, Fraunberger et al., 2020].

E.3.1.3 STA ConOps and Modes

The STA has only two modes, standby and science. Before each science orbit, the instrument turns on in standby mode and the MCP is brought up to operational voltage. Then the instrument enters science mode and data collection begins. At the end of the science pass the instrument exits science mode and the MCP voltage is brought down to minimize fluence on the detectors. The components that see extra stress at turn-on are derated to handle the max stress, so turning on and off three times a day is well within margins.

E.3.1.4 STA Calibration

All the ARCS units are to be characterized at a dedicated ion gun facility at UNH. A low energy ion gun (ILG-6/IGPS-1016) will be purchased from Kimball Physics early in Phase B and installed in existing vacuum chamber facilities. The gun can produce a <20 eV beam of heavy ions with intense enough flux to test the gate operation. The tests of each unit will characterize optimum MCP operating voltage, position linearity and high rate response. To quantify the geometric factor using a well-characterized beam, one unit will also be calibrated at the Marshall Space Flight Center (MSFC) Low-Energy Electron and Ion Facility (LEIF). This facility has been used extensively to characterize charged particle instruments for space flight, including the 32 Dual Ion Spectrometers (DIS), part of the Fast Plasma Instrument (FPI) on MMS. Finally, to test the instrument operation in a flight-like plasma environment, the same unit is to be tested at the Dartmouth microwave plasma source facility [Frederick-Frost and Lynch, 2007; Gayetsky and Lynch, 2011; Siddiqui et al., 2011]. In flight, periodic calibration time periods are planned when the MCP voltage is stepped through a range of values to confirm the optimum operating voltage. Following the experience from SWARM-TII [Knudsen et al., 2017, Lomidze et al., 2019], the rate of efficiency change early in the mission is used to determine the required cadence for routine calibration.

E.3.1.5 STA S/C Accommodations

The required S/C accommodations are summarized in FO1-A. The instrument requires an unobstructed field of view. During Science mode, the STA field of view must be kept centered within 1° of the ram direction. The STA places a requirement on the S/C to eliminate exposed voltages, for example from the solar arrays and their connection points, that could drive the S/C potential significantly more negative [Garrett, 2001] than the -0.7V nominal S/C potential see Figure E-4.

E.3.1.6 STA Plasma Flow Maps

Science Data Product. The STA plasma flow vectors from each S/C are combined across the CubeSwarm array, reconstructing the plasma flow maps (2D flows in the B-perp plane) across the measured area (Science Requirement L1-SR-1). For these electrostatic flows in the known International Geomagnetic Reference Field (IGRF) [Alken et al., 2021] magnetic field, the information is contained in the electric potential field ϕ , as $\mathbf{E} = -\nabla\phi$ and $\mathbf{v} = \mathbf{E} \times \mathbf{B}/B^2$. The flow field reconstruction process generates the electric potential surface for which $-\nabla\phi \times \mathbf{B}/B^2$ best fits the STA data vectors across the space at an 18 s cadence. The flow vectors are then extracted on a fixed-size grid.

Data Map Algorithm/Inversion Technique. The electric potential surface used to reconstruct the flow field is the sum of a set of scalar functions (gaussian-cross-section ridges) each individually parameterized (location, width, amplitude, slope) which each follow a pre-defined arc boundary curve at each timestep. It

is assumed that the reconstructed flow field has minimal variation in the direction along this arc boundary. The arc boundary is derived either from GBO imagery (Scen3) or from the maximum variance direction of the magnetometer data (Scen1 or 2). This constraint allows reconstruction of the flow field between the CubeSat tracks, and in the model space to either side of the CubeSwarm span. The gaussian function set is optimized to best match the data flow vectors in a given collection window (nominally 18 s). Low cadence vectors from before and after the time window are used to constrain the fit.

Figure E-10 shows examples of the reconstruction process as the array moves across a southward-moving arc structure. The measured flow vectors for two 18 s periods are used to create snapshots of the flow structure around the CubeSwarm; this frame is moved as a sliding window as the array moves northward. The left panel shows the (eastward component of) GEMINI model flow field for the first time step, overlaid with black feather plots indicating an 18 s collection of measured flow vectors from the CubeSwarm (decimated for clarity). The second panel shows the optimized electric potential field found for the first of the two time steps illustrated. The two right panels show two flow reconstructions as the CubeSwarm crosses an auroral arc. The blue and red arrows indicate low cadence velocity vectors from times before and after the window. The black vectors shown are again the measured vector flow field, but now the colormap illustrates the (eastward component of the) reconstructed flow field. Good agreement is seen between the original flow and

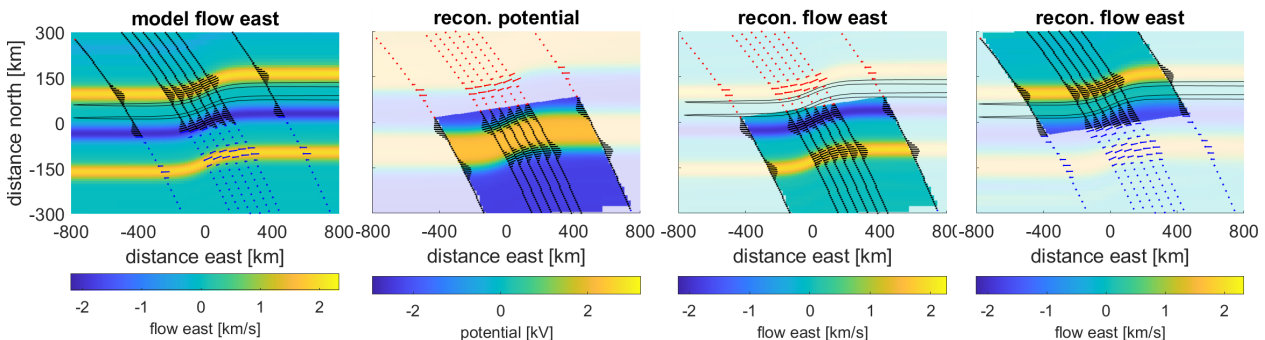


Figure E-10. Flow map reconstruction examples for two times as the array crosses a southward-moving (120 m/s) flow structure. (left panel) GEMINI model flow field. (2nd panel) Reconstructed electrostatic potential field. (right panels) Reconstructed flow field at two time steps. The RMS metric for the first example is 3%; for the second, 8%.

the reconstructed flow, with comparison metric defined below.

Data Map Resolution and Uncertainty. The OSSE formalism allows demonstration of the resulting reconstruction error for different auroral structures at different instrument sample rates, data collection frame rates, varying S/C dropouts, and levels of measurement uncertainty. The goodness of fit of the map is quantified using a pixel-to-pixel root-mean-squared difference of the reconstruction flow field, vs the original GEMINI synthetic datacube flow field, over the trapezoidal area of the CubeSwarm during the 18 s collection period. This metric is provided as a percentage in reference to the maximum flow value inside the collection window. Contributors to this metric include flow measurement uncertainty and also spatial and temporal errors introduced in the reconstruction of the map. Arc structures that move rapidly compared to the 18 s collection, or those having along-arc variation comparable to the inter-track distances, will have larger metric differences. Table E-4 lists a summary chart of STA flow map metric for various situations.

E.3.2 MAG

Auroral Birkeland currents produce magnetic signals above the ionosphere according to Ampere's law, $\mu_0 \mathbf{J} = \nabla \times \mathbf{B}$, where μ_0 is the permeability of free space, \mathbf{J} is the current density vector, and \mathbf{B} is the magnetic field. At auroral latitudes at ARCS altitude, \mathbf{J} is closely aligned with the background main field where $B \sim 50,000$ nT and \mathbf{B} is roughly vertical. The currents are determined from the magnetic field signals transverse to the main field, as has been done for many years to characterize the large-scale Birkeland currents [e.g. Zmuda and Armstrong,

1974; Iijima and Potemra, 1976; Anderson et al., 2014]. Currents on the narrower auroral arc scales include intense arcs with current densities from $1 \mu\text{A}/\text{m}^2$ to over $10 \mu\text{A}/\text{m}^2$ [Gjerloev et al., 2011; Lühr et al., 2015] on scales of ~ 10 km yielding typical magnetic signals of 20 to 200 nT or higher in intense arcs.

E.3.2.1 MAG Requirements

The primary observational objective for MAG is the determination of the auroral field-aligned current density over the CubeSwarm array. The magnetic field at ARCS orbit altitude in the polar regions ranges up to $\sim 50,000$ nT, so the full-scale range for MAG must be at least this high with margin. In addition, the objective requires a vector magnetic field measurement to allow transformation into coordinates parallel and perpendicular to the background field (instrument specifications in FO1-B).

The resolution and noise upper limit are driven by the need to detect currents from even relatively weak auroral arcs. To do this, MAG needs to be able to resolve signals at least as small as 10 nT transverse to the background magnetic field and distinguish them from the background Baseline variations over relatively short time scales, less than ~ 10 s (80 km along track). This implies a 10 nT total budget for the measurement resolution and uncorrectable magnetic field noise. To resolve signatures of structures as narrow as ~ 1 km, the measurement rate must be at least 8 vector samples per second.

The stability and accuracy of the measurements are driven by the need to place the ARCS observations in context of the large-scale currents, for which an accuracy of $\sim 20\%$ is desired. To measure typical current densities of $1 \mu\text{A}/\text{m}^2$ to 20% requires that the observations resolve current densities of $0.2 \mu\text{A}/\text{m}^2$ over the Baseline between CubeSats in the same orbit plane. An along track S/C separation of 18 s corresponds to a 144 km spatial separation and a current density $0.2 \mu\text{A}/\text{m}^2$ over that distance gives a magnetic field change of 36 nT so this is the difference in the field between successive ARCS satellites that must be resolvable. This imposes a requirement to resolve transverse signals to at least 2 parts in 10^4 in the presence of a 50,000 nT field. Since this is the net error in the difference between measurements, this implies a $1/\sqrt{2}$ accuracy error for individual measurements and

Table E-4: STA flow field metrics

Situation	Measurement Error	Median RMS Metric
Nominal	None	5.2%
Fast Motion	None	6.3%
8 Dropped S/C	None	5.3% to 6.6%
16 Dropped S/C	None	6.4% to 8.5%
Random noise added	15-300 m/s	10%
Nominal systematic error	15-50 m/s	10%
Large systemic error	300 m/s	20%
MAG maximum variance boundary	None	5.8% to 20.0%

Notice: Use or disclosure of the proprietary and competition sensitive material on this page is subject to the proposal title page restriction.

an accuracy error budget of 20 nT. The error budget accounts for: Stability in gain and zero levels in a 50,000 nT field over each science pass; Contribution of attitude knowledge uncertainty to errors in magnetic field knowledge between satellites; Knowledge of S/C-generated field; Inter-calibration of magnetometers consisting of gain (including temperature dependence), orientation, non-orthogonality, and offsets (including temperature dependence).

E.3.2.2 MAG Instrument Design

ARCS-MAG is a dual ring core tri-axial digital fluxgate instrument with low intrinsic noise, high sensitivity, and high stability. The sensor uses flight-proven 6-81 permalloy ring cores with $<30 \text{ pT}/\sqrt{\text{Hz}}$ at 1 Hz intrinsic noise and a compact mechanical design. The miniature electronics is the Austrian Space Research Institute (IWF) design based on the Application Specific Integrated Circuit (ASIC) digital fluxgate electronics flown on MMS for the Digital Fluxgate Magnetometer (DFG) and GEO-KOMPSAT 2A (SOSMAG). ARCS uses the fourth generation Magnetometer Front-end ASIC (MFA-4) to accommodate Earth-field operation. The MFA-4 provides 128 vector samples per second with 18 bit digital output resolution spanning $\pm 65,000$ nT, corresponding to 0.5 nT per least significant bit.

MAG Sensor. The key to high performance fluxgates is the ring core and JHU/APL has a stock of over 200 ultra low-noise 6-81 permalloy fluxgate ring cores. The sensor configuration is an adaptation of an APL design flown on the ACES 1 and 2 sounding rockets [Cohen et al., 2013]. The ARCS sensor is shown in FO1 and uses standard materials in a compact design with mechanical rigidity and thermal uniformity. One ring core has null/pickup windings in two directions and the second ring core has null/pickup windings to sense the third direction. For ARCS, the ring core bobbins and frame are made of carbon-filled PEEK to ensure thermal conductivity and mechanical strength.

MAG Electronics & Data Processing. The electronics uses the IWF-developed MMS design with full-scale of $\pm 65,000$ nT. The MFA-4 chip accommodates Earth field range without the additional amplifiers required for SOSMAG. The MFA-4 development at IWF progressed smoothly since the fall of 2020 so that

we are confident in adopting it as the Baseline for ARCS-MAG. This is advantageous since that the board size and layout are the same as for MMS (i.e., simplified relative to SOSMAG), providing power and mass savings relative to the Step 1 proposal. Performance characteristics are listed in Table E-5. Instrument testing and operation are simplified by single mode operation without a processor or software. The MFA-4 also includes up to eight housekeeping A/D channels used in MAG for temperature sensors: three in the magnetometer sensor to monitor temperature variations related to offset variations in the sensor with temperature and temperature gradients, and two to three on the boom for tracking boom flexure related to non-uniformity of boom temperature. Other instrument housekeeping include instrument voltages and currents and a heartbeat bit. The FPGA controls the interface including data buffering for transfer to the Interface Control Electronics (ICE), time stamping relative to the 1 PPS, and collecting housekeeping data. Electronics for sense of the fluxgate signal and digitization of the magnetic field and housekeeping data are implemented in the MFA-4 as shown in the instrument functional block diagram (FO1). Data averaging in BM is performed in the ICE and does not require any commanding to ARCS-MAG.

MAG Heritage and TRL. APL has extensive experience in space-flight magnetometer development. APL teamed with the Goddard Space Flight Center (GSFC) on fluxgates for AMPTE/CCE, Freja, UARS, NEAR and MESSENGER for which APL built the A/D, power and interface electronics and either interfaced with GSFC

Table E-5: MAG Requirements and Performance		
Observation Objective	Requirement	Design/Performance
Electric current, field-aligned	Vector magnetic field	Triaxial fluxgate sensor
Low Earth orbit	$\pm 50,000$ nT	$\pm 65,000$ nT
Large-scale Birke-land currents: 1 mA/m ² to $\sim 20\%$	21 nT accuracy each satellite	20 arc sec attitude knowledge: 4.8 nT 0.01° boom stability: 8.7 nT Bus B-field residual: 2 nT Calibration uncertainty: 7.1 nT Net RSS dB: 12.4 nT
Arc-scale currents: ~ 10 km; 10 $\mu\text{A}/\text{m}^2$ to $\sim 10\%$	12 nT resolution, noise below 12 nT on 1 to 2s time scales	0.5 nT resolution Bus B-field short time-scale (1 to 2s) noise: 2 nT 128 vectors/s



Pages E-17 through E-20 removed.

The largest sources of random error are the boom stability (estimated to be 0.01° from thermal flexure) and uncertainty in the star camera bore-sight (<20 arc seconds). In a field of 50,000 nT these correspond to projections of up to 8.7 nT and 4.8 nT perpendicular to the field, respectively. Thus, the net uncertainty from bus magnetics, orientation, and internal digitization errors is ~ 10 nT, meeting the science requirement of 21 nT (Table E-6).

E.3.2.6 MAG Field Aligned Current Maps

The primary science data products from MAG are maps of the field-aligned current density. Deriving the current density directly from multi-point magnetometer measurements is feasible if the separations between S/C are small relative to the scale size of the current density gradients [Robert et al., 1998]. Auroral arcs generally have latitudinal scales down to ~ 1 km or even smaller while the longitudinal scales are typically 10-100 km or greater. The separations between the inner six orbit tracks of ARCS are tailored to resolve the longitude scales of most arc forms. Spacing satellites closely enough along track to resolve the smallest-scale arcs is prohibitive because of the number of satellites required and because of the orbit dynamics and propulsion to control them so precisely. ARCS solves this problem by using rapid along track magnetic field sampling to estimate the latitudinal spatial structure of the currents. Succeeding ARCS satellites at 18 s along track separations provide repeated sampling in latitude to quantify the latitudinal scales for which this assumption is valid. This follows on a long tradition of making a quasi-stationarity assumption (e.g., as done for Swarm and AMPERE), but with a repeat interval of 18 s, the assumption of time stationarity is less restrictive by a factor of 35 than the 600 s re-sampling cadence for AMPERE.

MAG On Orbit Calibration and Science Data Processing. The science processing for ARCS uses techniques proven for AMPERE to automate magnetometer inter-calibration of many LEO satellites [cf. Anderson et al., 2021]. The first step in the analysis is to transform the magnetometer data into an orthogonal system with a uniform scale factor using the ground calibrations that include temperature dependence. A high-fidelity model magnetic field (e.g., WMM) is evaluated at the bus location and

transformed into the bus coordinate system using the star camera attitude data. The model and observed time series from the BM data over the entire orbit are then compared using 24 hours of data to determine systematic differences in the gain and sensor-to-bus transformation, providing intercalibration across the CubeSwarm to 0.01%. The residuals between the calibrated field data and the model field are then calculated and used to examine any correlations with sensor and boom temperatures not removed in the calibrations and to test for signals from other bus subsystems not identified in pre-flight testing.

The resulting residuals relative to the model field are then transformed into geophysical systems, including Earth Centered Inertial, Geographic, and Geomagnetic systems. These residuals, here denoted $\delta\mathbf{B}$, are the basis for ARCS science processing.

Science Data Product. The original method to estimate field-aligned current from a time series $\delta\mathbf{B}$ is to construct a pseudo gradient in the along-track direction, assuming that the along track variations are spatial gradients. In this original approach, one must assume that the currents are in the form of infinite sheets. The inversions for global Birkeland current distributions from AMPERE use a spherical harmonic fit applied to the $\delta\mathbf{B}$ and the radial current density is calculated analytically from the harmonic fit using recursion relations [Waters et al., 2020]. For ARCS we use the AMPERE regularization technique “to fill” in between ARCS tracks, but with a more sophisticated interpolation approach that allows curved arcs along which the $\delta\mathbf{B}$ are interpolated. The J_z is then evaluated by taking the curl of this dense grid of mapped $\delta\mathbf{B}$.

Results of the ARCS inversion for an OSSE run is shown in Figure E-15. The left panel shows the $J_{z,\text{Input}}$ from GEMINI and the inversion, $J_{z,\text{Inversion}}$, is shown in the center panels. Agreement is assessed by taking the product, $J_{z,\text{prod}} = J_{z,\text{Input}} J_{z,\text{Inversion}}$, and constructing $J_{zA} = \text{sign}(J_{z,\text{prod}}) \sqrt{|J_{z,\text{prod}}|}$, shown in the right panel, which is positive where the signs agree and whose magnitude is the geometric mean of the input and inversion results.

Data Map Algorithm/Inversion Technique. The time separation of 18 s between successive CubeSwarm satellites in a given orbit track defines the accumulation time required for contin-

uous latitude sampling across the CubeSwarm. Because the current density is calculated from the curl of the horizontal $\delta\mathbf{B}$, the interpolation between tracks must ensure that there are no discontinuities in either the locations of the $\delta\mathbf{B}$ samples or in the along track $\delta\mathbf{B}$ used for the interpolation. Because the Earth rotates under the satellite orbits, the geographic locations of successive satellites in an orbit plane do not line up but are shifted slightly in longitude, for example.

To eliminate discontinuities in both the positions and $\delta\mathbf{B}$ in the composite track data, data from each satellite are used that extend before and after the 18 s time window so that the tracks of successive satellites in each track have some overlap. The overlapping segments of data allow a smooth transition between the tracks and data from successive satellites. Picking the center of the overlap as a reference location, denoted as y_0 , the Fermi function, $f(y) = 1/(1 + \exp(-(y-y_0)/D))$, goes smoothly from 0, for $y \ll y_0$, to 1, for $y \gg y_0$, with a transition width in y of $\sim 4D$. Denoting data from the leading and trailing satellites by $\mathbf{d}\mathbf{B}_L$ and $\mathbf{d}\mathbf{B}_T$, the weighted average, $f(y)\mathbf{d}\mathbf{B}_L(y) + (1 - f(y))\mathbf{d}\mathbf{B}_T(y)$, provides a discontinuity-free transition through the overlap between successive satellites. Using the same weighted average on the track X-coordinate through the overlap produces a smooth composite track geometry as well. We used $D = 5$ km so the transition occurs over ~ 20 km, corresponding to ~ 3 s along track.

For each time step in the OSSE runs, the composite tracks and $\delta\mathbf{B}$ were evaluated. To derive a map of the $\delta\mathbf{B}$ between ARCS tracks we used

the observed $\delta\mathbf{B}$ variance for each track to construct curved paths between tracks that follow the dominant orientation of the arcs and continuously join adjacent the tracks following these curves. The points were then evaluated at 1 km intervals to obtain a regular gridded interpolated map of $\delta\mathbf{B}$. The map of J_z was then calculated from the finite difference curl of the mapped $\delta\mathbf{B}$, shown in Figure E-15. To assess the extent of unphysical artifacts in the mapped $\delta\mathbf{B}$ we also evaluate $\nabla \cdot \delta\mathbf{B}$. For the OSSE runs performed, $\nabla \cdot \delta\mathbf{B}$ remained below 10% of J_z and was generally near 1%.

Data Map Resolution and Uncertainty. The curved-path dense interpolation scheme remarkably well reproduces the patterns of the simulated J_z . The right hand panel of Figure E-15 confirms that the vast majority of the area has the right sign of the current. This means that the inversion reliably captures the transitions between upward and downward current, which is critical for assessing the relationships between flows, density, and auroral emissions. An additional measure of the inversion accuracy are shown in Figure E-16.

The linear regression comparison confirms the good agreement, with a regression coefficient of 0.92 and a linear fit slope of 0.72, implying an average under-estimate of the current by $\sim 30\%$. This can actually be assessed and corrected for by evaluating the $\delta\mathbf{B}$ along the tracks using the inverted J_z and comparing those against the measured $\delta\mathbf{B}$. The reliability of the patterns is confirmed in the right hand panels. The Overlap fraction falls off gradually as the Threshold current density increases, reflecting the decrease in

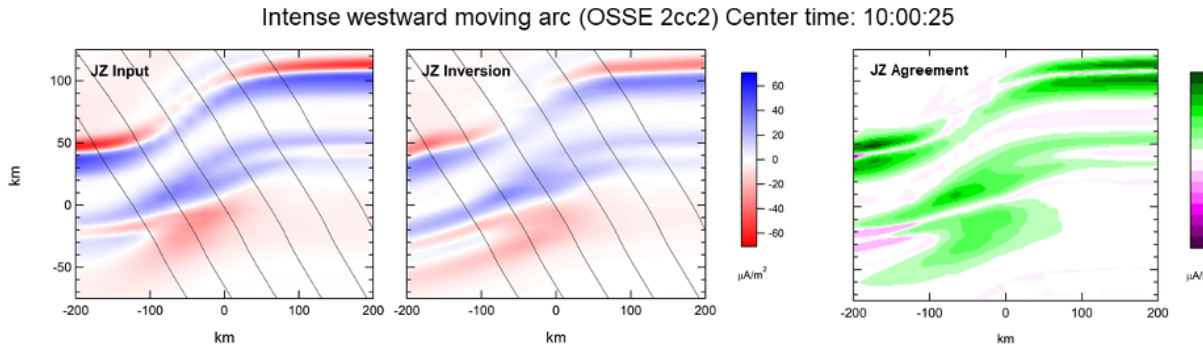


Figure E-15. Simulated field-aligned current density from GEMINI for a westward moving intense arc (left, JZ Input), current density generated from magnetic field data calculated along segments of ARCS orbit tracks (center, JZ Inversion), and convolution of the input and inversion results quantifying the agreement (right, JZ Agreement). The six inner tracks are shown by the black traces.

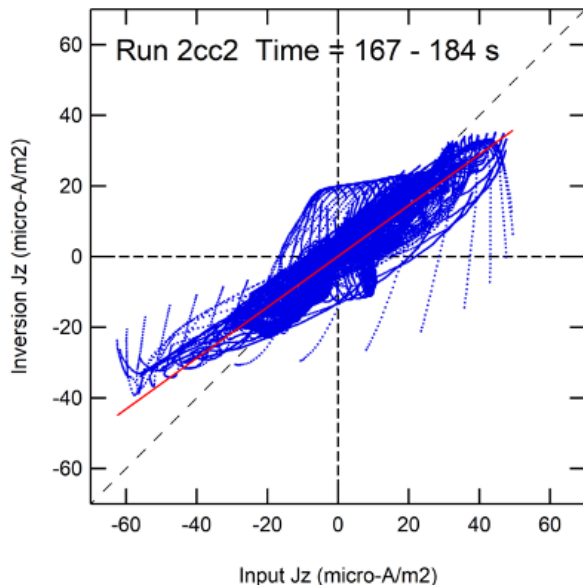


Figure E-16. Metrics of the current density inversion results for the intense auroral case, showing the reconstructed J_z versus the input J_z (blue dots) together with the linear fit (red line) and a 1:1 line (dashed).

area with increasing current density. The most significant feature is that the ‘Error/Overlap’ decreases more rapidly than the Overlap area, showing that the reliability of locating the currents increases with increasing current density. We conclude that the inversion technique is 90% reliable for reproducing the J_z patterns and at least 70% reliable in quantifying the current densities.

E.3.3 Electron density TOMography and Scintillation (eTOMS)

The eTOMS radio beacon transmitter/receiver system (FO1-D) measures the ionosphere total electron content (TEC) and radio scintillation along lines of sight between the GBO and the CubeSwarm array via remote sensing. Similar to Doppler Orbitography and Radio positioning Integrated by Satellite (DORIS) beacon system [Tavernier et al., 2005, Willies et al., 2007, 2010], the eTOMS is a dual-frequency beacon system operating at UHF (400-470 MHz) and S-band (2025-2120 MHz). The differential phase experienced by eTOMS’ radio signals resulting from dispersive propagation properties of the ionosphere [e.g., Heise et al., 2002] is proportional to the TEC along the signal ray path or line of sight (LOS) between each transmitter/re-

ceiver set. Volumetric ionospheric electron density is obtained from tomographic reconstruction of TEC estimated from differential phase contributing to two of the ARCS SOs (SO2 and SO3) and L1 requirement L1.SR-3. In addition, eTOMS 50-Hz measurements provide radio scintillation information resulting from km-scale irregularities in the auroral ionosphere.

E.3.3.1 eTOMS Requirement

eTOMS requirements are driven by the primary observational objective that it supports which is the determination of the ionosphere electron density over the region covered by the CubeSwarm array. eTOMS is slated to provide information on electron density in both winter and summer seasons in the auroral ionosphere over Alaska, where the electron density can increase up to $1 \times 10^{12} \text{ el/m}^3$. eTOMS requires a dynamic range that covers the corresponding line-of-sight TEC values (up to $\sim 50 \text{ TECU}$), hence it is required to measure the group time delay up to about 400 nm for the UHF band. The accuracy of the measurements are driven by the need to determine the electron density with 1σ accuracy of $1 \times 10^{11} \text{ el/m}^3$, which amounts to 10° 1σ phase error corresponding to 0.02 relative TECU accuracy. The requirement on sensitivity of the received signal is driven by the 10° phase error, which requires the link budget to close at after -129 dBm. Each eTOMS receiver is required to be able to receive dual-frequency signals from at least six eTOMS ground transmitters (STM in Table D-1) to accumulate diverse sets of rays used for tomographic electron density reconstruction. The requirements and performance characteristics are summarized in Table E-7. The performance characteristics are demonstrated in §E.3.3.2.

E.3.3.2 eTOMS Instrument Design

eTOMS Sensor. The eTOMS instrument comprises dual frequency receiver electronics and an antenna operating at UHF and S-band. Ground transmitters developed and deployed for this application provide the dual-frequency signal sources required to close the eTOMS RF link.

eTOMS Electronics. The receiver electronics is a single board assembly packaged in an Aluminum housing with bulkhead RF connections to a patch antenna and data/power connections



Pages E-24 through E-27 removed.

E.3.3.3 eTOMS ConOps and Modes

The eTOMS receiver can simultaneously acquire signals from 9 dual-frequency stations (18 channels or pseudocodes in total), from a predetermined table of up to 32 unique pseudocodes. The eTOMS transmitters are located at 24 of the GBO sites and are activated during ARCS passes over Alaska in the pre-midnight sector. Each eTOMS receiver has a prioritized list of ground station signals (9 of 32 possible pseudocodes), unique to each S/C, acquired during the pass and based on the stations that optimize the electron density tomography data product. A total of 24 transmitters will simultaneously operate through each ARCS pass over Alaska, and each eTOMS instrument will acquire dual frequency signals from the top 9-sites based on their pre-determined priority table, ignoring stations on the list having SNR below a predetermined Threshold. The prioritized lists are determined and uploaded as stored time-tagged instrument command macros through the normal S/C RF command link. The repeating Alaska pre-midnight ground track allows a Baseline configuration to be used throughout the mission, with a contingency for commanded configuration changes as necessary. It is expected that the prioritized list for any given S/C will change infrequently throughout the mission. The station IDs associated with all links are stored in eTOMS housekeeping data. The eTOMS science collection timeline is described in Table E-2.

E.3.3.4 eTOMS Calibration

Calibration of eTOMS prior to launch consists of precise measurement of relative gain, phase, and time delay for both receiver frequency channels over the full operating temperature range using APL RF enclosures and calibrated coaxial attenuators; this provides a calibration factor for absolute instrument bias, differential biases between the two frequency channels within each eTOMS instrument as well as across all eTOMS instruments. There are no radiation or aging-related effects on these biases. Each ground transmitter's relative amplitude, time delays, and phase shifts are also characterized prior to installation. These calibrations, along with the on-orbit measurement of pseudorange and differential phase, provide the full data set required for calculation of absolute TEC. Non-fractional frequency synthesis and integer clock relation-

ships in the transmitter and receiver electronics designs provide repeatable instrument bias across multiple link closures and power cycles.

E.3.3.5 eTOMS S/C Accommodations

eTOMS requires an obstruction-free field of view from the antenna to at least 66° from boresight. This allows for minimum disturbance to the antenna gain pattern and RF link performance. An analysis and test will be performed in Phase B to further refine antenna performance with a high fidelity mechanical model of the S/C structure, including the MAG boom. The low-gain eTOMS antenna patterns on both the S/C and ground transmitters facilitate the wide field of view required to close the eTOMS RF links without imposing an eTOMS pointing constraint.

E.3.3.6 eTOMS 3D Electron Density Maps

Science Data Product. The eTOMS instrument acquires differential phase measurements from two radio frequencies at UHF and S-bands to determine the ionosphere TEC along lines of sight, which are used to determine the volumetric density and is projected to meet ARCS measurement requirement as described in §E.3.3.1. The eTOMS reconstructions base-lined for every 60 s will provide the regional context of the ionosphere for in-situ ARCS measurements. The inversion technique is applied on the data from all eTOMS receivers each acquiring signals from up to 9 different ground transmitters. The eTOMS L1 science requirement (L1-SR-3) is to produce volumetric (3D) maps of electron densities in the pre-midnight sector auroral zone over the GBO array, as a moving mosaic along the S/C overpass (§E.1). The analysis below shows that the multi-point eTOMS measurements meet the L1 science requirements.

Data Map Algorithm/Inversion Technique. Since the relationship between the slant TEC along the line-of-sight and the underlying density is linear tomographic techniques [Karl, 2005; Vogel et al., 2002] can be used to invert this linear system of equations. The tomographic techniques that have been extensively developed for GPS and beacon data processing are leveraged for eTOMS data inversion. We leverage the procedures that have been developed [e.g., Austen et al., 1988; Bernhardt et al., 1998, 2000; Bernhardt and Siefring, 2006; Vierinen

et al., 2014]. The ionosphere beacon tomography is inherently a limited angle tomography problem, and hence requires application of constraints in the form of a priori information in the framework of statistical linear inverse problems to stabilize the solution in the presence of noise [e.g., Vogel and Oman, 1996, Kamalabadi et al., 1999, Vogel, 2002, Karl, 2005, Nikoukar et al., 2008, 2010, 2012, 2015]. To assess the data quality, the first step is the preprocessing of the data to determine slant TEC from differential phase, as described in §E.3.3.2, from “flying through” the OSSE simulated aurora (Fig. E-19a). The second step is to estimate the error representing the deviation of the reconstructed densities from the OSSE simulated aurora. The data quality of reconstructed electron density produced by eTOMS transmitter/receiver system is dependent on the instrument performance, the number and orientation of overlapping radio paths with respect to each other (observing geometry) determined by the number of satellites and their relative locations with respect to the ground transmitters, as well as complexity of the auroral structure. With the accumulated TEC data from at least six ground stations for each S/C along each track for 60s together with the S/C and ground transmitters positions, a map of electron density is created. To do this, we first discretize the underlying volume by adopting a non-uniform spacing in altitude based on ionosphere scale height (10–20 km in the E-region and 40 km above). To determine the discretization grid parameters

from the OSSE experiment, generalized cross validation [e.g., Craven and Wahba 1978, Sharif and Kamalabadi 2005, Lee et al. 2007] which basically would amount to optimization of cost function to estimate the predictive risk can be used. Since auroral arcs have typically a much more limited latitudinal span than a longitudinal span, it is imperative to have a finer latitudinal spacing. The generalized cross validation method yields latitudinal and longitudinal spacing of $\sim 0.2^\circ$ and $\sim 1^\circ$, respectively. The next step is to develop a forward model for the observation geometry based on the length of each ray path passing through the discretization grid for every 60s, which relates the TEC measurements to the density volume. The final step is the linear inversion of the matrix equation to determine the density which in turn amounts to optimization of a constrained cost function. Edge-preserving constraints are applied to be able to allow for detection of sharp enhancements due to auroral precipitation, while stabilizing the solution due to noise [Lee et al., 2008, Nikoukar et al., 2010]. The application of other constrained optimization such as reference constraints [e.g., Lee et al., 2007] which can utilize information on the edge of auroral arcs (from MAG or ML, for example) or parametric inversion techniques is envisioned as phase B to pre-launch science activities. Together with ARCS in-situ measurements, the 3D electron density estimates can be used to derive auroral precipitation parameters as discussed in §D.6.2.

Ground transmitters placement. To maxi-

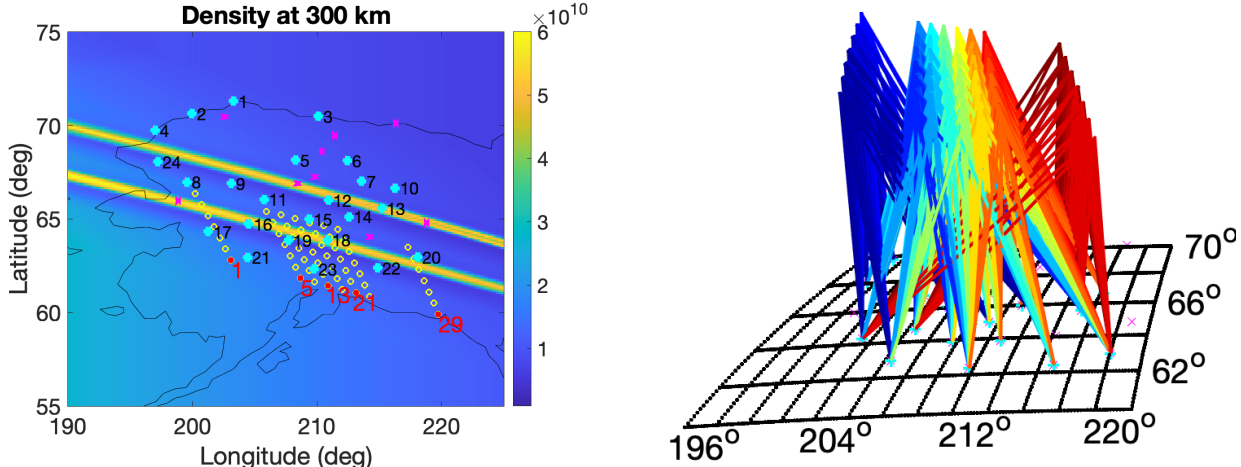


Figure E-19. (left) Set of 24 ground stations that enable a diverse set of ray paths (cyan), while the rest of ground stations shown in magenta. (right) A subset of ray paths and their coverage between the CubeSwarm and GBOs with each shade representing a distinct S/C.

mize the science return from eTOMS, it is envisioned to host eTOMS ground transmitters on 24 of GBO stations and that S/C along adjacent tracks receive the signal from a set of different ground stations. To avoid the exhaustive search for the optimal set of ground stations, application of previously developed techniques in optimal experiment design such as backward, forward, or greedy algorithms, sequential backward selection, or Clustered sequential backward selection [e.g., Sharif and Kamalabdi, 2008, Reeves and Zhe, 1999, and references therein], will be examined. A candidate set of 24 ground stations that enable a diverse set of ray paths are depicted in Figure E-19a (cyan pluses). The set of ground stations not hosting eTOMS transmitters in this example are noted by magenta crosses. The background image is the latitude-longitude of the model OSSE with a stationary two-arc structure at 300 km. The satellite positions are shown by yellow circles. The red text shows the numbers of the first satellites in each track. Figure E-19b shows a subset of ray paths and their coverage between the ARCS S/C and the ground stations (each S/C tracking up to 9 stations) with each shade representing a distinct S/C.

Data Map Resolution and Uncertainty. Within the OSSE framework, we can demonstrate the reconstructed maps and their associ-

ated errors for various auroral structures for different time intervals over the pass, varying number of S/C dropouts, and level of measurement uncertainty. Figure E-20 shows examples of reconstructed density with the discretization grid specified above for both 3D and a latitude-altitude 2D cut at 210° longitude for the observing geometry shown in Figure E-19a. Due to limitations imposed by the number of tracking channels for each S/C (maximum 9), eTOMS antenna FOV, as well as the observing geometry imposed by the tilted satellite tracks aligned with magnetic latitude, and the application of constrained tomography, the E-region density enhancements are slightly blurred over approximately 0.6° (3 adjacent voxels) latitude range. The white areas in the plots show the regions for which no overlapping rays pass through hence the corresponding voxels cannot be reconstructed.

One metric that can be used to quantify the goodness of map is a normalized voxel-to-voxel root-mean-squared difference of the reconstructed density, vs the original GEMINI synthetic density over the entire grid voxels that can be reconstructed with the particular observing geometry. This metric is provided as the percentage in reference to the maximum original density within the reconstructable voxels. Contributors to this error metric include measure-

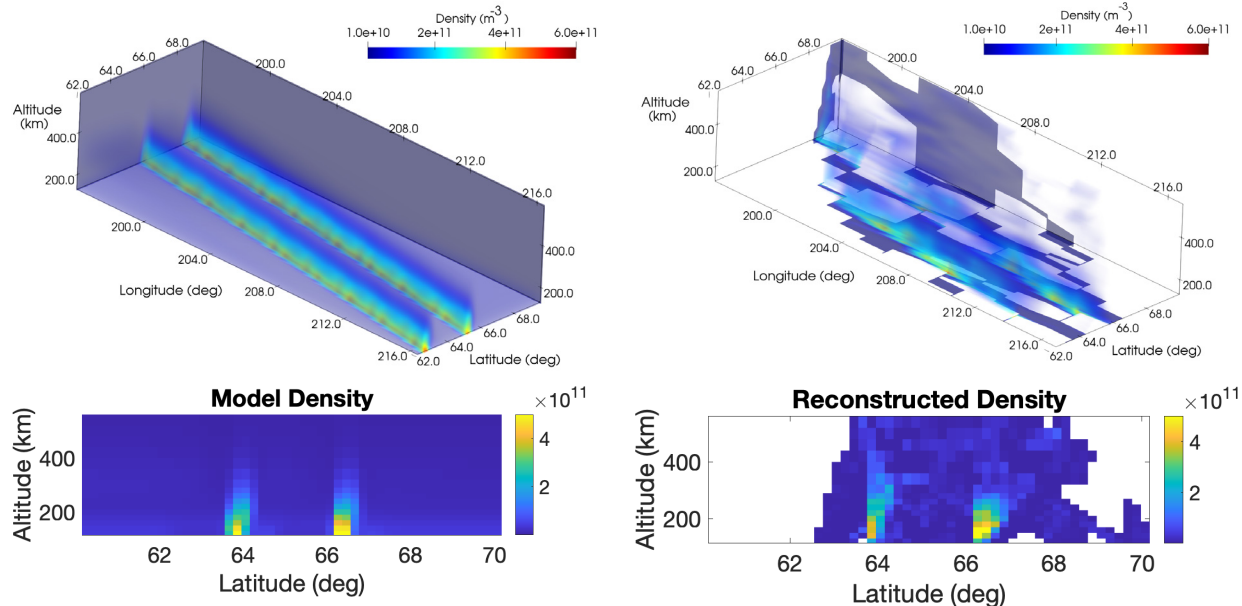


Figure E-20. 3D electron density reconstructions for the observation geometry shown in Figure E-19a. comparing original data cube (left) to reconstructed data (right)

Notice: Use or disclosure of the proprietary and competition sensitive material on this page is subject to the proposal title page restriction.

ment uncertainty, the relation between the ray paths accumulation time and the speed of moving arc structures, the spatial resolution of the grid relative to auroral structure spatial distribution. The inversion framework treats the underlying ionosphere as stationary for the ray path accumulation period, so the reconstructed density maps will be an average of the ionosphere density over the accumulation period (60s).

eTOMS Scintillation Maps. Scintillation indices (S_4 and σ_ϕ) obtained from eTOMS can be overplotted on All Sky Images (ASIs) to derive “scintillation maps.” The indices would be plotted at the ionospheric pierce point locations obtained at a height estimated from line green/red emissions in the ASI data [e.g., Loucks et al., 2017, Semeter et al., 2017]. These maps can be used to identify the approximate locations and strength of scintillation producing irregularities with respect to the auroral arcs. The location of a significant phase or amplitude variation in scintillation data would indicate presence of irregularities of scale sizes on the order of a few hundred meters to a few kilometers.

eTOMS Summary. Table E-8 lists a summary chart of eTOMS density map errors for different auroral scenarios using 60s data collection intervals for different situations for eTOMS nominal errors. The errors are computed based on 50 Monte Carlo realizations.

E.3.4 GBO

Auroral electron precipitation is the major driver of rapid and localized changes in the electron density and conductivity. The GBO will collect data used to create maps of the location, timing and energetics of the auroral precipitation. Each GBO site consists of three main components: a set of instruments; a hermetic, insulated enclosure; and an instrument control assembly (ICA) (FO1-C).

Table E-8: eTOMS Density Resolutions.

Situation	Density Error
stationary 2-arc structure, Baseline	9%
Westward Traveling, Baseline	7%
Westward Traveling - Baseline - Summer	20%
stationary 2-arc structure, Threshold	12%
Westward Traveling, Threshold	10%
Westward Traveling, Threshold - Summer	28%

E.3.4.1 GBO Requirements

The GBO imager requirements flow down from L1 requirements SR-4 and SR-5. The goal is to produce maps at 1 km resolution or better across the entire cross-track extent of the swarm and in the magnetic latitude range of 62° to 72° across Alaska. The technique to invert optical emissions into auroral energy characteristics is best when applied near local zenith, and uncertainties increase away from zenith. All-sky imagers with 1K x 1K pixel resolution can produce 0.5 km pixel scale resolution out to 40° from zenith. These two constraints lead to an optimal site-to-site spacing of 150-200 km, which for the Alaska overflight region results in the need for 30 to 35 sites. The range of auroral precipitation parameters ($\langle E \rangle$ and Q) defines the sensitivity requirements for the imagers. For Q at 5 mW/m², and $\langle E \rangle$ at 20 keV, the expected intensity of the 844.6 nm wavelength is 250 rayleighs, which defines the minimum sensitivity, which we apply to all imagers. The goal of examining changes in auroral forcing at 1 km scales also drives the imager frame rate requirement of 8 Hz during the swarm overpass.

E.3.4.2 GBO Instrument Design

As discussed in §D, we plan to reproduce the auroral electron precipitation characteristics by fielding a dense array of 32 ground sites across northern and central Alaska, each with a set of single-filter imagers (FO1-C). The longitudinal extent of the array spans the 900 km width of the CubeSwarm, and the latitudinal extent (10° in magnetic latitude) enables coverage for a wide range of auroral activity. Every site contains three imagers: 1) a Green Line Camera (GLC) for the 557.7 nm green-line emission of atomic O, 2) a Blue Line Camera (BLC) for the 427.8 nm emission of N2+, and 3) a near infrared camera (8LC) for the 844.6 nm emission of atomic O. A subset of 14 GBOs also operates a Red Line Camera (RLC) for the atomic O emission at 630.0 nm that enables energy flux measurements for very low average energies. eTOMS transmitters are accommodated at 24 GBO sites (FO1-C).

GBO Sensors. The imagers make use of optical designs to maximize the effective collecting area (etendue), and modern high-sensitivity detectors to produce near-theoretical performance for light gathering. In all imagers the output of

a fish-eye lens is collimated for transmission through a narrow-bandwidth interference filter for its particular emission. The collimated beam is then re-imaged onto the 13.3 x 13.3 mm detectors (18.8 mm diagonal). The choice of a large format fish-eye and re-imaging lenses reduces the plate scale to fit on the detector, while increasing the system speed from $\sim f/4$ to $\sim f/1$ in the case of the BLC and 8LC and $\sim f/1.4$ in the case of the GLC and RLC. In all cameras we use backside-thinned detectors that enable detection at near-theoretical limits.

The two most challenging measurement requirements are those for the 427.8 nm and 844.6 nm emissions, for three reasons; 1) Both are typically the dimmest of the four emissions to be collected, 2) the quantum efficiency of even most back-side thinned detectors is not at its peak (typically 30-40% off) and 3) in the case of 427.8 nm, the energy flux calculation is based primarily on this emission (with some secondary methods available). For these two emissions we have chosen to use the same camera design as described in Grubbs [2019a], which consists of a large format front fish-eye optic (based on a Mamiya 6 cm x 4.5 cm format) which is collimated by 3" diameter optics, transferred through a 3" diameter interference filter and re-imaged onto the 13.3 mm x 13.3 mm EMCCD detector using a f/0.95 50 mm lens.

The 3" design provides more performance than is needed for the GLC and the RLC. These cameras will still use a format scaling approach, but will use optics designed for 35 mm DSLR cameras as the fore-optics which are more plentiful and lower cost. Using commercial off-the-shelf optical components, the beam is collimated through a 2-inch diameter filter (again less expensive than the 3-inch filters of the BLC and 8LC) and re-imaged with a machine vision 25 mm lens at f/1.4 onto the 13.3 x 13.3 mm scientific CMOS detector. At these two wavelengths the detector quantum efficiency approaches 95%, and read noise is less than 2 e-.

While the requirement for sampling rate of the cameras is 8 frames per second, we have chosen to run the three main cameras (BLC, GLC and 8LC) at 15 frames per second. In most cases we anticipate that the emission intensities will far exceed the minimum of 250 rayleighs, and by sampling at twice the required rate we can examine the dynamics of rapid auroral motions.

GBO Electronics & Data Processing. All digitization of the analog signals of optical sensors (EMCCD and sCMOS) is done by the COTS imagers. All images are collected at 16 bits per pixel enabling a wide dynamic range. Digital signals from each imager are collected using a dedicated COTS small form-factor mini personal computer. Specifically, we have Baseline an Intel NUC10i7FNH. Images of the EMCCD sensors for the 3" optical design imagers are collected using gigabit ethernet (GigE) interface on one of two redundant network ports, and in the case of sCMOS sensor for the 2" optical design imagers, the images are collected using USB 3.0 interfaces. Both interfaces easily accommodate 15 frames per second at a 1024x1024 pixel image format. For all imaging modes (§E.3.4.3) images will be stored in multi-image Tag Image File Format (TIFF) files, which enables rapid uncompressed image writing to memory, and is used in heritage software for both collection and processing. Data are collected on an internal drive, then transferred via the Instrument Control Assembly processor to a set of redundant storage drives (§E.3.4.3).

GBO Heritage and TRL. The vast majority of components of GBO systems and subsystems are commercial off-the-shelf units requiring no modification or special handling. Mechanically, the only specialized parts are those to mount cameras and components within the enclosure and will not affect instrument performance. Electronically all components, including the detectors, use standard, well-tested interfaces (USB and GigE), and no design of special circuit boards or ICs is required. The 3" imagers are the same KEO Scientific design used extensively in the field [Grubbs et al., 2018a, 2018b]. GI/UAF is developing a 2" version of the 3" imager design for several projects, including ARCS. Initial prototypes in the lab, and recent field observation using the proposed detector (Teledyne Prime BSI Express), indicate the imager system will exceed specifications for ARCS. The enclosure has also been prototyped and thermal tested at cold (-40°C) and warm (+20°C) external operating temperatures and maintained the required internal thermal environment. While TRL is typically applied to space flight instrumentation we characterize the main components of the GBO as: (1) 3" Imager design TRL 9, (2) 2" Imager design TRL 5, (3)

Enclosure TRL 5, and (4) ICA all components are TRL 9 COTS. For the 2" imager design we will use GI/UAF and phase A funding to finalized an engineering model and operate it during the 2021/2022 auroral observing season, which will bring its TRL to 7 or greater by the time of PDR. For the Enclosure, an engineering model will be built and also operated during the 2021/2022 season, with thermal loads matching our expected GBO loads, again bringing the TRL to 7 or greater by PDR.

GBO Environmental Effects. The major environmental effects on the imager performance in the GBOs are 1) obscuration due to moisture inside or outside the dome, and 2) high or low temperature operating environment. Interior moisture control is accomplished with forced-air into the interior of the domes using redundant box fans and ducting. This is used at many remote observing sites to good effect. The thermal environment within the enclosure is driven by the requirements to keep the instruments and electronics within their operational temperature range, and specifically to keep the detector operating temperature cooled to provide optimal performance. This translates to a thermal range of +5 to +25 °C when the external temperature ranges from -50 to +20 °C. Successful tests of an engineering model enclosure are described below. A final environmental effect is obscuration due to clouds. We have included a broad-band low-resolution sky camera to each site that will take an image every 60 s. When returned to the GBOC these images are used to assess the sky conditions at that site.

GBO Expected Performance. Table E-9 shows the expected performance of the imagers to meet their measurement goals. For all key parameters we are exceeding the requirements.

E.3.4.3 GBO ConOps and Modes

The primary function of the GBOs is to collect optical data from the imagers, and for sites with eTOMS transmitters, to transmit during overpasses. After each night of image collection, there is a significant volume of data collected on each camera computer, and a significant amount of the non-imaging periods will be involved in moving the data to multiply redundant storage. Each GBO imager will have three operating modes: Idle, Survey and Burst. The imagers collect data when the solar elevation

Table E-9: GBO Expected Performance						
	Frame Rate (Hz)		Max Pixel Scale at 110 km at 40° from Zenith		Min Sensitivity (Rayleighs)	
	Req	Perf	Req	Perf	Req	Perf
BLC	8	15	0.5 km	0.46 km	250	150
GLC	8	15	0.5 km	0.46 km	250	200
8LC	8	15	0.5 km	0.46 km	250	210
RLC	0.5	2	0.5 km	0.46 km	50	18

Min Sensitivity for BLC, GLC and 8LC are for 8Hz

Min Sensitivity for RLC is for 0.5 Hz

angle (SEA) is <-6° and are in Idle Mode when SEA >-6°. The imagers operate in Burst Mode (Table E-9) during ARCS Science Passes over Alaska, otherwise they operate in Survey Mode (0.2 frames/s). The start and stop times of Burst mode is given in Table E-2.

Off-Season/eTOMS Only. During the off-season each GBO will not be completely powered off. The GBO PC will remain operational as will the Iridium modem. The GBO will continue to operate the eTOMS transmitters during the daily ARCS science passes over Alaska. The PC will primarily monitor thermal environments and implement cooling options if needed.

Data Management. After the end of each observation night, and following calibration data collection, the ICA PC will begin the transfer of data from each imager computer to two classes of storage – transfer storage and resident storage – both of which have redundant drives. The ICA PC will pull from each camera sequentially. Data on the camera computers are only deleted once the images are confirmed on the redundant storage. Thumbnails of a small image subset will be available over low speed internet to assess the data for each ARCS pass. We anticipate that most sites will not support network that will be sufficient to transfer the Burst data in even a 24 hour period, therefore transfer of the full resolution data will be accomplished by using a local caretaker to swap one of the set of redundant transfer drives on a regular basis (nominally every two weeks) and ship the full drives back to UAF/GI for upload to the GBOC.

Each site will maintain enough storage to save a full winter season's worth of images.

Local caretakers. The GBOs are designed to be mostly autonomous, although some operations require human intervention. For example, caretakers will be responsible for removing

snow from the domes that is obscuring the imagers. We have budgeted funds to hire a local caretaker to accomplish these tasks.

Error management. Errors will be monitored using telemetry from the imagers, imager computers and thermal and UPS monitors. For many errors, power cycling will resolve the issue, and we will develop scripts to be initiated either automatically during Burst mode ops or manually by an operator at the GBOC during other modes. In the case that the scripts do not resolve the error, further troubleshooting can be done remotely or with the help of the local caretaker to resolve problems.

E.3.4.4 GBO Imager Calibration

Each imager will require an intensity calibration and a geometric calibration to achieve accurate maps of the auroral precipitation. Acceptance testing of all imagers confirms that both light sensitivity, field of view, and resolution meet requirements, and serves as an initial calibration. More accurate calibrations are accomplished after the imagers are deployed, using stars observed during quiet auroral periods. As described in Grubbs et al. [2016], several catalogs describe the magnitude and spectral type of most bright stars. By matching the observed intensity to the predicted signal of the stars' spectral types as observed in the bandpass for the imagers filter for multiple stars produces the best estimate for the imager calibration. Variations in this calibrated gain can be tracked by observing a few bright stars over the season and the course of one observing night. This can inform us of changes in camera performance or changes in atmospheric conditions during observations. Geometric calibration uses the same star catalogs which define the stars position to arc-second accuracy. Matching the observed position of multiple stars (20 to 50) vs their expected location is used to create a map of the azimuth and elevation of each pixel in each imager to sub arc-minute resolution, sufficient to map the center of a pixel to sub-km accuracy. The software for both calibrations exists and for ARCS the only development is to improve the automation of the routines to reduce the hands-on requirements for the large number of sites.

E.3.4.5 GBO Accommodations

There are two primary requirements for the

enclosure: 1) maintain an internal operating temperature over a wide range of external temperatures and 2) transportability by air using Cessna Grand Caravan aircraft. We engaged a team of senior mechanical engineering students at UAF and mentors from UAF's Cold-Climate Housing Center to fabricate and perform tests on a design for an ARCS enclosure based on our extensive field experience and past enclosures.

Mechanical. Figure E-21 shows the current design: 4' by 8' ground footprint, 8' tall. We make use of structural insulated panels (SIPs), with a 2-inch layer of insulating foam to provide structural integrity and the correct level of insulation. Each panel is wrapped and sealed with membrane prior to assembly in the field. The panels fit through the cargo door of a Grand Caravan. In the field the panels are held together with metal braces, and the membrane surfaces are bonded together to make a hermetic seal.

Siting of the enclosures requires a clear field of view above 50° elevation (80° FOV) as viewed from the top of the enclosures, and minimal intrusions into the field of view above 30° elevation (120° FOV). In many rural Alaska sites the best location for clear views, as well as providing a stabilized foundation, is at state-run airports, and we have submitted 18 applications for placing our GBO enclosures at such sites.



Figure E-21. Prototype GBO Enclosure during cold testing.

Thermal. The most demanding thermal requirement is cooling the enclosure when external temperatures exceed 0°F (-18°C). The insulation needed to survive -50°C conditions means that heat loss through the walls is lower when external temperatures rise and the internal temperatures risk exceeding their limits. Testing of a commercial heat exchange system designed for domestic use shows that it can dump ~1kW of excess heat and maintain operating temperatures when outside temperatures reach 20°C, while not introducing external humidity which might risk frosting of the observing domes. For cold operation we include make-up heaters with sufficient power to maintain enclosure temperature even if the control electronics are powered off.

Observatory Control. The central control of the ICA is a dedicated PC running Linux. The PC sets the local virtual private network that connects via giga-bit network to the imager computers and other IP based components. A GPS receiver will be coupled with the open source Network Time Protocol (NTP) software for Linux to set the system time to sub msec accuracy. The PC will then act as an NTP server for the imager computers which will synchronize their times just prior to swarm overflight. This will provide absolute timing between each camera to a few msec, less than the 67 msec per frame when operating at 15 frames/s. The ICA PC also hosts a USB 3.0 hub for attaching a set of redundant storage and transfer drives. Management of these drives is described in §E.3.4.3. The internal and external temperatures of the GBO enclosure will be monitored every minute, recorded locally and telemetered back to the GBOC as part of the health and status telemetry.

Communications. Each site will have redundant communications systems. In all cases we plan to use an Iridium modem as a failsafe method for confirming and monitoring GBO status. The cost of transmitting quick-look images is prohibitive on this service. The primary network option will depend on the specific site. At sites with local 4G or 3G access, we will contract with providers to use an appropriate modem. At sites without local network access, we will use a satellite network provider (most often Hughesnet in rural AK).

The eTOMS transmitters and processor will

be accommodated in the equipment rack for the ICA. The eTOMS assembly is anticipated to occupy a 4U space in the rack, and we have set aside a 6U space to accommodate air-flow to help maintain thermal stability of the transmitters. The processor will be attached to the local VPN with a unique IP that can be accessed via either the Iridium or satellite/4G modem. We will allocate 4 outlets on the network power switches so that individual components can be power cycled as needed. Two coax cables will be routed through the same access as the GPS and satellite network antennas. The patch antenna will be mounted externally by an APL-provided bracket, and will placed so as not to impede the view of the cameras, and approximately 8 feet from the GPS and satellite network antennas.

For sites that will support the STudent collaboration Auroral Radio Experiment (STARE) we will also set aside a 6U space in the ICA rack, and set aside two outlets on network power switches. Coax cables and power to the receivers will use the same exit port as the eTOMS and satellite networks.

Power Management. Each GBO will use local utility power to run the site. Rural power can be “dirty” and is prone to short-term outages. We include a 3000 VA uninterruptible power supply (UPS) that will condition the incoming power and also provide up to 20 minutes of power for full operations. In the event of a power outage during Burst Mode the ICA will maintain the Burst Mode operations and then gracefully shut down power to the rest of the GBO until power is restored. We also include several network power strips at each site so that power to each component can be controlled individually.

E.3.4.6 GBO Auroral Image Mosaics & Energy Maps

The ARCS data products will consist of aggregate maps of imagery, $\langle E \rangle$, and Q over the span of the GBO. Here we describe how the individual measurement error expands out to aggregated maps, and the tools we use for synthesizing into single distributed maps of information. Of particular interest is how the errors increase as we move from away from zenith toward the spaces between imagers, and how we bridge the different FOVs, especially when a

station is inoperable or cloudy.

Science Data Products. Data from the GBOs will be used to produce mosaic maps of auroral emissions of the entire GBO extent, $\langle E \rangle$, and Q (L1.SR-4 & 5).

Data Map Algorithm/Inversion Technique. Once a camera has been geometrically calibrated with an accurate map of the azimuth and elevation of the center of each pixel, standard spherical geometry algorithms are used to map the intensity of each pixel onto a regular grid of geographic latitude and longitude to establish a common spatial scale. Each emission is mapped based on the typical peak altitude for that emission. These geographically mapped images are then converted to geomagnetic coordinates so that their intensities can be compared by shifting their maps to line up along magnetic field lines, based on their altitude.

The technique for inverting the emission intensities to auroral energetic parameters was discussed in §D, and is described in detail in [Grubbs et al., 2018a, 2018b]. The GLOW electron transport model is used to produce a library of altitude profiles of volume emission rates for a set of auroral electron distributions spanning a wide range of $\langle E \rangle$ and Q. These profiles are then height-integrated to produce surface brightness, and ratios of the brightness. The resulting look-up table is used to convert the measured intensity and ratios from the mapped images to estimates of $\langle E \rangle$ and Q for each pixel (Fig. D-7).

Map Resolution. We anticipate two main uses of the imagery from the GBOs. The first is to compare the location of boundaries of the intensity of auroral emissions with features in the in-situ data. With ARCS the improved resolution and ability to sample the same boundary up to 4 times, especially in dynamic conditions, will further inform us of the relationship of the auroral forcing and ionospheric response. Clearly for these studies the best resolution possible is desired. At 0.5 km per pixel or less at 110 km altitude we will create intensity maps of all imagers at 0.25 to 0.5 km resolution in the region within 40° of zenith. The second use of imagery is the inversion to auroral energetics ($\langle E \rangle$ and Q). These are primarily to be used as input to the data assimilation models described extensively in §D. The resolution of these models is on the order of 1 km, so the inversion al-

gorithms will produce energetics maps with 1 km grid size.

Map Uncertainties. Uncertainties in the GBO maps to be produced for ARCS fall into two broad categories of intensity and geometric uncertainties. The intensity uncertainties are further broken down into two types – random and calibration. The impacts of random uncertainty occur when auroral intensities are low and result in a “mottled” reproduction of the arc parameters (Fig. D-23). For these low energy flux events, the arcs are typically less dynamic, and co-adding of images can be used to reduce the random noise. Calibration uncertainties may cause shifts in the estimates of auroral energetic parameters ($\langle E \rangle$ and Q). Regular star calibrations of the imagers confirm the calibration and alert us to issue of changes in detector performance. We will monitor the overall sensitivity of each camera by observing a bright star every night and look for changes in measured intensity. This calibration product is stored along with the data.

At magnetic zenith all emissions imaged from an auroral arc are concentrated within the width of the arc. Observations at angles oblique to magnetic zenith produce geometric uncertainties. At oblique angles the altitude profile of the aurora emissions is spread out when an image is mapped, and the apparent width of the arc is typically greater than the true width. This has two consequences. In terms of mapping the auroral intensities the position of an arc boundary is shifted. The intensity of the oblique view is also spread out over a wider area and so the conversion to $\langle E \rangle$ and Q is affected by the change in apparent intensities. The magnitude of the uncertainty is a complicated function of the obliquity angle and the arc geometry, but the magnitude is reasonably approximated by a cosine function of the oblique angle (Fig. D-23). This is one key reason we have maintained close GBO site spacing to reduce the impact of the oblique geometry uncertainties.

A third uncertainty is also introduced when a station is non-operational or is clouded out. The choice of a dense array of GBOs is in part driven by the desire to provide some redundancy in the precipitating electron characterization. If a station is not available, we can make use of the designed field of view of the cameras, which is much wider than 40° from zenith, to observe

auroral forms over adjacent sites. This is shown in Figure E-22, which is a mosaic made from four cameras operating in NE Alaska in March of 2014. Three cameras denoted by the blue circles show the full 160° FOV (wider than the proposed ARCS FOV), while the camera at Venetie (red circle) is limited to 40° from zenith. The figure shows how individually mapped images, or auroral energetic parameters like those shown in Figure D-7, are stitched together. It also illustrates that even if one site (e.g., Venetie) was not operating, the arc position over Venetie would still be inferable, though with less certainty, from neighboring cameras, or by interpolating between the adjacent cameras.

E.3.5 Instrument Control Electronics (ICE)

E.3.5.1 ICE Requirements

The ICE is the central instrument data processor for ARCS (FO1-E). The ICE consists of a digital controller board for handling all command and data processing, a low voltage power supply (LVPS) board for regulated secondary power distribution, a high voltage power supply (HVPS) board for generating the STA MCP

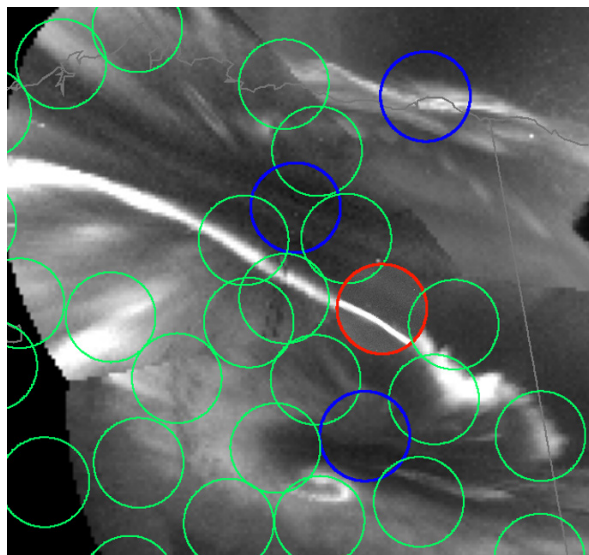


Figure E-22. Map of auroral activity from four sites, three in blue that make up the bulk of the map, and one, Venetie, AK, in red with the resolution expected for ARCS. The remaining circles, in green are a subset of the proposed ARCS GBO sites. The figure illustrates the advantage of dense array of multiple high-resolution imagers, but also shows the graceful degradation by collecting a wide-field image at all the sites.

Table E-10: ICE Accommodations	
Key Characteristics	
HV Output	-2.2 kV
LV Outputs	3.3V, 5V, 8V
Mass	1.8 kg
Power	5.1W
Volume	9 x 13 x 5 cm
Operating Temperature	-20 to +40° C
Survival Temperature	-30 to +50° C

bias voltages, and an interconnecting backplane (Table E-10). The controller board is full size while the LVPS and HV boards are half size cards (FO1-E).

E.3.5.2 ICE Instrument Design

ICE Electronics & Data Processing. The ICE box LVPS receives unregulated 12V and generates the +8V, +5V and +3.3V used by the science instruments and contains linear regulators for the lower voltages used internally. Independent switches for MAG, eTOMS and STA are incorporated with voltage and current limiting.

The ICE Controller contains the science FSW, and interfaces with the Avionics C&DH to receive commands and timing information used for instrument control and data processing. Data is compressed, formatted into time tagged CCSDS packets distinguished by APID, and transferred to the C&DH for storage in the 4GB Avionics memory awaiting transmission to the ground. The ICE receives a time message consisting of the time at the tone and a PPS indicating the second boundary from the C&DH. The ICE then distributes the PPS to the MAG and eTOMS to allow synchronization and data time stamping (STA time stamping occurs in the ICE). As shown in FO1-E, the heritage designed controller board contains an FPGA with a processor core and interface logic, non-volatile MRAM for boot and FSW, and 256MB of SDRAM memory for temporary buffering of data. The soft processor core is a fault-tolerant LEON3FT, a 32-bit microprocessor core based on the SPARC-V8 architecture.

The controller powers the instrument switches by sending a command to the LVPS. STA and eTOMS are powered on only for each science pass while MAG is powered continuously. The STA power switch controls power to the STA analog electronics on the controller, the STA

preamps in the sensor heads, and the HVPS. The ICE controls the HV output to the STA MCP with a dual protected command sequence to ensure HV does not inadvertently come on. The HV is enabled by the controller DAC and a reference voltage is then sent to give a slow ramp up to the MCP HV allowing a limited turn-on for ambient verification purposes.

On-orbit the MCP HV is disabled and the STA power switch is turned off at the end of science mode. The ICE controls the STA sweep synchronizing the start to the PPS and provides a DAC output to the analog section for routing to the sensor heads. STA preamp outputs received from the sensors are accumulated and binned by energy and position. The STA gate is controlled by comparing incoming particle count rates to a programmable threshold (§E.3.1).

ICE Flight Software. Four FSW builds are planned: 1) interface development (Phase B); 2) EM version (PDR to CDR); 3) FM version (CDR to SIR); and 4) Pre-launch and commissioning (SIR through end-to-end testing and commissioning). A test bed consisting of the EM ICE, EM instruments, and an avionics simulator is maintained at the UNH SOC for verification of new command sequences and uploads, FSW support, and anomaly investigation as needed.

ICE Heritage and TRL. The ICE box consists of a digital Controller board, a LVDS board, a HVPS board, and an interconnecting backplane; this is a low-risk development for the ARCS program due to the space flight heritage of the ICE design at the component and board level. The design and manufacturing processes to be utilized at SwRI for the ICE box also has extensive space flight hardware heritage and is at TRL 6.

The digital Controller board and FPGA design are based upon the similar flight MMS Central Data Processing Unit (CDPU), with the addition of the STA analog and FPGA control logic, which is derived from the STEREO/PLASTIC flight design. The LVPS design is based upon the DC-DC converter from the flight Firebird I and II cubesat designs. The design heritage for HVPS designs includes MMS, STEREO, and IBEX; the HVPS design for the STA is based upon the MMS/EDI HVPS.

E.3.5.3 ICE S/C Accommodations

The ICE is shown in FO2-B. There are no spe-

cial requirements on viewing or location on the satellite due to compact nature of the ARCS satellite. The ICE design must allow for all electrical connection and interface with STA, MAG, eTOMS and the S/C while minimizing overall footprint and mass.

E.4 Data Sufficiency

Data Quality: The quality and quantity of data has been carefully assessed and quantitatively studied using ARCS Observing System Simulation Experiments (OSSEs). The ARCS OSSEs demonstrate the sufficiency of the ARCS measurement to achieve science closure (§D).

The data quality for each instrument meets their respective L1 science requirements (Table E-1). This is demonstrated in our discussion of instrument calibration, expected instrument performance and error analysis associated with the science data products produced using the instrument data (§E.3.1-4). §D.4-7 demonstrate how these science data products provide science closure of the ARCS SOs.

Data Quantity: The ARCS SOs will be met through validated case study analyses of Scen2 and Scen3 observations backed by the statistically plentiful Scen1 data quantities, as detailed in §D.4. The 3x/day ARCS science passes over the 2-year mission result in over 2000 science passes. §D.2.2 and §D.4-7, demonstrate how the different science passes and the 3 types of observing scenarios build upon one another to meet all ARCS SOs. Together, the ARCS mission provides an unprecedented view of the pre-magnetic-midnight sector aurora. As an example, we show 48 of 96 days of clear-sky auroral viewing in Alaska at 10 UT during a similar phase in the solar cycle (Fig. E-23). The 96 days indicate about 40% of the nights have clear or mostly clear skies, in agreement with the arctic-based cloud occurrence studies by Shupe et al., [2006]. All these data will be used to produce the data maps that meet the L1 science requirements, that combined with detailed case studies, analysis using the ARCS modeling framework (§D.6.4) and ML approaches (§D.6.5 and App. L.14.2.4), provide closure of the ARCS SOs.

High End Computing (HEC) Requirements: Case study model simulations conducted with GEMINI and GITM will be very high resolution and require meshes of up to hundreds of millions of grid points. These will be conducted

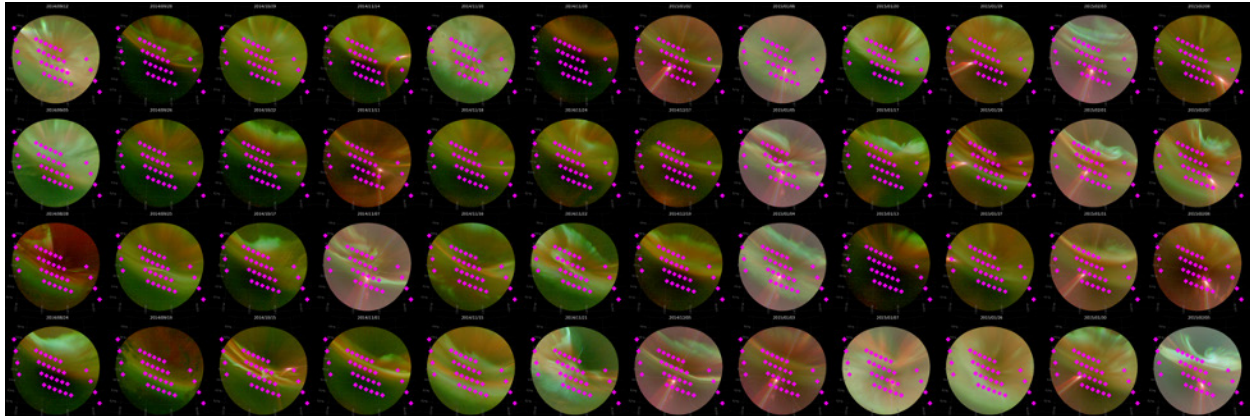


Figure E-23. 48 of at least 96 different days at Poker Flat, Alaska with auroral cloud free all sky images at 10 UT during the 2014-15 Winter Season. The ARCS array is shown in pink. Clear and mostly clear skies occur approximately 40% of the time over Alaska [Shupe et al., 2006].

for a large number of Scen3 crossings (~50-75), and thus will require use of NASA's HEC system. We anticipate a total of about 90 million core hours (65M GEMINI, 25M GITM) and about 20 TB of storage will be required over the course of the mission (simulation data will periodically be transferred to storage at ERAU and, eventually, the SOC). The total number of SBUs required is ~3.3 million SBUs, needed almost exclusively during Phases E-F.

E.5 Data Plans

E.5.1 ARCS Data Management

The ARCS Data Management Plan (App L.5) will follow and adhere to the NASA Plan for Increasing Access to the Results of Scientific Research (2015) and the NASA Heliophysics Science Data Management Policy (2016). The raw data will be pipeline-processed to create data products in physical units designed for scientific analysis. The ARCS team is committed to fast, easy data access. The team will facilitate community access by developing an interactive webpage modeled after the Swarm-Aurora page developed by the University of Calgary group that allows users to explore the full variety of ARCS data products, as well as supporting documentation, ancillary data, and algorithm descriptions. In addition to the validated data, the web interface will also provide quick-look images of CubeSwarm and GBO data for early event identification. The data will be archived at the NASA Space Physics Data Facility (SPDF) using Common Data Format (CDF) files for the CubeSwarm data and FITS files for GBO data.

The definition of the data levels are shown in Table E-11. Over the 2-year mission, there are 3.05 TB of satellite Level 0 data and 660 TB of GBO Level 1 data (raw data for GBO is Level 1 data). Table E-13 lists the data products and the schedule for data processing and delivery.

E.5.2 ARCS Data Processing Flow

The data processing is led by the ARCS SOC located at UNH, which incorporates data from the GBO Science Operations Center (GBOC) located at UAF/GI (§F.2.7.9). A simplified data flow diagram is shown in Figure E-24. For Level 1 through Level 3 data processing, there are two parallel processing chains. The SOC processes all data from the CubeSwarm while the GBOC processes all data from the GBOs. The Level 3 Q and <E> maps are then transferred from the GBOC to the SOC. ERAU retrieves Level 3 data from the SOC (both CubeSwarm data and GBO data) and uses them as data inputs to their model to generates survey model output (“Data Cubes”) of ionospheric plasma, electron, and neutral parameter at 5 s cadence for each pass.

Table E-11: Definition of Data Levels

Data Level	Data Level Definition
Level 0	Raw telemetry stream, but time ordered.
Level 1	Time ordered, decompressed and quality checked with duplicate data removed and GBO Raw Data
Level 2	Calibrated data from individual S/C converted into physical units and Calibrated GBO Data
Level 3	L1 Science Requirement maps (Table E-1), ARCS modeling and ML results.
Level 4	Products such as Peer Reviewed Publications

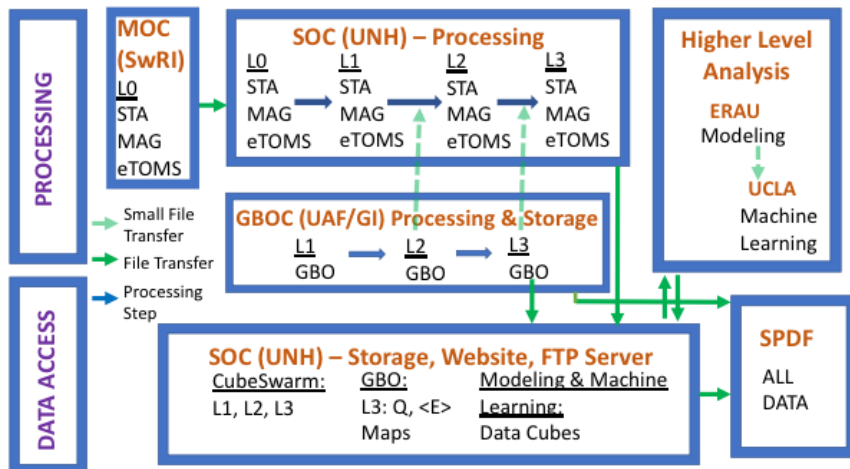


Figure E-24. Data processing pipeline.

The modeling results are returned to the SOC where they can be displayed and accessed along with the data. Similarly, UCLA takes the modeling results along with the CubeSwarm and GBO Level 3 data, and uses these to produce reconstructed maps of flows, field aligned currents, and convection electric fields using Machine Learning techniques. These maps are also transferred to the SOC for display and access. All data are then archived at the NASA archive.

Individual instrument teams are responsible for both ground and inflight calibration, as described in the individual instrument sections, and for delivering updated calibrations to the SOC for use in processing. The instrument and

science teams are responsible for providing algorithms to the SOC for the production of Level 2 and Level 3 data products, and for validating the products (Table E-12).

The GBO creates large volumes of data at remote locations. Most GBO sites have insufficient network bandwidth to send full resolution video-mode data back to the GBOC. Each GBO is equipped with sufficient storage to support a full sea-

son's data. Local personnel send the full-resolution data every two weeks. Sub-sampled, low resolution image data are available in near real-time from each station, and are forwarded from the GBOC to the SOC. In addition, quick-look products using low-resolution data from all stations are calculated and forwarded to the SOC. The Level 3 geo-located energy flux and average energy maps are sent to the SOC for use in the event analysis and modeling. Calibrated images may also be sent to the SOC for special cases, but the bulk of the raw and calibrated images remain at the GBOC where they are made available for download.

Table E-12: ARCS data product summary and delivery schedule

Data Product (Responsible Person)	Level	Data Validated	Data Posted	Location
CubeSwarm: Instrument and Spacecraft Raw Data (MOC, Redfern)	0	N/A	N/A	MOC
GBO: Raw Imagery and Housekeeping (GBOC, Hampton)	0	N/A	N/A	N/A
CubeSwarm: Time-Ordered Calibrated Data (SOC, Ellis)	1	1 Day	1 week	SOC
GBO: Raw Imagery and Housekeeping (GBOC, Hampton)	1	6 Weeks	4 weeks	GBOC
Ancillary Data: Attitude, Empheris, Calibration Tables (SOC, Ellis)	1	1 Day	1 week	SOC
STA: Calibrated plasma flow velocity vector time series and maps (Kistler)	2	2 Months	2 Months	SOC
MAG: Magnetic Field Perturbations in Geomagnetic Coordinates (Vines)	2	2 Months	2 Months	SOC
eTOMS: Scintillation and TEC data converted to ionospheric pierce point (Nikoukar)	2	2 Months	2 Months	SOC
GBO: Multi-spectral Auroral Imagery (Hampton)	2	2 Months	2 Months	GBOC
STA: Maps of plasma flow fields (Lynch)	3	4 Months	4 Months	SOC
MAG: Maps of field-aligned currents (Anderson)	3	4 Months	4 Months	SOC
eTOMS: Tomographic reconstructions of Ionospheric Electron Density (Nikoukar)	3	4 Months	4 Months	SOC
GBO: Multi-Site Mosaic Images of Aurora (Hampton)	3	4 Months	4 Months	GBOC
GBO: Maps of characteristic energy and total energy flux (Hampton)	3	4 Months	4 Months	SOC
Machine learning data assimilation products (Bortnik)	3	6 Months	6 Months	SOC
Model Based Science Data Product: FRAMBOISE Model Outputs (Zettergren)	3	6 Months	6 Months	SOC
Peer Reviewed Papers, Report (all)	4	N/A	As Produced	N/A

Notice: Use or disclosure of the proprietary and competition sensitive material on this page is subject to the proposal title page restriction.

E.5.3 Resources

The ARCS SOC lead has a 50% LOE during Phase B and C, and then increases to full time 18 months before launch to finalize pipeline processing. A full-time website developer starts one year before launch. Each of the instrument teams has ~50% LOE in B-D supporting algorithm development and processing software. After launch, a full-time data-tech manages the pipeline process. The website developer continues for 1 year. The SOC lead supports the pipeline processing at 50% LOE, and transitions down to 25% LOE over a year. Each of the instrument teams has 50% LOE support for data validation, software updates and calibration updates. In addition to the co-I support, each major institution also has a post-doc to support preliminary analysis of data and publication of results. A large server, capable of handling 3 PBytes of data is included in the SOC costs (\$120k).

For the GBOC, a project manager has 25% time during Phases C and D to ensure compliance with requirements. A systems programmer is funded at 50% for late Phase C and all of Phase D to produce the data ingestion system, and prepare the telemetry monitoring system with the GBOs. Storage for the full 3 PBytes of anticipated GBO raw and processed data is handled by a server, and tape storage hardware, and processing is handled by three dedicated multi-processor Penguin computer nodes for the Chinook HPC at the GI's Research Computing System group, and are all included in the GBOC costs (\$500k, including maintenance and storage fees for the entire mission). Processing algorithms for the L1 to L3 processing is handled by two dedicated full-time students and one post-doc at UAF.

E.6 Science Team

The ARCS science team (Table E-13) includes leading experts in auroral physics, space instrumentation, instrument calibration, data analysis, machine learning, data assimilation and modeling. All team members have specific roles and responsibilities, and share a joint responsibility of excellence, teamwork and collaboration. The team includes a mix of early, mid and late career experts.

The ARCS collaborators from the U of Calgary are funded by the Canadian Space Agency

and from UAF/GI (M. Conde) by NASA and NSF grants.

The ARCS science team, instrument leads and their team will support the design, build, calibration and develop algorithms used to produce data products. After launch, the teams will perform instrument characterization; produce the data products; and analyze data. The modeling team use a suite of models to assimilate these data into an auroral system wide perspective.

E.7 Plan for Science Enhancement Options

The SEO stand-alone justification and cost plans are provided in §K.

E.7.1 SEO-1 Aurorasaurus

Aurorasaurus [MacDonald et al., 2015] is a citizen science initiative that tracks auroras around the world via reports on the Aurorasaurus website, mobile apps, and social media [Case et al., 2016]. ARCS's auroral images and multipoint measurements will captivate the public over the next solar maximum, joining exquisite amateur images of the same events to comprise a path-finder science enhancement opportunity (SEO) as one of the first flight missions to include citizen science by design. The ARCS science missions and auroral observations occur at the same time, every day, over the same location in Alaska. The two other daily ARCS science pass locations will be publicized in advance, providing opportunities for citizen scientists participation. The ARCS science passes extend down to 45° geographic latitude. Although outside of the GBO network, it will provide opportunities for a larger part of the public to engage in Aurorasaurus and ARCS.

E.7.2 SEO-2 Guest Investigator Program

The ARCS data set provides a new view of the distributed system science of the ionosphere. It is exciting to consider the many different science questions that are addressable with both the primary data base, and other potential studies accessible from the existing mission design. These include data collected over equatorial latitudes or southern hemisphere auroral zone crossings, data captures over Scandinavian assets such as MIRACLE and Eiscat3D, day-side auroral zone studies, and technology studies of S/C charging on CubeSats with propulsion. Following the lead of the MMS mission,

we propose a Guest Investigator SEO focused on early-career scientists. We will look for new directions and new uses of the ARCS platform, including both (a) novel uses and analyses of the primary ARCS database, and (b) data collections in addition to our nominal “three nightside northern auroral crossings per day”, that make

use of the rich ARCS mission but do not require rearrangement of the nominal ARCS S/C array. These may, however, entail data collections in addition to our nominal Scenario1/2/3 collections as viable within our existing resources. Four 3-year GI studies will be chosen, to overlap with Phase E/F.

Table E-13: ARCS Science Team Roles

Science Leadership	Years from Ph.D	Roles and Responsibility	LOE (%) B-D/ E/ F
Kristina Lynch, Dartmouth	29	PI; Mission leader, science plasma flow maps	50/85/67
Marilia Samara, GSFC	16	Deputy PI; GBO auroral data products and science	50/64/20
Robert Erlandson, APL	35	Project Scientist; Level 1-2 Req, MAG Science	60/50/50
Co-Investigators	Roles and Responsibility		
Brian Anderson, APL	34	MAG Lead, Field aligned current map product	40/75/50
Sarah Vines, APL	5	MAG Instrument calibration and data analysis	40/75/50
*Rumi Nakamura, IWF	31	MAG Science-Auroral Electrodynamics, data analysis	5/30/20
*Werner Magnes, IWF	22	MAG Instrument calibration and science	30/10/5
Lynn Kistler, UNH	34	STA Lead, Instrument calibration and data analysis	44/50/37
Chris Mouikis, UNH	28	STA Data Analysis, SOC Science lead	44/50/50
Roy Torbert, UNH	42	STA Science, Science Advisor	1/6/0
Romina Nikoukar, APL	11	eTOMS Lead, 3D Electron density data product	40/75/50
Jim LaBelle, Dartmouth	36	Student Collaboration Lead, eTOMS Science	5/16/20
Don Hampton, UA/GI	25	GBO Lead, imagery calibration, mosaic data product	30/55/33
Robert Michell, GSFC	14	GBO imaging inversion and auroral morphology	18/32/10
Matt Zettergren, ERAU	12	Modeling Lead: FrAMBOISE – Geospace System Models	50/50/50
Shasha Zou, UMich	12	Global Ionosphere-Thermosphere Model	13/34/25
Meghan Burleigh, NRC	3	GEMINI: Geospace Env Model of Ion-Neutral Interactions	50/50/50
Kshitija Deshpande, ERAU	7	Modeling: SIGMA Model and scintillation analysis	21/21/21
John Lyon, Dartmouth	49	Modelling: LFM Model, Modeling Advisor	0/2/0
Jacob Bortnik, UCLA	17	Machine Learning & Data Assimilation Advisor	8/8/8
*David Knudsen, Calgary	31	Combined data analysis, auroral theory	10/20/20
Liz MacDonald, GSFC**	17	SEO-1 Aurorasaurus Lead (if Selected)	2/23/17
Collaborators	Roles and Responsibility		
*Johnathan Burchill, Calgary	18	STA Science, Data analysis	10/25/25
*Mark Conde, UAF/GI	30	Ground-based neutral wind observations	-/-/-
*Meg Gillies, Calgary	9	Ground-based auroral imaging analysis	5/20/5
*Eric Donovan, Calgary	28	Ground-based auroral imaging observations	5/20/5

*Non NASA Funded Co-I or Collaborator, **SEO-1 Lead (not a Co-I)

L.27 List of References

L.27.1 Referenced Standards

- ANSI/AIAA S-120A-2015(2019), Mass Properties Control for Space Systems. https://www.aiaa.org/docs/default-source/uploadedfiles/publications/standards/s-120a-sec-public-review-and-co-ballot-draft.pdf?sfvrsn=ac4256aa_0
- ANSI/EIA-649, National Consensus Standard for CM, March 2015. <https://www.dsp.dla.mil/Portals/26/Documents/Publications/Journal/150301-DSPJ-02.pdf>
- CANISTERIZED SATELLITE DISPENSER (CSD) DATA SHEET. Planetary Systems Corp. (2017, August 4). <http://www.planetarysystemscorp.com/web/wp-content/uploads/2017/10/2002337E-CSD-Data-Sheet.pdf>.
- EEE-INST-002 (2003), https://nepp.nasa.gov/docuploads/FFB52B88-36AE-4378-A05B-2C084B5EE2CC/EEE-INST-002_add1.pdf
- EHPD-RQMT-0001, Explorers & Heliophysics Projects Division (EHPD) Mission Assurance Requirements (MAR) Mission Risk Class - NPR7120.5 Class C, 2017. https://explorers.larc.nasa.gov/2019APSMEX/MO/pdf_files/EHPD-RQMT-0001-091416Released-1.pdf
- FAR 19.7, The Small Business Subcontracting Program, March 10, 2021. <https://www.acquisition.gov/far/subpart-19.7>.
- FAR 52.219-9, Small Business Subcontracting Plan, June 2020. <https://www.acquisition.gov/far/52.219-9>.
- FIPS 140-2, Security Requirements for Cryptographic Modules, May 25, 2001. <https://csrc.nist.gov/publications/detail/fips/140/2/final>.
- GSFC-STD-7000A, General Environmental Verification Standards for GSFC Flight Programs and Projects, (2013). <https://standards.nasa.gov/standard/gsfc/gsfc-std-7000>
- IPC standards for class-3/A printed wiring board assemblies. <https://www.ipc.org/ipc-standards>
- International Reference Ionosphere (2021), <http://irimodel.org/>.
- International Telecommunication Union, Recommendation ITU-R P.531-11 (2012) Ionospheric propagation data and prediction methods required for the design of satellite services and systems
- IRI, (2021) <https://ccmc.gsfc.nasa.gov/modelweb/ionos/iri.html>, accessed May, 2021.
- Mil-STD-461. http://everyspec.com/MIL-STD/MIL-STD-0300-0499/MIL-STD-461_8678/
- NASA CARA (2020), “Best Practices”, https://nодis3.gsfc.nasa.gov/OCE_docs/OCE_50.pdf; page 15. accessed 2021.
- NASA EEE-INST-002, (April 2008). <https://nepp.nasa.gov/index.cfm/12821>.
- NASA Strategic Plan 2018. (2018, February 12). https://www.nasa.gov/sites/default/files/atoms/files/nasa_2018_strategic_plan.pdf.
- NASA. (2018) Science Mission Directorate Policy Citizen Science SMD Policy Document SPD-33 Recommended by SMD Science Management Council Approved by SMD Associate Administrator Responsible SMD Official: Direction, Science Engagement and Partnerships[Online]. Available at: <https://science.nasa.gov/citizenscientists>
- NASA-STD-1006 Space Systems Protection, October 29, 2019. <https://standards.nasa.gov/standard/nasa/nasa-std-1006-wchange-1>.
- NASA-STD-6016 Technical Standards System (May 14, 2020). <https://standards.nasa.gov/standards/nasa/nasa-std-6016>

dard/nasa/nasa-std-6016.

NASA-STD-8719.24 Technical Standards System (August 26, 2011). <https://standards.nasa.gov/standard/nasa/nasa-std-871924>

NASA 8739 Workmanship Standards. <https://nepp.nasa.gov/index.cfm/5511>

NASA. (2016, June 30). GSFC-STD-1000. Rules for the Design, Development, Verification, and Operation of Flight Systems. <https://standards.nasa.gov/standard/gsfc/gsfc-std-1000>.

NID 1058.127, NASA Enterprise Protection Program, May 7, 2020. https://nodis3.gsfc.nasa.gov/OPD_docs/NID_1058_127.pdf

NPD 8700.1E, NASA Policy for Safety and Mission Success, (December 6, 2013). https://nodis3.gsfc.nasa.gov/displayDir.cfm?Internal_ID=N_PD_8700_001E_&page_name=main

NPR 1058.1 section 2.3, Officials-in-Charge of Headquarters Offices, Mission Directorate Associate Administrators, Center Directors, Program Directors, Program Managers, and Project Managers, June 14, 2019.

NPR 2810.1, Security of Information Technology, (May 19, 2011). https://nodis3.gsfc.nasa.gov/displayDir.cfm?Internal_ID=N_PR_2810_001A_&page_name=main

NPR 7120.5, NASA Space Flight Program and Project Management Requirements, (August 14, 2012). <https://nodis3.gsfc.nasa.gov/displayDir.cfm?t=NPR&c=7120&s=5E>

NPR 7123.1C, NASA Systems Engineering Processes and Requirements, (February, 14, 2020). <https://nodis3.gsfc.nasa.gov/displayDir.cfm?t=NPR&c=7123&s=1B>

NPR 7150.2C, NASA Software Engineering Requirements, (2019). <https://nodis3.gsfc.nasa.gov/displayDir.cfm?t=NPR&c=7150&s=2B>

NPR 8705.4, Risk Classification for NASA Payloads, (June 14, 2004). https://nodis3.gsfc.nasa.gov/displayDir.cfm?Internal_ID=N_PR_8705_004A_&page_name=main

NPR 8705.5A, Technical Probabilistic Risk Assessment (PRA) Procedures for Safety and Mission Success for NASA Programs and Projects, (June 7, 2010). Technical Probabilistic Risk Assessment (PRA) Procedures for Safety and Mission Success for NASA Programs and Projects

NPR 8715.7, Payload Safety Program, (April 27, 2020). https://nodis3.gsfc.nasa.gov/displayDir.cfm?Internal_ID=N_PR_8715_007B_&page_name=main

NRC, (2013), National Research Council (2013), Solar and Space Physics: A Science for a Technological Society. Washington, DC: The National Academies Press. <https://doi.org/10.17226/13060>.

Science Mission Directorate Policy Citizen Science SMD Policy Document SPD-33 Recommended by SMD Science Management Council Approved by SMD Associate Administrator Responsible SMD Official: Director, Science Engagement and Partnerships. (2018). Retrieved from <https://science.nasa.gov/citizenscientists>

L.27.2 Documents and Papers

Aakjær, C.D., Olsen, N. and Finlay, C.C., 2016. Determining polar ionospheric electrojet currents from Swarm satellite constellation magnetic data. *Earth, Planets and Space*, 68(1), p.140. doi: 10.1186/s40623-016-0509-y.

AIM-1, in National Research Council (2013), Solar and Space Physics: A Science for a Technological Society. Washington, DC: The National Academies Press. <https://doi.org/10.17226/13060>.

Alken, P., Thébault, E., Beggan, C.D. et al. International Geomagnetic Reference Field: the thirteenth generation. *Earth Planets Space* 73, 49 (2021). <https://doi.org/10.1186/s40623-020-0118-1>

01288-x

- Amm, O., 2001. The elementary current method for calculating ionospheric current systems from multisatellite and ground magnetometer data. *Journal of Geophysical Research: Space Physics*, 106(A11), pp.24843-24855. doi: 10.1029/2001JA900021.
- Amm, O., et al., *Ann. Geophys.*, 29, 701–716, 2011.
- Amm, O., Pajunpää, A., and Brandström, U., 1999, Spatial distribution of conductances and currents associated with a north-south auroral form during a multiple-substorm period, *Ann. Geophys.*, 17, 1385–1396, <https://doi.org/10.1007/s00585-999-1385-6>.
- Anderson, B. J., R. Angappan, A. Barik, S. K. Vines, S. Stanley, P. N. Bernasconi, H. Korth, and R. J. Barnes (2020), Satellite Constellation Data for Study of Earth's Magnetic Field, in press, *Geochemistry, Geophysics, Geosystems (G3)*, 8 June 2021.
- Anderson, B.J., Acuña, M.H., Lohr, D.A., Scheifele, J., Raval, A., Korth, H. and Slavin, J.A., 2007. The Magnetometer instrument on MESSENGER. In *The MESSENGER mission to Mercury* (pp. 417-450). Springer, New York, NY. doi: 10.1007/978-0-387-77214-1_12.
- Anderson, B.J., Gary, J.B., Potemra, T.A., Frahm, R.A., Sharber, J.R. and Winningham, J.D., 1998. UARS observations of Birkeland currents and Joule heating rates for the November 4, 1993, storm. *Journal of Geophysical Research: Space Physics*, 103(A11), pp.26323-26335. doi: 10.1029/98JA01236.
- Anderson, B.J., Korth, H., Waters, C.L., Green, D.L., Merkin, V.G., Barnes, R.J. and Dyrud, L.P., 2014. Development of large-scale Birkeland currents determined from the Active Magnetosphere and Planetary Electrodynamics Response Experiment. *Geophysical Research Letters*, 41(9), pp.3017-3025. doi: 10.1002/2014GL059941.
- Anderson, B.J., Potemra, T.A., Bythrow, P.F., Zanetti, L.J., Holland, D.B. and Winningham, J.D., 1993. Auroral currents during the magnetic storm of November 8 and 9, 1991: Observations from the Upper Atmosphere Research Satellite particle environment monitor. *Geophysical research letters*, 20(12), pp.1327-1330. doi: 10.1029/93GL01106.
- Anderson, B.J., Takahashi, K. and Toth, B.A., 2000. Sensing global Birkeland currents with Iridium® engineering magnetometer data. *Geophysical Research Letters*, 27(24), pp.4045-4048. doi: 10.1029/2000GL000094.
- Anderson, B.J., Zanetti, L.J., Lohr, D.H., Hayes, J.R., Acuña, M.H., Russell, C.T. and Mulligan, T., 2001. In-flight calibration of the NEAR magnetometer. *IEEE transactions on geoscience and remote sensing*, 39(5), pp.907-917. doi: 10.1109/36.921408.
- Anderson, C., Davies, T., Conde, M., Dyson, P., & Kosch, M. J. (2011). Spatial sampling of the thermospheric vertical wind field at auroral latitudes. *Journal of Geophysical Research: Space Physics*, 116(A6).
- Angelopoulos et al., 2008, First Results from the THEMIS Mission, *Space Sci Rev*, 141: 453–476 DOI 10.1007/s11214-008-9378-4
- Archer, W. E., Knudsen, D. J., Burchill, J. K., Jackel, B., Donovan, E., Connors, M., and Juusola, L., 2017. Birkeland current boundary flows, *J. Geophys. Res. Space Physics*, 122, 4617– 4627, doi:10.1002/2016JA023789.
- Archer, W. E., Knudsen, D. J., Burchill, J. K., Patrick, M. R. and St.-Maurice, J. P. 2015. Anisotropic core ion temperatures associated with strong zonal flows and upflows. *Geophys. Res. Lett.*, 42: 981– 986. doi: 10.1002/2014GL062695.
- Archer, W., D.J. Knudsen, 2018. Distinguishing subauroral ion drifts from Birkeland current boundary flows: SAID vs BCBF. *Journal of Geophysical Research: Space Physics* 123. doi: 10.1002/2017JA024577.

- Archer, W.E., Gallardo-Lacourt, B., Perry, G., St.-Maurice, J.P., Buchert, S.C. and Donovan, E., 2019. Steve: The Optical Signature of Intense Subauroral Ion Drifts. *Geophysical Research Letters*. doi: 10.1029/2019GL082687.
- Auroral Imaging Group, University of Calgary., (2019) swarm-aurora.com[Online]. Available at: <https://swarm-aurora.com>.
- Austen, J.R., Franke, S.J. and Liu, C.H., 1988. Ionospheric imaging using computerized tomography. *Radio Science*, 23(3), pp.299-307. doi: 10.1029/RS023i003p00299.
- Averkin, S. N. and N. A.Gatsonis, A parallel electrostatic Particle-in-Cell method on unstructured tetrahedral grids for large-scale bounded collisionless plasma simulations, *Journal of Computational Physics*, Volume 363, 15 June 2018, Pages 178-199, <https://doi.org/10.1016/j.jcp.2018.02.011>
- Baker, D.N., Riesberg, L., Pankratz, C.K., Panneton, R.S., Giles, B.L., Wilder, F.D. and Ergun, R.E., 2016. Magnetospheric multiscale instrument suite operations and data system. *Space Science Reviews*, 199(1-4), pp.545-575. doi: 10.1007/s11214-014-0128-5.
- Basu, S. K.M. Groves, Su. Basu, P.J. Sultan, Specification and forecasting of scintillations in communication/navigation links: current status and future plans, *Journal of Atmospheric and Solar-Terrestrial Physics*, Volume 64, Issue 16, 2002, Pages 1745-1754, ISSN 1364-6826,[https://doi.org/10.1016/S1364-6826\(02\)00124-4](https://doi.org/10.1016/S1364-6826(02)00124-4).
- Basu, S., MacKenzie, E., and Basu, S. (1988), Ionospheric constraints on VHF/UHF communications links during solar maximum and minimum periods, *Radio Sci.*, 23(3), 363– 378, doi:10.1029/RS023i003p00363.
- Bekkeng, T.A., Helgeby, E.S., Pedersen, A., Trondsen, E., Lindem, T. and Moen, J.I., 2019. Multi-needle Langmuir probe system for electron density measurements and active spacecraft potential control on cubesats. *IEEE Transactions on Aerospace and Electronic Systems*. doi: 10.1109/TAES.2019.2900132.
- Bernhardt, P.A. and Siefring, C.L., 2006. New satellite-based systems for ionospheric tomography and scintillation region imaging. *Radio science*, 41(5). doi: 10.1029/2005RS003360.
- Bernhardt, P.A. and Siefring, C.L., 2010. Low-latitude ionospheric scintillations and total electron content obtained with the CITRIS instrument on STPSat1 using radio transmissions from DORIS ground beacons. *Advances in Space Research*, 45(12), pp.1535-1540. doi: 10.1016/j.asr.2009.12.001.
- Bernhardt, P.A., McCoy, R.P., Dymond, K.F., Picone, J.M., Meier, R.R., Kamalabadi, F., Cotton, D.M., Charkrabarti, S., Cook, T.A., Vickers, J.S. and Stephan, A.W., 1998. Two-dimensional mapping of the plasma density in the upper atmosphere with computerized ionospheric tomography (CIT). *Physics of Plasmas*, 5(5), pp.2010-2021. doi: 10.1063/1.872872.
- Bernhardt, P.A., Selcher, C.A., Basu, S., Bust, G. and Reising, S.C., 2000. Atmospheric studies with the Tri-Band Beacon instrument on the COSMIC constellation. *TERRESTRIAL ATMOSPHERIC AND OCEANIC SCIENCES*, 11(1), pp.291-312.
- Bernhardt, P.A., Siefring, C.L., Galysh, I.J. and Koch, D.E., 2008. The Scintillation and Tomography Receiver in Space (CITRIS) Instrument for Ionospheric Research. *NAVAL RESEARCH LAB WASHINGTON DC PLASMA PHYSICS DIV*.
- Bernhardt, P.A., Siefring, C.L., Galysh, I.J., Rodiloso, T.F., Koch, D.E., MacDonald, T.L., Wilkens, M.R. and Landis, G.P., 2006. Ionospheric applications of the scintillation and tomography receiver in space (CITRIS) mission when used with the DORIS radio beacon network. *Journal of Geodesy*, 80(8-11), pp.473-485. doi: 10.1007/s00190-006-0064-6.
- Bland, E. C., Heino, E., Kosch, M. J., and Partamies, N.: SuperDARN Radar-Derived HF Radio Attenuation During the September 2017 Solar Proton Events, *Space Weather*, 16, 1455–1469,

<https://doi.org/10.1029/2018SW001916>, 2018.

- Blewitt, G., 1990. An automatic editing algorithm for GPS data. *Geophysical research letters*, 17(3), pp.199-202. doi: 10.1029/GL017i003p00199.
- Board, S.S. and National Research Council, 2013. *Solar and space physics: A science for a technological society*. National Academies Press. doi: 10.17226/13060.
- Borovsky, J.E., 1998. Aurorae: Still in the dark. *Nature*, 393(6683), p.312. doi: 10.1038/30616.
- Borovsky, J.E., Birn, J., Echim, M.M., Fujita, S., Lysak, R.L., Knudsen, D.J., Marghitu, O., Otto, A., Watanabe, T.H. and Tanaka, T., 2020. Quiescent discrete auroral arcs: A review of magnetospheric generator mechanisms. *Space Science Reviews*, 216(1), pp.1-39.
- Bortnik, J., W. Li, R. M. Thorne, and V. Angelopoulos (2016), A unified approach to inner magnetospheric state prediction, *J. Geophys. Res. Space Phys.*, 120, doi: 10.1002/2015JA021733.
- Bortnik, J., X. Chu, Q. Ma, W. Li, X. Zhang, R. M. Thorne, V. Angelopoulos, R. E. Denton, C. A. Kletzing, G. B. Hospodarsky, H. E. Spence, G. D. Reeves, S. G. Kanekal, and D. N. Baker (2018), Artificial Neural Networks for Determining Magnetospheric Conditions, in *Machine Learning Techniques for Space Weather*, Elsevier Inc., doi: 10.1016/B978-0-12-811788-0.00011-1.
- Brambles, O.J., Lotko, W., Zhang, B., Wiltberger, M., Lyon, J. and Strangeway, R.J., 2011. Magnetosphere sawtooth oscillations induced by ionospheric outflow. *Science*, 332(6034), pp.1183-1186. doi: 10.1126/science.1202869.
- Brekke, A., Hall, C. and Hansen, T.L., 1989, June. Auroral ionospheric conductances during disturbed conditions. In *Annales Geophysicae* (Vol. 7, pp. 269-280).
- Briggs, B.H., 1975. Ionospheric irregularities and radio scintillations. *Contemporary Physics*, 16(5), pp.469-488. doi: 10.1080/00107517508210825.
- Brittnacher, M., Spann, J., Parks, G. and Germany, G., 1997. Auroral observations by the polar ultraviolet imager (UVI). *Advances in Space Research*, 20(4-5), pp.1037-1042. doi: 10.1016/S0273-1177(97)00558-9.
- Bunch, N.L., J. LaBelle, A.T. Weatherwax, J.M. Hughes, Auroral Medium Frequency Burst radio emission associated with the March 23, 2007, THEMIS study substorm, *J. Geophys. Res.*, 113, A00C08, doi:10.1029/2008JA013503, 2008.
- Burch, J.L., 2000. IMAGE mission overview. In *The Image Mission* (pp. 1-14). Springer, Dordrecht. doi: 10.1007/978-94-011-4233-5_1.
- Burch, J.L., Torbert, R.B., Phan, T.D., Chen, L.J., Moore, T.E., Ergun, R.E., Eastwood, J.P., Gershman, D.J., Cassak, P.A., Argall, M.R. and Wang, S., 2016. Electron-scale measurements of magnetic reconnection in space. *Science*, 352(6290), p.aaf2939. doi: 10.1126/science.aaf2939.
- Burke, W. J., Huang, C. Y., Valladares, C. E., Machuzak, J. S., Gentile, L. C., & Sultan, P. J. (2003). Multipoint observations of equatorial plasma bubbles. *Journal of Geophysical Research: Space Physics*, 108(A5).
- Burnett, A., and J. LaBelle, Estimating polar cap density and medium-frequency burst source heights using 2fce-roar radio emissions, *J. Geophys. Res.*, 125, doi:10.1029/2020JA028166, 2020.
- Camporeale, E., X. Chu, O. V. Agapitov, and J. Bortnik (2019), On the generation of probabilistic forecasts from deterministic models, *Space Weather*, doi: 10.1029/2018SW002026.
- Carlson, C.W., Curtis, D.W., Paschmann, G. and Michel, W., 1982. An instrument for rapidly measuring plasma distribution functions with high resolution. *Advances in Space Research*, 2(7), pp.67-70. doi: 10.1016/0273-1177(82)90151-X.

- Carlson, C.W., Pfaff, R.A. and Watzin, J.G., 1998a. The fast auroral snapshot (FAST) mission. *Geophysical research letters*, 25(12), pp.2013-2016. doi: 10.1029/98GL01592.
- Carlson, C.W., McFadden, J.P., Ergun, R.E., Temerin, M., Peria, W., Mozer, F.S., Klumpar, D.M., Shelley, E.G., Peterson, W.K., Moebius, E. and Elphic, R., 1998b. FAST observations in the downward auroral current region: Energetic upgoing electron beams, parallel potential drops, and ion heating. *Geophysical Research Letters*, 25(12), pp.2017-2020. doi: 10.1029/98GL00851.
- Carlson, C.W., McFadden, J.P., Turin, P., Curtis, D.W. and Magoncelli, A., 2001. The electron and ion plasma experiment for FAST. In *The FAST Mission* (pp. 33-66). Springer, Dordrecht. doi: 10.1007/978-94-010-0332-2_2.
- Case, N., MacDonald, E. and Patel, K., 2015a. Aurorasaurus and the St Patrick's Day storm. *Astronomy and Geophysics*, 56(3), pp.3-13. doi: 10.1093/astrogeo/atv089.
- Case, N.A., MacDonald, E.A., Heavner, M., Tapia, A.H. and Lalone, N., 2015b. Mapping auroral activity with Twitter. *Geophysical Research Letters*, 42(10), pp.3668-3676. doi: 10.1002/2015GL063709.
- Case, N.A., Kingman, D. and MacDonald, E.A., 2016a. A real-time hybrid aurora alert system: Combining citizen science reports with an auroral oval model. *Earth and Space Science*, 3(6), pp.257-265. doi: 10.1002/2016EA000167.
- Case, N.A., MacDonald, E.A. and Viereck, R., 2016b. Using citizen science reports to define the equatorial extent of auroral visibility. *Space Weather*, 14(3), pp.198-209. doi: 10.1002/2015SW001320.
- Cavalier, D. and Kennedy, E.B. eds., 2016. *The rightful place of science: Citizen science*. Consortium for Science, Policy & Outcomes.
- Chu, X., et al. (2017a), A neural network model of three-dimensional dynamic electron density in the inner magnetosphere, *J. Geophys. Res. Space Physics*, 122, 9183–9197, doi: 10.1002/2017JA024464.
- Chu, X. N., J. Bortnik, W. Li, Q. Ma, V. Angelopoulos, and R. M. Thorne (2017b), Erosion and refilling of the plasmasphere during a geomagnetic storm modeled by a neural network, *Journal of Geophysical Research: Space Physics*, Volume 122, issue 7, pp. 7118-7129, doi: 10.1002/2017JA023948.
- Clayton, R., Burleigh, M., Lynch, K.A., Zettergren, M., Conde, M., Evans, T., Grubbs, G., Hampton, D.L., Hysell, D., Lessard, M., Michell, R., Reimer, A., Roberts, T.M., Samara, M., Varney, R., 2021. 3D modeling results of the GEMINI models using reconstructed 2D maps of auroral data. In preparation for submission to *Journal of Geophysical Research: Space Physics*.
- Clayton, R., Lynch, K. A., Evans, T., Hampton, D. L., Burleigh, M., Zettergren, M. D., et al. (2017). ISINGLASS Auroral Sounding Rocket Campaign Data Synthesis: Radar, Imagery, and In Situ Observations. In AGU Fall Meeting Abstracts (Vol. 2017, pp. SM41A-2664).
- Clayton, R., Lynch, K., Zettergren, M., Burleigh, M., Conde, M., Grubbs, G., Hampton, D., Hysell, D., Lessard, M., Michell, R. and Reimer, A., 2019. Two-Dimensional Maps of In Situ Iono-spheric Plasma Flow Data Near Auroral Arcs Using Auroral Imagery. *Journal of Geophysical Research: Space Physics*, 124(4), pp.3036-3056. doi: 10.1029/2018JA026440.
- Codrescu, M.V., Fuller-Rowell, T.J. and Foster, J.C., 1995. On the importance of E-field variability for Joule heating in the high-latitude thermosphere. *Geophysical Research Letters*, 22(17), pp.2393-2396. doi: 10.1029/95GL01909.
- Codrescu, M.V., Fuller-Rowell, T.J., Foster, J.C., Holt, J.M. and Cariglia, S.J., 2000. Electric field variability associated with the Millstone Hill electric field model. *Journal of Geophysical Research: Space Physics*, 105(A3), pp.5265-5273. doi: 10.1029/1999JA900463.

- Cohen, I.J., Lessard, M.R., Kaepller, S.R., Bounds, S.R., Kletzing, C.A., Streltsov, A.V., LaBelle, J.W., Dombrowski, M.P., Jones, S.L., Pfaff, R.F. and Rowland, D.E., 2013. Auroral Current and Electrodynamics Structure (ACES) observations of ionospheric feedback in the Alfvén resonator and model responses. *Journal of Geophysical Research: Space Physics*, 118(6), pp.3288-3296. doi: 10.1002/jgra.50348.
- Conde, M.G., Bristow, W.A., Hampton, D.L. and Elliott, J., 2018. Multiinstrument Studies of Thermospheric Weather Above Alaska. *Journal of Geophysical Research: Space Physics*, 123(11), pp.9836-9861. doi: 10.1029/2018JA025806.
- Cooper, C., 2016. Citizen science: How ordinary people are changing the face of discovery. Abrams.
- Coster, A.J., Erickson, P. J., Lanzerotti, Lou, eds., *Space Weather Effects and Applications*, Wiley. (2021). DOI: <https://doi.org/10.1002/9781119815570>
- Coster, Anthea, Skone, Susan, Mitchell, Cathryn, De Franceschi, Giorgiana, Alfonso, Lucilla, Romano, Vincenzo, “Global Studies of GPS Scintillation,” Proceedings of the 2005 National Technical Meeting of The Institute of Navigation, San Diego, CA, January 2005, pp. 1130-1139.
- Coxon, J. C., Milan, S. E., & Anderson, B. J. (2018). A review of Birkeland current research using AMPERE. *Electric currents in geospace and beyond*, 257-278.
- Craven P. and Wahba G., Smoothing noisy data with spline functions: Estimating the correct degree of smoothing by the method of generalized cross-validation, *Numerische Mathematik* volume31, pages 377–403 (1978).
- Craven, J. D., Frank, L. A., and Akasofu, S.-I. (1989), Propagation of a westward traveling surge and the development of persistent auroral features, *J. Geophys. Res.*, 94(A6), 6961– 6967, doi:10.1029/JA094iA06p06961.
- Darkjamn (2021), <https://darkjamn.blogspot.com/2015/12/dark-wallpaper-earth.html>, accessed May 2021.
- Datta-Barua, S., Su, Y., Deshpande, K., Miladinovich, D., Bust, G.S., Hampton, D. and Crowley, G., 2015. First light from a kilometer-baseline Scintillation Auroral GPS Array. *Geophysical research letters*, 42(10), pp.3639-3646. doi: 10.1002/2015GL063556.
- Delamere, P.A., Otto, A., Ma, X., Bagenal, F. and Wilson, R.J., 2015. Magnetic flux circulation in the rotationally driven giant magnetospheres. *Journal of Geophysical Research: Space Physics*, 120(6), pp.4229-4245. doi: 10.1002/2015JA021036.
- Delaney, A.H. and Bresler, Y., 1998. Globally convergent edge-preserving regularized reconstruction: an application to limited-angle tomography. *IEEE Transactions on Image Processing*, 7(2), pp.204-221. doi: 10.1109/83.660997
- Deng, Y., Maute, A., Richmond, A.D. and Roble, R.G., 2009. Impact of electric field variability on Joule heating and thermospheric temperature and density. *Geophysical Research Letters*, 36(8). doi: 10.1029/2008GL036916.
- Deshpande, K.B. and Zettergren, M.D., 2019. Satellite-Beacon Ionospheric-Scintillation Global Model of the Upper Atmosphere (SIGMA) III: Scintillation Simulation Using A Physics-Based Plasma Model. *Geophysical Research Letters*, 46(9), pp.4564-4572. doi: 10.1029/2019GL082576.
- Deshpande, K.B., Bust, G.S., Clauer, C.R., Rino, C.L. and Carrano, C.S., 2014. Satellite-beacon Ionospheric-scintillation Global Model of the upper Atmosphere (SIGMA) I: High-latitude sensitivity study of the model parameters. *Journal of Geophysical Research: Space Physics*, 119(5), pp.4026-4043. doi: 10.1029/2019GL082576.

- Deshpande, K.B., Bust, G.S., Clauer, C.R., Scales, W.A., Frissell, N.A., Ruohoniemi, J.M., Spogli, L., Mitchell, C. and Weatherwax, A.T., 2016. Satellite-beacon Ionospheric-scintillation Global Model of the upper Atmosphere (SIGMA) II: Inverse modeling with high-latitude observations to deduce irregularity physics. *Journal of Geophysical Research: Space Physics*, 121(9), pp.9188-9203. doi: 10.1002/2016JA022943.
- Dettmering, D., Limberger, M. and Schmidt, M., 2014, May. Using DORIS for modeling the Vertical Total Electron Content of the Earth's Ionosphere. In EGU General Assembly Conference Abstracts (Vol. 16). doi: 10.1007/s00190-014-0748-2
- Devereux, W.S., Asher, M.S., Heins, R.J., Chacos, A.A., Kusterer, T.L. and Linstrom, L.A., 2003. TIMED GPS navigation system (GNS): design, implementation, and performance assessment. Johns Hopkins APL technical digest, 24(2), p.179.
- Documentary: Chasing Steve (2019), Prod. Leah Mallen and J. Fraser, All-In Productions.
- Doe, R.A., Mendillo, M., Vickrey, J.F., Zanetti, L.J. and Eastes, R.W., 1993. Observations of night-side auroral cavities. *Journal of Geophysical Research: Space Physics*, 98(A1), pp.293-310. doi: 10.1029/92JA02004.
- Doe, R.A., Vickrey, J.F. and Mendillo, M., 1995. Electrodynamic model for the formation of auroral ionospheric cavities. *Journal of Geophysical Research: Space Physics*, 100(A6), pp.9683-9696. doi: 10.1029/95JA00001.
- Donovan, E., Mende, S., Jackel, B., Frey, H., Syrjäsu, M., Voronkov, I., Trondsen, T., Peticolas, L., Angelopoulos, V., Harris, S. and Greffen, M., 2006. The THEMIS all-sky imaging array—System design and initial results from the prototype imager. *Journal of Atmospheric and Solar-Terrestrial Physics*, 68(13), pp.1472-1487. doi: 10.1016/j.jastp.2005.03.027.
- Dungey, J.W., 1961. Interplanetary magnetic field and the auroral zones. *Physical Review Letters*, 6(2), p.47. doi: 10.1103/PhysRevLett.6.47.
- ECSA. (2015) Ten principles of citizen science [Online]. Available at: <https://ecsa.citizen-science.net/documents>.
- EISCAT3d, (2019): <https://www.eiscat.se/eiscat3d/>, accessed 2019.
- ESA, 2021, <https://earth.esa.int/eogateway/instruments/vfm/description>.
- Evans, T, 2019. The Reconstruction of Auroral Zone Plasma Flow Fields and Associated Electric Fields Combining Ground-Based Observation and MultiPoint in Situ Measurements, Senior Honors Thesis, Dept of Physics and Astronomy, Dartmouth College.
- Fernandes, P.A. and Lynch, K.A., 2016. Electrostatic analyzer measurements of ionospheric thermal ion populations. *Journal of Geophysical Research: Space Physics*, 121(7), pp.7316-7325. doi: 10.1002/2016JA022582.
- Fernandes, P.A., Lynch, K.A., Zettergren, M., Hampton, D.L., Bekkeng, T.A., Cohen, I.J., Conde, M., Fisher, L.E., Horak, P., Lessard, M.R. and Miceli, R.J., 2016. Measuring the seeds of ion outflow: Auroral sounding rocket observations of low-altitude ion heating and circulation. *Journal of Geophysical Research: Space Physics*, 121(2), pp.1587-1607. doi: 10.1002/2015JA021536.
- Finlay, C.C., Maus, S., Beggan, C.D., Bondar, T.N., Chambodut, A., Chernova, T.A., Chulliat, A., Golovkov, V.P., Hamilton, B., Hamoudi, M. and Holme, R., 2010. International geomagnetic reference field: the eleventh generation. *Geophysical Journal International*, 183(3), pp.1216-1230. doi: 10.1111/j.1365-246X.2010.04804.x.
- Fisher, L.E., Lynch, K.A., Fernandes, P.A., Bekkeng, T.A., Moen, J., Zettergren, M., Miceli, R.J., Powell, S., Lessard, M.R. and Horak, P., 2016. Including sheath effects in the interpretation of planar retarding potential analyzer's low-energy ion data. *Review of Scientific Instruments*, 87(4), p.043504. doi: 10.1063/1.4944416.

- Forget, B., J-C. Cerisier, A. Berthelier, and J-J. Berthelier. "Ionospheric closure of small-scale Birkeland currents." *Journal of Geophysical Research: Space Physics* 96, no. A2 (1991): 1843-1847.
- Forsyth, C., Sergeev, V.A., Henderson, M.G. et al. Physical Processes of Meso-Scale, Dynamic Auroral Forms. *Space Sci Rev* 216, 46 (2020). <https://doi.org/10.1007/s11214-020-00665-y>
- Fraunberger, Lynch, et al, "Auroral Ionospheric Plasma Flow Extraction using Subsonic Retarding Potential Analyzers", *Rev Scientific Instr*, 2020, DOI: 10.1063/1.5144498.
- Fraunberger, M 2019. 'Fitting Auroral Sounding Rocket Data to Optimize Thermal Ion Sensors'. Undergraduate thesis. Dartmouth College, Hanover.
- Frederick-Frost, K.M. and Lynch, K.A., 2007. Low energy stable plasma calibration facility. *Review of Scientific Instruments*, 78(7), p.075113. doi: 10.1063/1.2756996.
- Frey, H.U., Mende, S.B., Carlson, C.W., Gérard, J.C., Hubert, B., Spann, J., Gladstone, R. and Immel, T.J., 2001. The electron and proton aurora as seen by IMAGE-FUV and FAST. *Geophysical research letters*, 28(6), pp.1135-1138. doi: 10.1029/2000GL012352.
- Frissell, N.A., Joshua S. Vega, E. Markowitz, A.J. Gerrard, W.D. Engelke, P.J. Erickson, E.S. Miller, R.C. Luetzelschwab, and J. Bortnik, High-Frequency Communications Response to Solar Activity in September 2017 as Observed by Amateur Radio Networks, *Space Weather*, 10.1029/2018SW002008, 17, 1, (118-132), (2019).
- Frissell, N.A., Katz, J.D., Gunning, S.W., Vega, J.S., Gerrard, A.J., Earle, G.D., Moses, M.L., West, M.L., Huba, J.D., Erickson, P.J. and Miller, E.S., 2018. Modeling amateur radio soundings of the ionospheric response to the 2017 Great American Eclipse. *Geophysical Research Letters*, 45(10), pp.4665-4674. doi: 10.1029/2018GL077324.
- Frissell, N.A., Miller, E.S., Kaepller, S.R., Ceglia, F., Pascoe, D., Sinanis, N., Smith, P., Williams, R. and Shovkopyas, A., 2014. Ionospheric sounding using real-time amateur radio reporting networks. *Space Weather*, 12(12), pp.651-656. doi: 10.1002/2014SW001132.
- Gallardo-Lacourt, B., Nishimura, Y., Donovan, E., Gillies, D. M., Perry, G. W., Archer, W. E., et al. (2018). A statistical analysis of STEVE. *Journal of Geophysical Research: Space Physics*, 123,9893– 9905. doi: 10.1029/2018JA025368.
- Galvin, A.B., Kistler, L.M., Popecki, M.A., Farrugia, C.J., Simunac, K.D.C., Ellis, L., Möbius, E., Lee, M.A., Boehm, M., Carroll, J. and Crawshaw, A., 2008. The Plasma and Suprathermal Ion Composition (PLASTIC) investigation on the STEREO observatories. In *The STEREO Mission* (pp. 437-486). Springer, New York, NY. doi: 10.1007/s11214-007-9296-x.
- Garbe, G.P., 1990. A study of ion acceleration at rocket altitudes and development and calibration of pitch angle imaging charged particle detectors.
- Garner, T.W., Gaussiran, T.L., York, J.A., Munton, D.M., Slack, C.M. and Mahrous, A.M., 2009. Ionospheric tomography network of Egypt: A new receiver network in support of the International Heliophysical Year. *Earth, Moon, and Planets*, 104(1-4), pp.227-235.
- Garrett, H.B., "Spacecraft charging, an update", *IEEE Transactions on Plasma Science*, DOI:10.1109/27.902229, January 2001.
- Gayetsky, L.E. and Lynch, K.A., 2011. Note: Flowing ion population from a resonance cavity source. *Review of Scientific Instruments*, 82(4), p.046112. Doi: 10.1063/1.3584969.
- GCC Team. (2013, April 11). GCC 4.7 Release Series. *GCC 4.7 Release Series - GNU Project - Free Software Foundation (FSF)*. <https://gcc.gnu.org/gcc-4.7/>. GEMINI, (2021) (<https://github.com/gemini3d/>), accessed May, 2021.
- Germany, G.A., Parks, G.K., Brittnacher, M., Cumnock, J., Lummerzheim, D., Spann, J.F., Chen, L., Richards, P.G. and Rich, F.J., 1997. Remote determination of auroral energy char-

acteristics during substorm activity. *Geophysical research letters*, 24(8), pp.995-998. doi: 10.1029/97GL00864.

Gillies, D. M., Knudsen, D., Spanswick, E., Donovan, E., Burchill, J., and Patrick, M. , 2015. Swarm observations of field-aligned currents associated with pulsating auroral patches, *J. Geophys. Res. Space Physics*, 120, 9484–9499, doi: 10.1002/2015JA021416.

Gillies, D.M., Knudsen, D.J., Donovan, E.F., Spanswick, E.L., Hansen, C., Keating, D. and Erion, S., 2014. A survey of quiet auroral arc orientation and the effects of the interplanetary magnetic field. *Journal of Geophysical Research: Space Physics*, 119(4), pp.2550-2562.

GITM, (2021) GitHub (<https://github.com/aaronjridley/GITM>), accessed May, 2021.

Gjerloev, J. W., S. Ohtani, T. Iijima, B. Anderson, J. Slavin, and G. Le (2011), Characteristics of the terrestrial field-aligned current system, *Ann. Geophys.*, 29, 1713–1729, doi:10.5194/angeo-29-1713-2011.

Gkioulidou, M., Wang, C.-P., Lyons, L. R., and Wolf, R. A.(2009), Formation of the Harang reversal and its dependence on plasma sheet conditions: Rice convection model simulations, *J. Geophys. Res.*, 114, A07204, doi: 10.1029/2008JA013955.

Gledhill, J.A., 1986. The effective recombination coefficient of electrons in the ionosphere between 50 and 150 km. *Radio Science*, 21(3), pp.399-408. doi: 10.1029/RS021i003p00399.

Gold, G.H., Van Loan, C.F. (1996) Matrix Computations. Chapter 10.

Gold, R.E., Solomon, S.C., McNutt Jr, R.L., Santo, A.G., Abshire, J.B., Acuña, M.H., Afzal, R.S., Anderson, B.J., Andrews, G.B., Bedini, P.D. and Cain, J., 2001. The MESSENGER mission to Mercury: scientific payload. *Planetary and Space Science*, 49(14-15), pp.1467-1479.

Grodent, D., 2015. A brief review of ultraviolet auroral emissions on giant planets. *Space Science Reviews*, 187(1-4), pp.23-50. doi: 10.1007/s11214-014-0052-8.

Grubbs, G., II, R. Michell, M. Samara, D. Hampton, and J.-M. Jahn., 2016. A synthesis of star calibration techniques for ground-based narrowband electron-multiplying charge-coupled device imagers used in Auroral Photometry. *J. Geophys.Res. Space Physics*, 121, (pp.5991–6002), doi:10.1002/2015JA022186.

Grubbs, G., Michell, R., Samara, M., Hampton, D., Hecht, J., Solomon, S. and Jahn, J.M., 2018a. A comparative study of spectral auroral intensity predictions from multiple electron transport models. *Journal of Geophysical Research: Space Physics*, 123(1), pp.993-1005. doi: 10.1002/2017JA025026.

Grubbs, G., Michell, R., Samara, M., Hampton, D. and Jahn, J.M., 2018b. Predicting electron population characteristics in 2-D using multispectral ground-based imaging. *Geophysical Research Letters*, 45(1), pp.15-20. doi: 10.1002/2017GL075873.

Haerendel, G., Buchert, S., La Hoz, C., Raaf, B., & Rieger, E. (1993). On the proper motion of auroral arcs. *Journal of Geophysical Research: Space Physics*, 98(A4), 6087-6099.

Hansen, A., Blanch, J., Walter, T. and Enge, P., 2000. Ionospheric correlation analysis for WAAS: quiet and stormy. *proceedings of ION GPS*, Salt Lake City, UT.

Harrington, M, “RENU2 SOUNDING ROCKET ANALYSIS: ION DATABASE CONSTRUCTION”, MS Thesis, Dartmouth College, Hanover NH, 2017

Haskins, C.B., Angert, M.P., Sheehi, E.J., Millard, W.P., Adams, N. and Hennawy, J.R., 2016, March. The Frontier software-defined radio for the solar probe plus mission. In 2016 IEEE Aerospace Conference (pp. 1-11). IEEE. doi: 10.1109/AERO.2016.7500770.

Heise, S., Jakowski, N., Wehrenpfennig, A., Reigber, C. and Lühr, H., 2002. Sounding of the topside ionosphere/plasmasphere based on GPS measurements from CHAMP: Initial results. *Geophysical Research Letters*, 29(14), pp.44-1. doi: 10.1029/2002GL014738.

- Hernandez, E., E.A. Bering, A. Pessoa, M. Manriquez, N. Frissell, and J. LaBelle, HamSci Radio Research Using VLF and HF to measure aurora emissions and related phenomena, Abstract SA028-0004, presented at American Geophysical Union Fall Meeting (2020).
- Huang, C.Y., Su, Y.J., Sutton, E.K., Weimer, D.R. and Davidson, R.L., 2014. Energy coupling during the August 2011 magnetic storm. *Journal of Geophysical Research: Space Physics*, 119(2), pp.1219-1232. doi: 10.1002/2013JA019297.
- Huang, P. M. et al., "Different approaches to developing Small Satellite Missions," 31st Annual AIAA/USU Conference on Small Satellites, 2017.
- Hughes, J., and J. LaBelle, The latitude dependence of auroral roar emissions, *J. Geophys. Res.*, 103, 14910, 1998.
- Iijima, T. and Potemra, T.A., 1976. The amplitude distribution of field-aligned currents at northern high latitudes observed by Triad. *Journal of Geophysical Research*, 81(13), pp.2165-2174. doi: 10.1029/JA081i013p02165.
- Jia, X., Hansen, K. C., Gombosi, T. I., Kivelson, M. G., Tóth, G., DeZeeuw, D. L., and Ridley, A. J.(2012), Magnetospheric configuration and dynamics of Saturn's magnetosphere: A global MHD simulation, *J. Geophys. Res.*, 117, A05225, doi:10.1029/2012JA017575.
- Kaepller, S.R., Hampton, D.L., Nicolls, M.J., Strømme, A., Solomon, S.C., Hecht, J.H. and Conde, M.G., 2015. An investigation comparing ground-based techniques that quantify auroral electron flux and conductance. *Journal of Geophysical Research: Space Physics*, 120(10), pp.9038-9056. doi: 10.1002/2015JA021396.
- Kalmoni, N.M.E., Rae, I.J., Watt, C.E.J., Murphy, K.R., Samara, M., Michell, R.G., Grubbs, G. and Forsyth, C., 2018. A diagnosis of the plasma waves responsible for the explosive energy release of substorm onset. *Nature communications*, 9(1), p.4806. doi: 10.1038/s41467-018-07086-0.
- Kamalabadi, F., Karl, W.C., Semeter, J.L., Cotton, D.M., Cook, T.A. and Chakrabarti, S., 1999. A statistical framework for space-based EUV ionospheric tomography. *Radio Science*, 34(2), pp.437-447. doi: 10.1029/1998RS900026.
- Kaminski, A., Buquo, L., Roman, M.C., Beck, B. and Thaller, M., 2016. NASA's Public Participation Universe: Why and How the US Space Agency Is Democratizing Its Approaches to Innovation. In AIAA SPACE 2016 (p. 5466). doi: 10.2514/6.2016-5466.
- Kan, J. R., & Akasofu, S. I. (1979). A model of the auroral electric field. *Journal of Geophysical Research: Space Physics*, 84(A2), 507-512.
- Karl, W.C., 2005. Regularization in image restoration and reconstruction. In *Handbook of Image and Video Processing*(pp. 183-V). Academic Press.
- Keiling, A., Wygant, J., Fillingim, M., & Trattner, K. J. (2020). Energetics and Alfvénic coupling of a poleward boundary intensification: A Polar case study. *Journal of Geophysical Research: Space Physics*, 125(8), e2020JA028041.
- Kelley, M., 1989. The Earth's Ionosphere: Plasma Physics and Electrodynamics, *Int. Geophys. Ser.*, 43, pp.437-455.
- Kim, H., Lessard, M.R., Jones, S.L., Lynch, K.A., Fernandes, P.A., Aruliah, A.L., Engebretson, M.J., Moen, J.I., Oksavik, K., Yahnin, A.G. and Yeoman, T.K., 2017. Simultaneous observations of traveling convection vortices: Ionosphere-thermosphere coupling. *Journal of Geophysical Research: Space Physics*, 122(5), pp.4943-4959. doi: 10.1002/2017JA023904.
- Kishk, A.A. and Huang, W., 2011. Size-reduction method for dielectric-resonator antennas. *IEEE Antennas and Propagation Magazine*, 53(2), pp.26-38. doi: 10.1109/MAP.2011.5949322.
- Kivelson, M. G. and C.T. Russell, "Introduction to Space Physics", Cambridge University Press,

Apr 28, 1995

- Knudsen, D. J., Burchill, J. K., Buchert, S. C., Eriksson, A. I., Gill, R., Wahlund, J.-E., Åhlen, L., Smith, M., and Moffat, B., 2017. Thermal ion imagers and Langmuir probes in the Swarm electric field instruments, *J. Geophys. Res. Space Physics*, 122, 2655– 2673, doi:10.1002/2016JA022571.
- Knudsen, D.J., Donovan, E.F., Cogger, L.L., Jackel, B. and Shaw, W.D., 2001. Width and structure of mesoscale optical auroral arcs. *Geophysical Research Letters*, 28(4), pp.705-708. doi: 10.1029/2000GL011969.
- Knudsen, D.J., Kelley, M.C. and Vickrey, J.F., 1992. Alfvén waves in the auroral ionosphere: A numerical model compared with measurements. *Journal of Geophysical Research: Space Physics*, 97(A1), pp.77-90. doi: 10.1029/91JA02300.
- Knudsen, D.J., Kelley, M.C., Earle, G.D., Vickrey, J.F. and Boehm, M., 1990. Distinguishing Alfvén waves from quasi-static field structures associated with the discrete aurora: Sounding rocket and HILAT satellite measurements. *Geophysical Research Letters*, 17(7), pp.921-924. doi: 10.1029/GL017i007p00921.
- Kosar, B.C., MacDonald, E.A., Case, N.A. and Heavner, M., 2018a. Aurorasaurus Database of Real-Time, Crowd-Sourced Aurora Data for Space Weather Research. *Earth and Space Science*, 5(12), pp.970-980. doi: 10.1029/2018EA000454.
- Kosar, B.C., MacDonald, E.A., Case, N.A., Zhang, Y., Mitchell, E.J. and Viereck, R., 2018b. A case study comparing citizen science aurora data with global auroral boundaries derived from satellite imagery and empirical models. *Journal of Atmospheric and Solar-Terrestrial Physics*, 177, pp.274-282. doi: 10.1016/J.JASTP.2018.05.006.
- Kovesi, P., 2015. Good colour maps: How to design them. arXiv preprint arXiv:1509.03700.
- Kunitsyn, V.E. and Tereshchenko, E.D., 2003. Ionospheric tomography. Springer Science & Business Media.
- Kunitsyn, V.E., Andreeva, E.S., Razinkov, O.G. and Tereshchenko, E.D. (1994), Phase and phase-difference ionospheric radio tomography. *Int. J. Imaging Syst. Technol.*, 5: 128-140.
- Kunitsyn, V.E., Andreeva, E.S., Tereshchenko, E.D., Khudukon, B.Z. and Nygren, T., 1994. Investigations of the ionosphere by satellite radiotomography. *International Journal of Imaging Systems and Technology*, 5(2), pp.112-127. doi: 10.1002/ima.1850050208.
- LaBelle, J., An Explanation for the Fine Structure of MF Burst Emissions, *Geophys. Res. Lett.*, 38, L03105, doi:10.1029/2010GL046218, 2011a.
- LaBelle, J., Medium Frequency Burst Emissions: A terrestrial analog to Solar Type III bursts?, *Planet. Radio Emissions VII*, ed. by H.O. Rucker, et al., Austrian Acad. Sci. Press, p. 271--282, 2011b.
- LaBelle, J., High-latitude radiowave propagation studies using a meridional chain of receivers, *Ann. Geophys.*, 22, 1705--1718, 2004.
- Lamarche, L. J., Varney, R. H., & Siefring, C. L. (2020). Analysis of Plasma Irregularities on a Range of Scintillation-Scales Using the Resolute Bay Incoherent Scatter Radars. *Journal of Geophysical Research: Space Physics*, 125(3), e2019JA027112.
- Lee, J. K., Kamalabadi, F., and Makela, J. J. (2007), Localized three-dimensional ionospheric tomography with GPS ground receiver measurements, *Radio Sci.*, 42, RS4018, doi:10.1029/2006RS003543.
- Lee, J. K., Kamalabadi, F., and Makela, J. J. (2008), Three-dimensional tomography of ionospheric variability using a dense GPS receiver array, *Radio Sci.*, 43, RS3001, doi:10.1029/2007RS003716.

- Lessard, M., et al., 2019. "Overview of the Rocket Experiment for Neutral Upwelling Sounding Rocket 2 (RENU2), *Geophys. Res. Lett.*, 46, <https://doi.org/10.1029/2018GL081885>
- Liemohn, M. W. (2020). The case for improving the Robinson formulas. *Journal of Geophysical Research: Space Physics*, 125(10), e2020JA028332
- Lohr, D.A., Zanetti, L.J., Anderson, B.J., Potemra, T.A., Hayes, J.R., Gold, R.E., Henshaw, R.M., Mobley, F.F., Holland, D.B., Acuña, M.H. and Scheifele, J.L., 1997. NEAR magnetic field investigation, instrumentation, spacecraft magnetics and data access. In *The Near Earth Asteroid Rendezvous Mission* (pp. 255-281). Springer, Dordrecht. doi: 10.1007/978-94-011-5200-6_6.
- Lomidze, L., Burchill, J.K., Knudsen, D.J., Kouznetsov, A. and Weimer, D.R., 2019. Validity study of the Swarm horizontal cross-track ion drift velocities in the high-latitude ionosphere. *Earth and Space Science*, 6(3), pp.411-432. doi: 10.1029/2018EA000546.
- Lotko, W., 2004. Inductive magnetosphere–ionosphere coupling. *Journal of atmospheric and solar-terrestrial physics*, 66(15-16), pp.1443-1456.
- Loucks, D., Palo, S., Pilinski, M., Crowley, G., Azeem, I., and Hampton, D. (2017), High-latitude GPS phase scintillation from E region electron density gradients during the 20–21 December 2015 geomagnetic storm, *J. Geophys. Res. Space Physics*, 122, 7473– 7490, doi:10.1002/2016JA023839.
- Lu, G., Baker, D. N., McPherron, R. L., Farrugia, C. J., Lummerzheim, D., Ruohoniemi, J. M., et al. (1998). Global energy deposition during the January 1997 magnetic cloud event. *Journal of Geophysical Research: Space Physics*, 103(A6), 11685–11694. <https://doi.org/10.1029/98JA00897>
- Lu, G., Richmond, A. D., Ruohoniemi, J. M., Greenwald, R. A., Hairston, M., Rich, F. J., & Evans, D. S. (2001). An investigation of the influence of data and model inputs on assimilative mapping of ionospheric electrodynamics. *Journal of Geophysical Research: Space Physics*, 106(A1), 417–433. <https://doi.org/10.1029/2000JA000606>
- Lühr,H., J.Park, J.W.Gjerloev, J. Rauberg, I. Michaelis, J. M. G. Merayo, and P. Brauer (2015), Field-aligned currents' scale analysis performed with the Swarm constellation, *Geophys. Res. Lett.*, 42,1–8, doi:10.1002/2014GL062453.
- Lummerzheim, D. and Lilensten, J., 1994, November. Electron transport and energy degradation in the ionosphere: Evaluation of the numerical solution, comparison with laboratory experiments and auroral observations. In *Annales Geophysicae* (Vol. 12, No. 10, pp. 1039-1051).
- Lynch, K.A., Hampton, D.L., Zettergren, M., Bekkeng, T.A., Conde, M., Fernandes, P.A., Horak, P., Lessard, M., Miceli, R., Michell, R. and Moen, J., 2015. MICA sounding rocket observations of conductivity-gradient-generated auroral ionospheric responses: Small-scale structure with large-scale drivers. *Journal of Geophysical Research: Space Physics*, 120(11), pp.9661-9682. doi: 10.1002/2014JA020860.
- Lyon, J.G., Fedder, J.A. and Mobarrey, C.M., 2004. The Lyon–Fedder–Mobarrey (LFM) global MHD magnetospheric simulation code. *Journal of Atmospheric and Solar-Terrestrial Physics*, 66(15-16), pp.1333-1350. doi: 10.1016/j.jastp.2004.03.020.
- Lyons, L.R., Nishimura, Y. and Zou, Y., 2016. Unsolved problems: Mesoscale polar cap flow channels' structure, propagation, and effects on space weather disturbances. *Journal of Geophysical Research: Space Physics*, 121(4), pp.3347-3352. doi: 10.1002/2016JA022437.
- Lysak, R.L., 1991. Feedback instability of the ionospheric resonant cavity. *Journal of Geophysical Research: Space Physics*, 96(A2), pp.1553-1568. doi: 10.1029/90JA02154.
- MacDonald, E.A., Case, N.A., Clayton, J.H., Hall, M.K., Heavner, M., Lalone, N., Patel, K.G. and Tapia, A., 2015. Aurorasaurus: A citizen science platform for viewing and reporting the aurora. *Space Weather*, 13(9), pp.548-559. doi: 10.1002/2015SW001214

- MacDonald, Elizabeth A. (2018a) STEVE and the Citizen Scientists [Online]. Available at: <https://www.americanscientist.org/article/steve-and-the-citizen-scientists>. doi: 10.1511/2018.106.5.283.
- MacDonald, E.A., Donovan, E., Nishimura, Y., Case, N.A., Gillies, D.M., Gallardo-Lacourt, B., Archer, W.E., Spanswick, E.L., Bourassa, N., Connors, M. and Heavner, M., 2018b. New science in plain sight: Citizen scientists lead to the discovery of optical structure in the upper atmosphere. *Science advances*, 4(3), p.eaaq0030. doi: 10.1126/sciadv.aaq0030
- Magnes, W., Oberst, M., Valavanoglou, A., Hauer, H., Hagen, C., Jernej, I., Neubauer, H., Baumjohann, W., Pierce, D., Means, J. and Falkner, P., 2008. Highly integrated front-end electronics for spaceborne fluxgate sensors. *Measurement Science and Technology*, 19(11), p.115801. doi: 10.1088/0957-0233/19/11/115801.
- Marghitu, O., 2012. Auroral arc electrodynamics: Review and outlook. *Auroral Phenomenology and Magnetospheric Processes: Earth And Other Planets*, 197, pp.143-158. doi:10.1029/2011GM001189.
- Marholm, S., Marchand, R., Darian, D., Miloch, W.J. and Mortensen, M., 2019. Impact of Miniaturized Fixed-Bias Multineedle Langmuir Probes on CubeSats. *IEEE Transactions on Plasma Science*. doi: 10.1109/TPS.2019.2915810.
- Markkanen, M., Lehtinen, M., Nygren, T., Pirtilä, J., Henelius, P., Vilenius, E., Tereshchenko, E.D. and Khudukon, B.Z., 1995. Bayesian approach to satellite radiotomography with applications in the Scandinavian sector. In *Annales geophysicae* (Vol. 13, No. 12, pp. 1277-1287). Copernicus.
- Marklund, G. T., Karlsson, T., Blomberg, L. G., Lindqvist, P. A., Fälthammar, C. G., Johnson, M. L., ... & Zanetti, L. J. (1998). Observations of the electric field fine structure associated with the westward traveling surge and large-scale auroral spirals. *Journal of Geophysical Research: Space Physics*, 103(A3), 4125-4144.
- Marsland, S. (2015), Machine learning: An Algorithmic Perspective, Second Edition, CRC Press, ISBN-13: 978-1-4665-8328-3
- MATLAB answers: Reconstructing an image from projection data—MATLAB and Simulink Example [Online]. (2017). Available at: www.mathworks.com/matlabcentral/answers/370726-how-to-control-color-and-brightness-for-a-vector-map.
- Maus, S., Manoj, C., Rauberg, J., Michaelis, I. and Lühr, H., 2010. NOAA/NGDC candidate models for the 11th generation International Geomagnetic Reference Field and the concurrent release of the 6th generation Pomme magnetic model. *Earth, planets and space*, 62(10), p.2. doi: 10.5047/eps.2010.07.006.
- McPherron, R. L., El-Alaoui, M., Walker, R. J., Nishimura, Y., & Weygand, J. M. (2020). The relation of N-S auroral streamers to auroral expansion. *Journal of Geophysical Research: Space Physics*, 125(4), e2019JA027063.
- Mende, S.B., Frey, H.U., Lampton, M., Gerard, J.C., Hubert, B., Fuselier, S., Spann, J., Gladstone, R. and Burch, J.L., 2001. Global observations of proton and electron auroras in a substorm. *Geophysical research letters*, 28(6), pp.1139-1142. doi: 10.1029/2000GL012340.
- Mende, S.B., Harris, S.E., Frey, H.U., Angelopoulos, V., Russell, C.T., Donovan, E., Jackel, B., Greffen, M. and Peticolas, L.M., 2009. The THEMIS array of ground-based observatories for the study of auroral substorms. In *The THEMIS Mission* (pp. 357-387). Springer, New York, NY. doi: 10.1007/978-0-387-89820-9_16.
- Merayo, J.M., Brauer, P., Primdahl, F., Petersen, J.R. and Nielsen, O.V., 2000. Scalar calibration of vector magnetometers. *Measurement science and technology*, 11(2), p.120.
- Mercier, F., Cerri, L. and Berthias, J.P., 2010. Jason-2 DORIS phase measurement processing.

- Advances in space research, 45(12), pp.1441-1454. doi: 10.1016/j.asr.2009.12.002.
- Merkin, V.G. and Lyon, J.G., 2010. Effects of the low-latitude ionospheric boundary condition on the global magnetosphere. *Journal of Geophysical Research: Space Physics*, 115(A10). doi: 10.1029/2010JA015461.
- Merkin, V.G., Anderson, B.J., Lyon, J.G., Korth, H., Wiltberger, M. and Motoba, T., 2013a. Global evolution of Birkeland currents on 10 min timescales: MHD simulations and observations. *Journal of Geophysical Research: Space Physics*, 118(8), pp.4977-4997. doi: 10.1002/jgra.50466.
- Merkin, V.G., Lyon, J.G. and Claudepierre, S.G., 2013b. Kelvin-Helmholtz instability of the magnetospheric boundary in a three-dimensional global MHD simulation during northward IMF conditions. *Journal of Geophysical Research: Space Physics*, 118(9), pp.5478-5496. doi: 10.1002/jgra.50520.
- Mitchell, C.N., Kersley, L., Heaton, J.A.T. and Pryse, S.E., 1997, June. Determination of the vertical electron-density profile in ionospheric tomography: experimental results. In *Annales Geophysicae* (Vol. 15, No. 6, pp. 747-752). Springer-Verlag. doi: 10.1007/s00585-997-0747-1.
- Mittermaier, M. and Roberts, N., 2010. Intercomparison of spatial forecast verification methods: Identifying skillful spatial scales using the fractions skill score. *Weather and Forecasting*, 25(1), pp.343-354. doi: 10.1175/2009WAF2222260.1.
- Moore, T.E., Chandler, M.O., Pollock, C.J., Reasoner, D.L., Arnoldy, R.L., Austin, B., Kintner, P.M. and Bonnell, J., 1996. Plasma heating and flow in an auroral arc. *Journal of Geophysical Research: Space Physics*, 101(A3), pp.5279-5297. doi: 10.1029/95JA03154.
- Morioka, A., Y. Miyoshi, F. Tsuchiya, H. Misawa, K. Yumoto, G.K. Parks, R.R. Anderson, J.D. Menietti, and F. Honary (2009), Vertical evolution of auroral acceleration at substorm onset, *Ann. Geophys.*, 27, 525–535.
- Morioka, A., Y. Miyoshi, F. Tsuchiya, H. Misawa, T. Sakanoi, K. Yumoto, R.R. Anderson, J.D. Menietti, and E.F. Donovan (2007), Dual structure of auroral acceleration regions at substorm onsets as derived from AKR spectra, *J. Geophys. Res.*, 112, A06245, doi:10.1029/2006JA012186.
- Mrak, S., Semeter, J., Hirsch, M., Starr, G., Hampton, D., Varney, R.H., Reimer, A.S., Swoboda, J., Erickson, P.J., Lind, F. and Coster, A.J., 2018. Field-aligned GPS scintillation: Multisensor data fusion. *Journal of Geophysical Research: Space Physics*, 123(1), pp.974-992. doi: 10.1002/2017JA024557.
- Nakamura, R., W. Baumjohann, R. Schoedel, V. A. Sergeev, M. Kubyshkina, M. Brittnacher, T. Mukai, K. Liou, 2001, Earthward flow bursts, auroral streamers and small expansions, *J. Geophys. Res.*, 106, 10791-10802
- Newell, P. T., and J. W. Gjerloev (2011), Evaluation of SuperMAG auroral electrojet indices as indicators of substorms and auroral power, *J. Geophys. Res.*, 116, A12211, doi:10.1029/2011JA016779.
- Newell, P.T., Meng, C.I. and Lyons, K.M., 1996. Suppression of discrete aurorae by sunlight. *Nature*, 381(6585), p.766. doi: 10.1038/381766a0.
- Nikoukar, R., Kamalabadi, F., Kudeki, E., and Sulzer, M. 2012, On resolution/error trade-offs in incoherent scatter radar measurements, *Radio Sci.*, 47, RS1008, doi:10.1029/2011RS004685.
- Nikoukar, R., 2010. Near-optimal inversion of incoherent scatter radar measurements: coding schemes, processing techniques, and experiments (Doctoral dissertation, University of Illinois at Urbana-Champaign).
- Nikoukar, R., Bust, G. and Murr, D., 2015. A novel data assimilation technique for the plasmasphere. *Journal of Geophysical Research: Space Physics*, 120(10), pp.8470-8485. doi: 10.1002/2015JA021455.

- Nikoukar, R., Kamalabadi, F., Kudeki, E. and Sulzer, M., 2008. An efficient near-optimal approach to incoherent scatter radar parameter estimation. *Radio Science*, 43(05), pp.1-15. doi: 10.1029/2007RS003724.
- Nishimura, Y., Gallardo-Lacourt, B., Zou, Y., Mishin, E., Knudsen, D.J., Donovan, E.F., Angelopoulos, V. and Raybell, R., 2019. Magnetospheric signatures of STEVE: Implication for the magnetospheric energy source and inter-hemispheric conjugacy. *Geophysical Research Letters*. doi: 10.1029/2019GL082460.
- Nishimura, Y., Yang, J., Pritchett, P. L., Coroniti, F. V., Donovan, E. F., Lyons, L. R., ... & Mende, S. B. (2016). Statistical properties of substorm auroral onset beads/rays. *Journal of Geophysical Research: Space Physics*, 121(9), 8661-8676.
- NOAA-SWPC, Solar Cycle 25 Forecast Update, <https://www.swpc.noaa.gov/news/solar-cycle-25-forecast-update>, downloaded May 2021
- Nygrén, T., Markkanen, M., Lehtinen, M., Tereshchenko, E.D., Khudukon, B.Z., Evstafiev, O.V. and Pollari, P., 1997, February. Comparison of F-region electron density observations by satellite radio tomography and incoherent scatter methods. In *Annales Geophysicae* (Vol. 14, No. 12, pp. 1422-1428). Springer-Verlag. doi: 10.1007/s00585-996-1422-7.
- O'Neill, M.B., Millard, W.P., Bubnash, B.M., Mitch, R.H. and Boye, J.A., 2016. Frontier Radio Lite: A Single-Board Software-Defined Radio for Demanding Small Satellite Missions, AIAA Small Satellite Conference SSC16-VII-2.
- Otsuka, Y., Ogawa, T., Saito, A. et al. *Earth Planet Sp* (2002) 54: 63. <https://doi.org/10.1186/BF03352422>
- Pedatella, N.M., Lu, G. and Richmond, A.D., 2018. Effects of high-latitude forcing uncertainty on the low-latitude and midlatitude ionosphere. *Journal of Geophysical Research: Space Physics*, 123(1), pp.862-882. doi: 10.1002/2017JA024683.
- Peticolas, L.M., Hallinan, T.J., Stenbaek-Nielsen, H.C., Bonnell, J.W. and Carlson, C.W., 2002. A study of black aurora from aircraft-based optical observations and plasma measurements on FAST. *Journal of Geophysical Research: Space Physics*, 107(A8), pp.SMP-30. doi: 10.1029/2001JA900157.
- Petosa, A. and Ittipiboon, A., 2010. Dielectric resonator antennas: A historical review and the current state of the art. *IEEE antennas and Propagation Magazine*, 52(5), pp.91-116. doi: 10.1109/MAP.2010.5687510.
- Potemra, T.A., Zanetti, L.J. and Acuna, M.H., 1985. The AMPTE CCE magnetic field experiment. *IEEE transactions on geoscience and remote sensing*, (3), pp.246-249. doi: 10.1109/TGRS.1985.289521.
- Raissi, Maziar, Paris Perdikaris, and George E. Karniadakis. "Physics-informed neural networks: A deep learning framework for solving forward and inverse problems involving nonlinear partial differential equations." *Journal of Computational Physics* 378 (2019): 686-707.
- Raymund, T.D., Austen, J.R., Franke, S.J., Liu, C.H., Klobuchar, J.A. and Stalker, J., 1990. Application of computerized tomography to the investigation of ionospheric structures. *Radio Science*, 25(5), pp.771-789. doi: 10.1029/RS025i005p00771.
- Rees, M.H. and Luckey, D., 1974. Auroral electron energy derived from ratio of spectroscopic emissions 1. Model computations. *Journal of Geophysical Research*, 79(34), pp.5181-5186. doi:10.1029/JA079i034p05181.
- Rees, M.H. and Roble, R.G., 1986. Excitation of O (1 D) atoms in aurorae and emission of the [OI] 6300-Å line. *Canadian journal of physics*, 64(12), pp.1608-1613. doi: 10.1139/p86-284.
- Reeves S. J. and Z. Zhe (1999), Sequential algorithms for observation selection, *IEEE Trans. Sig*

- nal Process., vol. 47, no. 1, pp. 123-132.
- Richmond, A.D. and Kamide, Y., 1988. Mapping electrodynamic features of the high-latitude ionosphere from localized observations: Technique. *Journal of Geophysical Research: Space Physics*, 93(A6), pp.5741-5759. doi: 10.1029/JA093iA06p05741.
- Richmond, A.D., 1992. Assimilative mapping of ionospheric electrodynamics. *Advances in Space Research*, 12(6), pp.59-68. doi: 10.1016/0273-1177(92)90040-5.
- Richmond, A.D., 2010. On the ionospheric application of Poynting's theorem. *Journal of Geophysical Research: Space Physics*, 115(A10). doi: 10.1029/2010JA015768.
- Richmond, A.D., Lu, G., Emery, B.A. and Knipp, D.J., 1998. The AMIE procedure: Prospects for space weather specification and prediction. *Advances in Space Research*, 22(1), pp.103-112. doi: 10.1016/S0273-1177(97)01108-3.
- Ridley, A.J., Deng, Y. and Toth, G., 2006. The global ionosphere–thermosphere model. *Journal of Atmospheric and Solar-Terrestrial Physics*, 68(8), pp.839-864. doi: 10.1016/j.jastp.2006.01.008.
- Robert, P., Dunlop, M. W., Roux, A., & Chanteur, G. (1998). Accuracy of current density determination. In G. Paschmann & P. W. Daly (Eds.), *Analysis methods for multi-spacecraft data*, ISSI scientific Reports Series (Vol. 1, pp. 395–418). Bern: Springer.
- Roberts, N.M. and Lean, H.W., 2008. Scale-selective verification of rainfall accumulations from high-resolution forecasts of convective events. *Monthly Weather Review*, 136(1), pp.78-97. doi: 10.1175/2007MWR2123.1.
- Roberts, T.M., Lynch, K.A., Clayton, R.E., Weiss, J. and Hampton, D.L., 2017. A small spacecraft for multipoint measurement of ionospheric plasma. *Review of Scientific Instruments*, 88(7), p.073507. doi: 10.1063/1.4992022.
- Robinson, R. M., Vondrak, R. R., and Potemra, T. A. (1985), Auroral zone conductivities within the field-aligned current sheets, *J. Geophys. Res.*, 90(A10), 9688– 9696, doi:10.1029/JA090iA10p09688.
- Robinson, R. M., Vondrak, R. R., Miller, K., Dabbs, T., & Hardy, D. (1987). On calculating ionospheric conductances from the flux and energy of precipitating electrons. *Journal of Geophysical Research*, 92(A3), 2565– 2569. <https://doi.org/10.1029/JA092iA03p02565>
- Rogers, N.C., E.M. Warrington, and T.B. Jones, Large HF bearing errors for propagation paths tangential to the auroral oval, *IEEE Proc. Microw. Antennas Propag.*, 144(4), 241-249, 1997.
- Russell, C. T., B. J. Anderson, W. Baumjohann, K. R. Bromund, D. Dearborn, D. Fischer, G. Le, H. K. Leinweber, D. Leneman, W. Magnes, J. D. Means, M. B. Moldwin, R. Nakamura, D. Pierce, F. Plaschke, K. M. Ro, J. A. Slavin, R. J. Strangeway, R. Torbert, C. Hagen, I. Jernej, A. Valavanoglou, I. Richter (2014), The Magnetospheric Multiscale Magnetometers, *Space Sci. Rev.*, doi:10.1007/s11214-014-0057-3.
- Sarkango, Y., Jia, X., & Toth, G. (2019). Global MHD simulations of the response of Jupiter's magnetosphere and ionosphere to changes in the solar wind and IMF. *Journal of Geophysical Research: Space Physics*, 124, 5317– 5341. <https://doi.org/10.1029/2019JA026787>
- Sarno-Smith, L. K., B. A. Larsen, R. M. Skoug, M. W. Liemohn, A. Breneman, J. R. Wygant, and M. F. Thomsen (2016), Spacecraft surface charging within geosynchronous orbit observed by the Van Allen Probes, *Space Weather*, 14, 151– 164, doi:10.1002/2015SW001345.
- Sarraih P. et al., “SPIS 5: New Modeling Capabilities and Methods for Scientific Missions,” in *IEEE Transactions on Plasma Science*, vol. 43, no. 9, pp. 2789-2798, Sept. 2015, doi: 10.1109/TPS.2015.2445384.
- Schaubert, D.H., D. M. Pozar and A. Adrian, “Effect of microstrip antenna substrate thickness and permittivity: comparison of theories with experiment,” in *IEEE Transactions on Antennas and*

- Propagation, vol. 37, no. 6, pp. 677-682, June 1989, doi: 10.1109/8.29353.
- Schunk, R.W. and Sojka, J.J., 1982. Ion temperature variations in the daytime high-latitude F region. *Journal of Geophysical Research: Space Physics*, 87(A7), pp.5169-5183. doi: 10.1029/JA087iA07p05169.
- Semeter, J., Mrak, S., Hirsch, M., Swoboda, J., Akbari, H., Starr, G.,... Pankratius, V. (2017). GPS signal corruption by the discrete Aurora: Precise measurements from the Mahali experiment. *Geophysical Research Letters*, 44, 9539– 9546. <https://doi.org/10.1002/2017GL073570>
- Semeter, J., & Kamalabadi, F. (2005). Determination of primary electron spectra from incoherent scatter radar measurements of the auroral E region. *Radio Science*, 40(2), 1-17.
- Semeter, J., Butler, T., Heinselman, C., Nicolls, M., Kelly, J. and Hampton, D., 2009. Volumetric imaging of the auroral ionosphere: Initial results from PFISR. *Journal of Atmospheric and Solar-Terrestrial Physics*, 71(6-7), pp.738-743. doi: 10.1016/j.jastp.2008.08.014.
- Sergeev V, Sauvaud JA, Popescu D, Kovrashkin R, Liou K, Newell P, Brittnacher M, Parks G, Nakamura R, Mukai T, Reeves G, 2000, Multiple-spacecraft observation of a narrow transient plasma jet in the earth's plasma sheet. *Geophys Res Lett* 27(6):851–854
- Sharif B., and F. Kamalabadi (2008), Optimal Sensor Array Configuration in Remote Image Formation, in *IEEE Transactions on Image Processing*, vol. 17, no. 2, pp. 155-166, doi: 10.1109/TIP.2007.914225
- Sharif, B., and F. Kamalabadi (2005), Optimal discretization resolution in algebraic image reconstructions, in *Bayesian Inference and Maximum Entropy Methods in Science and Engineering*, edited by K. H. Knuth, A. E. Abbas, R. D. Morris, and J. P. Castle, Am. Inst. Phys. Conf. Proc., 803, 199–206.
- Sharma, A. and R. Stilwell. “A low profile broadband UHF canted turnstile antenna phasing network.” 2017 USNC-URSI Radio Science Meeting (Joint with AP-S Symposium) (2017): 117-118.
- Shepherd, S.G., J. LaBelle, C.W. Carlson, and G. Rostoker, The latitudinal dynamics of auroral roar emissions, *J. Geophys. Res.*, 104, 17217, 1999.
- Shupe, M. D., , S. Y. Matrosov, , and T. Uttal, 2006: Arctic mixed-phase cloud properties derived from surface-based sensors at SHEBA. *J. Atmos. Sci.*, 63, 697–711.
- Siddiqui, M.U., Gayetsky, L.E., Mella, M.R., Lynch, K.A. and Lessard, M.R., 2011. A laboratory experiment to examine the effect of auroral beams on spacecraft charging in the ionosphere. *Physics of Plasmas*, 18(9), p.092905. doi: 10.1063/1.3640512.
- Smith, A.M., Mitchell, C.N., Watson, R.J., Meggs, R.W., Kintner, P.M., Kauristie, K. and Honary, F., 2008. GPS scintillation in the high arctic associated with an auroral arc. *Space Weather*, 6(3). doi: 10.1029/2007SW000349.
- Solomon, S.C., 2001. Auroral particle transport using Monte Carlo and hybrid methods. *Journal of Geophysical Research: Space Physics*, 106(A1), pp.107-116. doi: 10.1029/2000JA002011.
- Solomon, S.C., 2017. Global modeling of thermospheric airglow in the far ultraviolet. *Journal of Geophysical Research: Space Physics*, 122(7), pp.7834-7848. doi: 10.1002/2017JA024314.
- Sonnerup, B. U. Ö., & Scheible, M. (1998). Minimum and maximum variance analysis. In G. Paschmann, & P. W. Daly (Eds.), *Analysis Methods for Multi-Spacecraft Data* (no. SR-001 in ISSI Scientific Reports, chap. 8) (pp. 185–220). Noordwijk, Netherlands: ESA Publ. Div.
- Stenbaek-Nielsen, H.C., Hallinan, T.J., Osborne, D.L., Kimball, J., Chaston, C., McFadden, J., Delory, G., Temerin, M. and Carlson, C.W., 1998. Aircraft observations conjugate to FAST: Auroral are thicknesses. *Geophysical research letters*, 25(12), pp.2073-2076. doi: 10.1029/98GL01058.
- St-Maurice, J.P. and Schunk, R.W., 1979. Ion velocity distributions in the high-latitude ionosphere.

- Reviews of Geophysics, 17(1), pp.99-134. doi: 10.1029/RG017i001p00099.
- Streltsov, A.V. and Lotko, W., 2008. Coupling between density structures, electromagnetic waves and ionospheric feedback in the auroral zone. *Journal of Geophysical Research: Space Physics*, 113(A5). doi: 10.1029/2007JA012594.
- Strickland, D.J., Meier, R.R., Hecht, J.H. and Christensen, A.B., 1989. Deducing composition and incident electron spectra from ground-based auroral optical measurements: Theory and model results. *Journal of Geophysical Research: Space Physics*, 94(A10), pp.13527-13539. doi:10.1029/JA094iA10p13527.
- Sugiura, M., 1984. A fundamental magnetosphere-ionosphere coupling mode involving field-aligned currents as deduced from DE-2 observations. *Geophysical research letters*, 11(9), pp.877-880. doi: 10.1029/GL011i009p00877.
- Sukur, M.I.A., Rahim, M.K.A. and Murad, N.A., 2013, September. Hybrid dielectric resonator with patch antenna at ultra-high frequency band. In 2013 IEEE International Conference on RFID-Technologies and Applications (RFID-TA) (pp. 1-4). IEEE. doi: 10.1109/RFID-TA.2013.6694535.
- Sydorenko, D. and Rankin, R., 2013. Simulation of O⁺ upflows created by electron precipitation and Alfvén waves in the ionosphere. *Journal of Geophysical Research: Space Physics*, 118(9), pp.5562-5578. doi: 10.1002/jgra.50531.
- Tavernier G, Fagard H, Feissel-Vernier M, Lemoine F, Noll C, Ries J, Soudarin L, Willis P (2005) The international DORIS service, *Adv Space Res* 36(3):333–341
- Torbert, R.B., Burch, J.L., Phan, T.D., Hesse, M., Argall, M.R., Shuster, J., Ergun, R.E., Alm, L., Nakamura, R., Genestreti, K.J. and Gershman, D.J., 2018. Electron-scale dynamics of the diffusion region during symmetric magnetic reconnection in space. *Science*, 362(6421), pp.1391-1395. doi: 10.1126/science.aat2998.
- Torbert, R.B., Vaith, H., Granoff, M., Widholm, M., Gaidos, J.A., Briggs, B.H., Dors, I.G., Chutter, M.W., Macri, J., Argall, M. and Bodet, D., 2016. The electron drift instrument for MMS. *Space Science Reviews*, 199(1-4), pp.283-305. doi: 10.1007/s11214-015-0182-7.
- Torr, M.R., Torr, D.G., Zukic, M., Johnson, R.B., Ajello, J., Banks, P., Clark, K., Cole, K., Keffer, C., Parks, G. and Tsurutani, B., 1995. A far ultraviolet imager for the international solar-terrestrial physics mission. *Space Science Reviews*, 71(1-4), pp.329-383. doi: 10.1007/BF00751335.
- TREx, (2019): <https://www.ucalgary.ca/aurora/projects/trex>, accessed 2019.
- Troyer, R. N., Jaynes, A. N., Jones, S. L., Knudsen, D. J., & Trondsen, T. S. (2021). The diffuse auroral eraser. *Journal of Geophysical Research: Space Physics*, 126, e2020JA028805. <https://doi.org/10.1029/2020JA028805>
- University of Calgary. Auroral Imaging Group, Projects [Online]. Available at: <https://www.ucalgary.ca/aurora/projects>.
- University of Calgary. What is TREx? [Online]. Available at: http://aurora.phys.ucalgary.ca/public/trex/TREx_factsheet.png.
- Vierinen, J., Norberg, J., Lehtinen, M. S., Amm, O., Roininen, L., Väänänen, A., Erickson, P. J., and McKay-Bukowski, D. (2014), Beacon satellite receiver for ionospheric tomography, *Radio Sci.*, 49, 1141– 1152, doi: 10.1002/2014RS005434.
- Vogel, C.R. and Oman, M.E., 1996. Iterative methods for total variation denoising. *SIAM Journal on Scientific Computing*, 17(1), pp.227-238. doi: 10.1137/0917016.
- Vogel, C.R., 2002. Computational methods for inverse problems (Vol. 23). Siam.
- Warrington, E.M., N.C. Rogers, and T.B. Jones, Large bearing errors for propagation paths contained within the polar cap, *IEEE Proc. Microw. Antennas Propag.*, 144(4), 241-249, 1997.

Notice: Use or disclosure of the proprietary and competition sensitive material on this page is subject to the proposal title page restriction.

- Waters, C.L., Anderson, B.J. and Liou, K., 2001. Estimation of global field aligned currents using the Iridium® system magnetometer data. *Geophysical Research Letters*, 28(11), pp.2165-2168. doi: 10.1029/2000GL012725.
- Weatherwax, A.T., P.H. Yoon, and J. LaBelle, Model results and interpretation related to topside observations of auroral roar, *J. Geophys. Res.*, 107, 10.1029/2001JA000315, 2002.
- Weimer, D.R., 1996. A flexible, IMF dependent model of high-latitude electric potentials having “space weather” applications. *Geophysical Research Letters*, 23(18), pp.2549-2552. doi: 10.1029/96GL02255.
- Wiggins, A. and He, Y., 2016, February. Community-based data validation practices in citizen science. In Proceedings of the 19th ACM Conference on computer-supported cooperative work & social computing (pp. 1548-1559). ACM. doi: 10.1145/2818048.2820063.
- Willis, P., Fagard, H., Ferrage, P., Lemoine, F.G., Noll, C.E., Noomen, R., Otten, M., Ries, J.C., Rothacher, M., Soudarin, L. and Tavernier, G., 2010. The international DORIS service (IDS): toward maturity. *Advances in space research*, 45(12), pp.1408-1420. doi:10.1016/j.asr.2009.11.018.
- Willis, P., Soudarin, L., Jayles, C. and Rolland, L., 2007. DORIS applications for solid earth and atmospheric sciences. *Comptes Rendus Geoscience*, 339(16), pp.949-959. doi: 10.1016/j.crte.2007.09.015.
- Wiltberger, M., Merkin, V., Lyon, J.G. and Ohtani, S., 2015. High-resolution global magnetohydrodynamic simulation of bursty bulk flows. *Journal of Geophysical Research: Space Physics*, 120(6), pp.4555-4566. doi: 10.1002/2015JA021080.
- Winningham, J.D., Sharber, J.R., Frahm, R.A., Burch, J.L., Eaker, N., Black, R.K., Blevins, V.A., Andrews, J.P., Rudzki, J., Sablik, M.J. and Chenette, D.L., 1993. The UARS particle environment monitor. *Journal of Geophysical Research: Atmospheres*, 98(D6), pp.10649-10666. doi: 10.1029/93JD00461.
- Wygant, J.R., Keiling, A., Cattell, C.A., Johnson, M., Lysak, R.L., Ternerin, M., Mozer, F.S., Kletzing, C.A., Scudder, J.D., Peterson, W. and Russell, C.T., 2000. sheet-tail lobe boundary to UVI images: An energy source for the aurora. *Journal of Geophysical Research*, 105(A8), pp.18-675.
- Yamamoto, M., 2008. Digital beacon receiver for ionospheric TEC measurement developed with GNU Radio. *Earth, Planets and Space*, 60(11), pp.e21-e24. doi: 10.1186/BF03353137.
- Yang, J., Toffoletto, F., Lu, G., and Wiltberger, M.(2014), RCM-E and AMIE studies of the Harang reversal formation during a steady magnetospheric convection event, *J. Geophys. Res. Space Physics*, 119, 7228– 7242, doi:10.1002/2014JA020207.
- Yoon, P.H., J. LaBelle, A.T. Weatherwax, and M. Samara, Mode conversion radiation in the terrestrial ionosphere and magnetosphere, in *Geospace Electromagnetic Waves and Radiation*, ed. by R.A. Treumann and J. LaBelle, Springer-Verlag, 2006.
- Young, D.T., Bame, S.J., Thomsen, M.F., Martin, R.H., Burch, J.L., Marshall, J.A. and Reinhard, B., 1988. 2π -radian field-of-view toroidal electrostatic analyzer. Review of scientific instruments, 59(5), pp.743-751. doi: 10.1063/1.1139821.
- Zanetti, L., Potemra, T., Erlandson, R., Bythrow, P., Anderson, B., Lui, A., Ohtani, S.I., Fountain, G., Henshaw, R., Ballard, B. and Lohr, D., 1994. Magnetic field experiment on the Freja satellite. In *The Freja Mission* (pp. 61-78). Springer, Dordrecht. doi: 10.1007/978-94-011-0299-5_4.
- Zanetti, L.J., Baumjohann, W. and Potemra, T.A., 1983. Ionospheric and Birkeland current distributions inferred from the MAGSAT magnetometer data. *Journal of Geophysical Research: Space Physics*, 88(A6), pp.4875-4884. doi: 10.1029/JA088iA06p04875.

- Zettergren M., M. Hirsch, P. Inchin, J. Klenzing, and G. Grubbs, Gemini3D ionospheric modeling suite (software). <http://doi.org/10.5281/zenodo.4757432>
- Zettergren, M. and Semeter, J., 2012. Ionospheric plasma transport and loss in auroral downward current regions. *Journal of Geophysical Research: Space Physics*, 117(A6). doi: 10.1029/2012JA017637.
- Zettergren, M. D., and Snively, J. B. (2015), Ionospheric response to infrasonic-acoustic waves generated by natural hazard events, *J. Geophys. Res. Space Physics*, 120, 8002– 8024, doi:10.1002/2015JA021116.
- Zettergren, M., Lynch, K., Hampton, D., Nicolls, M., Wright, B., Conde, M., Moen, J., Lessard, M., Miceli, R. and Powell, S., 2014. Auroral ionospheric F region density cavity formation and evolution: MICA campaign results. *Journal of Geophysical Research: Space Physics*, 119(4), pp.3162-3178. doi: 10.1002/2013JA019583.
- Zettergren, M., Semeter, J., Burnett, B., Oliver, W., Heinselman, C., Blelly, P.L. and Diaz, M., 2010. Dynamic variability in F-region ionospheric composition at auroral arc boundaries. *Anales Geophysicae* (09927689), 28(2).
- Zettergren, M., Semeter, J., Heinselman, C. and Diaz, M., 2011. Incoherent scatter radar estimation of F region ionospheric composition during frictional heating events. *Journal of Geophysical Research: Space Physics*, 116(A1). doi: 10.1029/2010JA016035.
- Zettergren, M.D. and Snively, J.B., 2019. Latitude and Longitude Dependence of Ionospheric TEC and Magnetic Perturbations From Infrasonic-Acoustic Waves Generated by Strong Seismic Events. *Geophysical Research Letters*, 46(3), pp.1132-1140. doi: 10.1029/2018GL081569.
- Zhang, B., Lotko, W., Brambles, O., Wiltberger, M. and Lyon, J., 2015. Electron precipitation models in global magnetosphere simulations. *Journal of Geophysical Research: Space Physics*, 120(2), pp.1035-1056. doi: 10.1002/2014JA020615.
- Zhu J., Taesung Park, Phillip Isola, and Alexei A. Efros. “Unpaired Image-to-Image Translation using Cycle-Consistent Adversarial Networks”, in IEEE International Conference on Computer Vision (ICCV), 2017.
- Zhu, J., Ridley, A.J. and Deng, Y., 2016. Simulating electron and ion temperature in a global ionosphere thermosphere model: Validation and modeling an idealized substorm. *Journal of Atmospheric and Solar-Terrestrial Physics*, 138, pp.243-260. doi: 10.1016/j.jastp.2016.01.005.
- Zmuda,A. J. and J.C. Armstrong, The diurnal flow pattern of field-aligned currents, *J. geophys. Res.*, 79 (1974), p. 4611
- Zou, M. and Pan, J., 2015. Investigation of resonant modes in wideband hybrid omnidirectional rectangular dielectric resonator antenna. *IEEE Transactions on Antennas and Propagation*, 63(7), pp.3272-3275. doi: 10.1109/TAP.2015.2425421.
- Zou, S., Lyons, L.R., Wang, C.P., Boudouridis, A., Ruohoniemi, J.M., Anderson, P.C., Dyson, P.L. and Devlin, J.C., 2009. On the coupling between the Harang reversal evolution and substorm dynamics: A synthesis of SuperDARN, DMSP, and IMAGE observations. *Journal of Geophysical Research: Space Physics*, 114(A1). doi: 10.1029/2008JA013449.
- Zou, S., Moldwin, M.B., Lyons, L.R., Nishimura, Y., Hirahara, M., Sakanoi, T., Asamura, K., Nicolls, M.J., Miyashita, Y., Mende, S.B. and Heinselman, C.J., 2010. Identification of sub-storm onset location and preonset sequence using Reimei, THEMIS GBO, PFISR, and Geotail. *Journal of Geophysical Research: Space Physics*, 115(A12). doi: 10.1029/2010JA015520.
- Zou, S., Moldwin, M.B., Nicolls, M.J., Ridley, A.J., Coster, A.J., Yizengaw, E., Lyons, L.R. and Donovan, E.F., 2013. Electrodynamics of the high-latitude trough: Its relationship with convection flows and field-aligned currents. *Journal of Geophysical Research: Space Physics*, 118(5), pp.2565-2572. doi: 10.1002/jgra.50120. doi: 10.1002/jgra.50120.

Notice: Use or disclosure of the proprietary and competition sensitive material on this page is subject to the proposal title page restriction.

storm onset location and preonset sequence using Reimei, THEMIS GBO, PFISR, and Geotail. Journal of Geophysical Research: Space Physics, 115(A12). doi: 10.1029/2010JA015520.

Zou, S., Moldwin, M.B., Nicolls, M.J., Ridley, A.J., Coster, A.J., Yizengaw, E., Lyons, L.R. and Donovan, E.F., 2013. Electrodynamics of the high-latitude trough: Its relationship with convection flows and field-aligned currents. Journal of Geophysical Research: Space Physics, 118(5), pp.2565-2572. doi: 10.1002/jgra.50120. doi: 10.1002/jgra.50120.